https://doi.org/10.5194/egusphere-2026-1107
Preprint. Discussion started: 6 March 2026

Two Decades of Aerosol Optical Depth evolution from CAMS Reanalysis

Anna Moustaka[1,2], Antonis Gkikas[3], Stavros-Andreas Logothetis[3,4], Johannes Flemming[5], Samuel Rémy[6], Melanie Ades[5], Angela Benedetti[5], Kleareti Tourpali[1], Vassilis Amiridis[7], and Stelios Kazadzis[2]

[1] Laboratory of Atmospheric Physics, Department of Physics, Aristotle University of Thessaloniki, Thessaloniki, 54124, Greece
[2] Physicalisch Meteorologisches Observatorium, World Radiation Center, Davos, 7260, Switzerland
[3] Research Centre for Atmospheric Physics and Climatology, Academy of Athens, Athens, 11521, Greece
[4] Laboratory of Atmospheric Physics, Physics Department, University of Patras, Patras, 26500, Greece
[5]Research Department, European Centre for Medium-Range Weather Forecasts, Reading, RG2 9AX, UK
[6]HYGEOS, Lille, 59000, France
[7]Institute for Astronomy, Astrophysics, Space Applications and Remote Sensing, National Observatory of Athens, Athens, 11810, Greece

Correspondence to: Anna Moustaka (anna.moustaka@pmodwrc.ch)

Abstract. Aerosol optical depth (AOD) is a key indicator for evaluating global climate change, and its long-term trends provide critical insights into the evolving climatic impact of atmospheric aerosols. In this study, we analyse the long-term (2003–2024) AOD record from the fourth-generation ECMWF Atmospheric Composition Reanalysis (EAC4) to investigate global and regional variability and long-term trends over the past two decades. EAC4 is evaluated against independent AERONET observations from 178 stations selected using strict data-availability criteria. The impact of satellite assimilation is explicitly quantified through comparison with a free-running control simulation (CTRL). EAC4 reproduces observed global AOD variability with high skill (R = 0.84, RMSE = 0.12, IOA = 0.90; >1.6 million collocations) and shows strong agreement with AERONET-derived trends at stations exhibiting statistically significant changes (R = 0.89), correctly capturing the trend sign at 96.7% of sites. Negative trends are generally well represented, while positive trends are more frequently underestimated. Trend analyses across 18 regions of interest reveal significant AOD declines over eastern China, North Africa, Central Europe, and the eastern United States, alongside persistent increases over South Asia and the Middle East. Decadal analyses identify pronounced transitions, including a reversal from increasing to decreasing trends over eastern China and shifts in several dust- and biomass-burning-dominated regions. Sliding-window trend diagnostics further highlight temporal variability and regime changes. By integrating long-term reanalysis data, independent validation, and component-resolved diagnostics, this study provides a consistent assessment of recent global AOD evolution.

https://doi.org/10.5194/egusphere-2026-1107
Preprint. Discussion started: 6 March 2026

1 Introduction

Atmospheric aerosols, whether of natural or anthropogenic origin, play a pivotal role in the Earth–atmosphere system and remain among the most uncertain climate forcings (IPCC, 2021). Through the scattering and absorption of solar and terrestrial radiation, they perturb the radiative balance, modify surface temperature, and alter the atmospheric thermodynamic structure (Ackerman and Toon, 1981; Lohmann and Feichter, 2005; Zhao et al., 2012; Yang et al., 2020). Depending on their absorption properties, aerosols may cool the surface while heating the atmosphere, and changes in their optical characteristics can even reverse the sign of their radiative forcing (Hansen et al., 1997; Ding et al., 2016; Sun et al., 2018; Zheng et al., 2019; Moustaka et al., 2024), with the aerosol direct effect partly offsetting greenhouse gas–induced warming in recent decades (Bernstein et al., 2007). Aerosols also exert important indirect effects by acting as cloud condensation nuclei (CCN) and ice-nucleating particles (INPs), thereby modifying cloud microphysical and radiative properties, extending cloud lifetime, and influencing precipitation efficiency, atmospheric circulation, and the global water cycle (Twomey et al., 1984; Haywood and Boucher, 2000; Jiang et al., 2018). Beyond climate, aerosols strongly influence environmental quality and human health. Their complex physical and chemical properties affect air quality (Che et al., 2014; Gui et al., 2022; Z. Li et al., 2017), visibility (Che et al., 2007; Liu et al., 2013, 2020), and ecosystems (W. Li et al., 2017; Liu et al., 2017; Yue et al., 2017), and pose severe health risks, with fine particulate matter contributing to respiratory and cardiovascular diseases and premature mortality (Cohen et al., 2017; Xue et al., 2019; Wei et al., 2019, 2021). Unlike long-lived greenhouse gases such as CO_2, CH_4, and N_2O, aerosols are short-lived and highly variable in space and time; therefore, understanding their optical and microphysical properties, long-term variability, and trends is essential, as changes in aerosol loading and composition can alter both the magnitude and direction of their forcing and influence the effectiveness of emission mitigation strategies (IPCC, 2021).

Aerosol optical depth (AOD), which represents the column-integrated attenuation of solar radiation by atmospheric aerosols, is a fundamental parameter for quantifying aerosol loading and assessing its impacts on radiative forcing, climate, cloud processes, and precipitation. Owing to the sustained development of ground-based networks and satellite observing systems over the past decades, a broad suite of long-term AOD datasets is now available. These datasets enable detailed investigations of aerosol variability on annual, seasonal, and decadal timescales at both global and regional scales (De Leeuw et al., 2018; Proestakis et al., 2018; Gui et al., 2021; Logothetis et al., 2021; Xian et al., 2022; Zhang et al., 2025). Ground-based observations from networks such as the Aerosol Robotic Network (AERONET; Holben et al., 1998, 2001) provide high-quality, long-term reference measurements, while satellite instruments—including the Moderate Resolution Imaging Spectroradiometer (MODIS; Levy et al., 2015) and the Multi-angle Imaging Spectroradiometer (MISR; Diner et al., 1998)—provide near-global spatial coverage. In addition, the Cloud–Aerosol Lidar with Orthogonal Polarization (CALIOP; Winker et al., 2009) has delivered vertically resolved aerosol observations over more than 15 years, offering complementary information on aerosol vertical structure. In parallel, atmospheric reanalyses such as the Modern-Era Retrospective Analysis for Research and Applications, Version 2 (MERRA-2; Buchard et al., 2017; Gelaro et al., 2017) and the Copernicus

https://doi.org/10.5194/egusphere-2026-1107
Preprint. Discussion started: 6 March 2026

Atmosphere Monitoring Service (CAMS; Morcrette et al., 2009) combine numerical modeling with diverse observational datasets to provide temporally and spatially consistent estimates of aerosol distributions.

The Copernicus Atmosphere Monitoring Service (CAMS) combines ground-based observations, satellite retrievals, and numerical atmospheric modeling to deliver temporally consistent and near–real-time aerosol products, including high-resolution AOD fields (Peuch et al., 2022). Operated by the European Centre for Medium-Range Weather Forecasts (ECMWF), CAMS builds on more than a decade of experience in global atmospheric composition forecasting and reanalysis (Inness et al., 2019). A core component of the CAMS system is data assimilation, which optimally merges model background information with observations while explicitly accounting for their respective uncertainties (Courtier et al., 1994). This is implemented using a four-dimensional variational (4D-Var) assimilation framework within the ECMWF Integrated Forecast System (IFS). For aerosol modeling, CAMS assimilates AOD retrievals from the Moderate Resolution Imaging Spectroradiometer (MODIS) aboard the Aqua and Terra satellites since 2003 (Levy et al., 2015). These observations are complemented by Advanced Along-Track Scanning Radiometer (AATSR; Popp et al., 2016) retrievals from Envisat , spanning 2003 to March 2012. Numerous studies have shown that the assimilation of satellite-based AOD significantly improves estimates of aerosol loading and reduces model spread compared with free-running simulations (Zhang et al., 2008; Benedetti et al., 2009; Di Tomaso et al., 2017; Xian et al., 2019; Garrigues et al., 2023). These improvements are particularly evident during intense aerosol events, such as dust storms and biomass burning episodes, where free-running models tend to underestimate AOD and where large emission uncertainties prevail (Benedetti et al., 2009; Choi et al., 2020; Escribano et al., 2022). Through this integrated modeling and assimilation framework, CAMS provides a comprehensive suite of aerosol and atmospheric composition products supporting applications in air-quality monitoring and forecasting, climate research, and health impact assessments (Casciaro et al., 2022; Sbai et al., 2022).

The performance of CAMS aerosol products has been extensively evaluated against AERONET observations (Blake et al., 2025). Globally, CAMS exhibit good agreement with ground-based measurements, although regional overestimations remain, particularly over North America, western Europe, South America, and the Tibetan Plateau (Zhao et al., 2024). Inness et al. (2019) compared the latest CAMS Reanalysis (CAMSRA) with earlier versions and demonstrated that CAMSRA had the lowest mean bias against AERONET, while the previous CAMS Interim Reanalysis (CIRA; Flemming et al., 2017) and Monitoring Atmospheric Composition and Climate Reanalysis (MACCRA; Flemming et al., 2015) showed larger positive or negative biases depending on region. However, the authors reported unrealistic AOD hotspots near volcanic outgassing regions such as Mauna Loa and Mexico City, linked to difficulties in representing diffuse volcanic emissions at model resolution and uncertainties in the treatment of sulfate formation from volcanic SO_2. Regional validations provide additional insight: CAMS reproduces spatial AOD gradients in the eastern Mediterranean and Middle East but tends to underestimate extreme dust and pollution events (Tuygun and Elbir, 2024), while over Brazil CAMS performed well, showing high correlations, low error metrics, and Willmott indices close to 1 (Pedreira Júnior et al., 2024). More recent evaluations confirmed improvements in global AOD representation, though dust-heavy regions continue to show discrepancies (Eskes et al., 2024). Collectively, these

https://doi.org/10.5194/egusphere-2026-1107
Preprint. Discussion started: 6 March 2026

studies underline that CAMS offers reliable large-scale AOD fields and temporal consistency, while local-scale biases persist, particularly in regions with complex aerosol sources or during high aerosol loading outbreaks.

Over the past decade, numerous studies have investigated intra-annual and interannual variability in aerosol loading at global and regional scales using combinations of ground-based observations, satellite retrievals, and numerical modeling frameworks (e.g., Chin et al., 2014; Klingmüller et al., 2016; Hammer et al., 2018; Che et al., 2019; Gui et al., 2021; Logothetis et al., 2021; Zhao et al., 2024; Zhang et al., 2025). Early multi-sensor analyses by Chin et al. (2014), integrating satellite products (TOMS, AVHRR, MODIS, MISR), AERONET observations, and GOCART simulations over the period 1980–2009, revealed pronounced AOD declines over Europe and the United States, primarily driven by reductions in sulfate aerosols. In contrast, increasing AOD over East and South Asia was attributed to rising anthropogenic emissions, partially masked by high background dust levels. Their study further highlighted the dominant influence of meteorological factors—particularly near-surface wind speed and soil moisture—in controlling dust variability over North Africa and the Middle East. Building on this work, Klingmüller et al. (2016) analysed MODIS Dark Target and Deep Blue AOD retrievals for 2000–2015 and reported a strong dust-driven increase in AOD over the Middle East during the early 2000s, linked to declining soil moisture, reduced precipitation, and enhanced surface winds, followed by a weakening of this signal after approximately 2012. Subsequently, Hammer et al. (2018) examined long-term changes in aerosol absorption and scattering using satellite observations and model simulations, demonstrating that regional AOD trends are strongly modulated by shifts in aerosol composition, particularly mineral dust, brown carbon, and secondary inorganic aerosols, underscoring the importance of aerosol-speciated analyses. Using long-term records from the MERRA-2 reanalysis (1980–2016) together with MODIS/Terra and MISR AOD retrievals for 2001–2016, Che et al. (2019) identified significant decreasing AOD trends over Europe and the eastern United States, contrasted by increasing trends over eastern China and South Asia, although the positive trend over China reversed during the most recent decade. Their analysis further showed that meteorological factors explained a substantial fraction (approximately 20–73%) of AOD variability in most regions, with sulfur dioxide (SO_2) dominating anthropogenic aerosol regimes and black or organic carbon driving variability in biomass-burning-influenced regions.

More recent satellite- and model-based studies have refined the role of aerosol type in shaping total AOD trends. Gui et al. (2021), using MODIS Terra and Aqua AOD data for 2001–2018, reported widespread global and regional decreases in seasonal AOD, largely attributable to reductions in small-sized and spherical aerosols, with notable exceptions over South Asia, the Middle East, and North Africa. In parallel, Logothetis et al. (2021) employed the MIDAS satellite-derived dust optical depth (DOD) dataset (Gkikas et al., 2021) for 2003–2017 and identified pronounced regional contrasts in dust trends, including declining dust activity over large parts of the Sahara, the Mediterranean Basin, and East Asia, and increasing dust loads over the central Sahara and the Arabian Peninsula. These findings emphasized the dominant contribution of dust to total AOD trends in dust-rich regions. Using CAMS reanalysis data for 2007–2019, Zhao et al. (2024) showed that declining AOD over eastern China, the eastern United States, and western Europe was primarily driven by reductions in sulfate aerosols, with additional contributions from decreased dust over eastern China. In contrast, increasing sulfate, black carbon, and organic matter concentrations over South Asia and Siberia partially offset these declines at the hemispheric scale. Most recently, Zhang

https://doi.org/10.5194/egusphere-2026-1107
Preprint. Discussion started: 6 March 2026

et al. (2025) analysed long-term AERONET observations (2000–2022) and reported widespread decreases in AOD and aerosol absorption over Europe, North America, and East Asia, alongside increasing AOD over northern India and the Arabian Peninsula, driven mainly by fine-mode scattering aerosols and mineral dust, respectively. Their aerosol-type classification further reinforced the importance of aerosol-speciated approaches for interpreting long-term AOD trends.

Collectively, these studies show that long-term AOD variability reflects the combined effects of emission controls, weather patterns, and changes in aerosol composition. There are notable regional differences between industrialized areas, where pollution measures have mostly reduced aerosol levels, and regions sensitive to weather variability, where AOD remains high or continues to rise. However, there is still a lot of uncertainty about how these factors interact to influence long-term aerosol trends and how reliable reanalysis-derived trends are compared to independent observations. In particular, the impact of satellite AOD assimilation on the magnitude, distribution, and stability of multi-decade trends has not been systematically measured.

The main goal of this study is to use the 22-year CAMS aerosol climatology to look into recent shifts in global and regional AOD while specifically evaluating the reliability of the reanalysis product. To do this, we start with a thorough evaluation of the latest ECMWF Atmospheric Composition Reanalysis (EAC4) against independent AERONET observations. This assessment is carried out (a) in terms of absolute statistical agreement using all available collocated measurements, (b) by comparing the added value of satellite AOD assimilation with a free-running control simulation (CTRL), and (c) by checking the consistency of long-term AOD trends between 178 AERONET stations and corresponding CAMS time series. Following this evaluation framework, we quantify global and regional AOD trends over the full 2003–2024 period, examine decadal shifts (2003–2013 and 2014–2024), and assess the temporal robustness of detected changes using sliding-window analyses. Furthermore, we apply aerosol-speciated trend diagnostics to quantify the relative contribution of dust, sulfate, organic matter, black carbon, and sea salt to the observed total AOD trends across 18 regions of interest representing distinct aerosol regimes. By explicitly linking product evaluation, assimilation impact assessment, and aerosol-type attribution of trends within a unified framework, this study provides new insight into both the drivers and the reliability of recent global and regional AOD evolution, extending previous ground-, satellite-, and model-based assessments.

2 Data and methods

2.1 CAMS reanalysis

The Copernicus Atmosphere Monitoring Service (CAMS; https://atmosphere.copernicus.eu) is a key component of the European Union's Copernicus Earth observation programme. Among its core products, CAMS delivers a global reanalysis of reactive trace gases and aerosols. The production of this reanalysis began in early 2017, with the historical period from 2003 to 2019 completed in January 2020 (Langerock et al., 2024). Since then, the dataset has been continuously extended and currently spans up to August 2025. The latest and fourth generation European Centre for Medium-Range Weather Forecasts (ECMWF) Atmospheric Composition Reanalysis (EAC4) is based on the Integrated Forecast System (IFS), which incorporates

https://doi.org/10.5194/egusphere-2026-1107
Preprint. Discussion started: 6 March 2026

the Carbon Bond 2005 (CB05) chemical mechanism (Huijnen et al., 2010), originally developed within the TM5 chemical transport model. The integration of CB05 into the ECMWF IFS resulted in the IFS-CB05 system, enhancing computational efficiency and improving the representation of interactions between meteorology and atmospheric chemistry (Flemming et al., 2015). The reanalysis is produced at a horizontal resolution of T255 (approximately 80 km), representing a substantial improvement over the earlier CAMS Interim Reanalysis (CIRA; Flemming et al., 2017), which was generated at T159 resolution (approximately 110 km).

The CAMS aerosol module includes 12 prognostic tracers that describe the mass mixing ratios of the main aerosol species. Sea salt (SS) and desert dust (DU) are each represented by three size bins (SS: 0.03–0.5, 0.5–5, and 5–20 μm; DU: 0.03–0.55, 0.55–0.9, and 0.9–20 μm), in addition to hydrophobic and hydrophilic organic matter (OM) and black carbon (BC), sulfate aerosols (SO_4), and their gaseous precursor sulfur dioxide (SO_2) (Morcrette et al., 2009). Within the ECMWF IFS, emissions of natural aerosols (DU and SS) are simulated online as a function of meteorological conditions, accounting for processes such as dust saltation over arid regions (Marticorena and Bergametti, 1995; Ginoux et al., 2001) and sea spray generation over the oceans (Monahan et al., 1986). Biomass-burning emissions are provided daily by the Global Fire Assimilation System version 1.2 (GFASv1.2; Kaiser et al., 2012), which is based on fire radiative power observations from the MODIS instruments aboard the Aqua and Terra satellites. Anthropogenic emissions are taken from the monthly MACCity inventory (Granier et al., 2011), with additional adjustments applied to enhance wintertime road traffic emissions over Europe and North America following Stein et al. (2014). Additionally, monthly mean biogenic emissions are derived from the hourly MEGAN-MERRA dataset (Sindelarova et al., 2014). Aerosol removal processes in the model include both dry and wet deposition. Dry deposition represents turbulent transfer to the surface and gravitational settling, while wet deposition encompasses in-cloud scavenging (rainout) and below-cloud scavenging (washout) associated with large-scale and convective precipitation. The model also accounts for hygroscopic growth, particularly the aging of carbonaceous aerosols from hydrophobic to hydrophilic states, as well as the chemical conversion of SO_2 to particulate sulfate (SO_4) using a simplified parameterization. A comprehensive description of aerosol emissions and removal processes is provided by Morcrette et al. (2009).

In addition to the assimilation of satellite observations for individual chemical species, EAC4 constrains the total aerosol mass through the assimilation of total AOD at 550 nm retrieved from the Moderate Resolution Imaging Spectroradiometer (MODIS; Levy et al., 2015) aboard the Aqua and Terra satellites for the period from 2003 to the present. AOD retrievals from the Advanced Along-Track Scanning Radiometer (AATSR; Popp et al., 2016) aboard Envisat were also assimilated from 2003 until March 2012. Following the loss of AATSR observations in April 2012, Inness et al. (2019) reported a small global increase in CAMS AOD, with more pronounced positive biases over Europe and North America. Further details on the data assimilation methodology are provided by Inness et al. (2015) for chemical trace gases and by Benedetti et al. (2009) for aerosols.

In addition to EAC4, a control simulation (CTRL) is performed using the same IFS-CB05 configuration as the EAC4, but with data assimilation of satellite retrievals switched off. The CTRL simulation therefore provides a baseline against which the impact of data assimilation on aerosol and chemical fields can be explicitly evaluated through direct comparison with EAC4.

https://doi.org/10.5194/egusphere-2026-1107
Preprint. Discussion started: 6 March 2026

In this study, the analysis focuses on CAMS AOD. Consequently, when referring to the CTRL simulation, the emphasis is placed on assessing the impact of satellite-based AOD assimilation. Although EAC4 also assimilates additional observations for different chemical species, the assimilation of AOD is expected to be the primary driver of differences between EAC4 and CTRL with respect to the simulated aerosol fields.

To better understand the relative contribution of each aerosol type to the total AOD on a regional scale, we computed the fractional values for each component. These fractions were estimated using the following formula:

$$FR_{type} = \frac{typeOD}{AOD}, \quad (1)$$

where *type* refers to the aerosol-speciated AOD: dust (DUOD), sea salt (SSOD), black carbon (BCOD), organic matter (OMOD), and sulfate (SUOD).

The global reanalysis data provided at a spatial resolution of 0.75° × 0.75° and a 3-hourly temporal resolution, were retrieved from the Copernicus Atmosphere Data Store (https://ads.atmosphere.copernicus.eu/, last access: 19 February 2026). Detailed guidance on data access and download procedures is available on the official website.

2.2 AERONET

The Aerosol Robotic Network (AERONET) is a global network comprising over 1,700 ground-based sun photometers that provide high-quality, multi-wavelength measurements of aerosol optical properties over the last 30 years (Holben et al., 1998; 2001). In this study, we use the latest version (V3) of Level 2.0 AERONET data, which provides cloud-screened and quality-assured direct-sun AOD retrievals with uncertainties of about ±0.01 in the visible and ±0.02 in the ultraviolet range (Giles et al., 2019; Sinyuk et al., 2020). The derived AOD measurements span a broad spectral range, typically from 340 to 1640 nm, covering both visible and near-infrared regions. These observations are provided both as daily averages and at the highest temporal resolution (i.e., all individual measurements at ~5 to 15 min), enabling a detailed characterization of aerosol columnar properties (Giles et al. 2019; Sinyuk et al., 2020). AERONET AOD retrievals serve a dual purpose in the present study, as they are used both to evaluate the EAC4 and CTRL AOD datasets and to assess their long-term trends.

Following Zhang et al. (2025), to ensure a robust and consistent analysis of long-term trend analysis, a comprehensive set of selection criteria was applied to identify AERONET stations with extensive and continuous data records during the 2003-2024 study period. Initially, for the low-AOD stations we excluded abnormally high AOD records (e.g., greater than 2.0) to avoid bias from extreme events. Monthly mean AOD values were calculated only when there were at least five valid daily observations distributed over three or more different days within the month, ensuring that monthly statistics accurately represent aerosol conditions. For yearly data sufficiency, stations were required to have at least ten years with a minimum of eight valid months per year to improve the reliability of long-term trend assessments; this threshold was relaxed to four valid months per year for polar stations located above 65° latitude to account for extended periods of solar darkness. To guarantee seasonal representativeness and capture intraseasonal variability, only stations with at least ten years of valid data for each climatological season (DJF, MAM, JJA, SON) were included. Additionally, following Inness et al. (2019), the Mauna Loa and

https://doi.org/10.5194/egusphere-2026-1107
Preprint. Discussion started: 6 March 2026

Mexico City stations were excluded due to biases introduced by volcanic sulfate emissions that pose challenges for global aerosol model representation. These biases may be attributed to the model's tendency to inject volcanic SO_2 at lower altitudes than observed, where SO_2 is more efficiently converted to sulfate through the sulfur oxidation pathways represented in CAMS IFS(CB05) chemical scheme (Huijnen et al., 2010; Innes et al., 2019).

The aforementioned selection criteria resulted in a total number of 178 AERONET stations, distributed across diverse regions of the world characterized by different aerosol conditions, providing a high-quality observational dataset suitable for robust global and regional aerosol trend assessments. The spatial distribution of the selected stations is shown in Fig. 1, where non-polar sites (black-outlined) and polar sites (cyan-outlined) are indicated separately. The background shading represents the annual mean AOD of the individual EAC4 aerosol components (i.e., dust, sea salt, organic matter, black carbon, and sulfate), thereby illustrating the dominant aerosol type in each region. Each station is additionally colored according to the number of available monthly observations used to estimate AOD trends, with the methodology for trend estimation described in Section 2.3.2.

Since CAMS does not assimilate ground-based AOD measurements from the AERONET network, AERONET provides a fully independent reference dataset for the evaluation of CAMS outputs (see Section 2.1). To enable consistent AOD comparisons between CAMS and AERONET stations, since AERONET does not provide observations at 550 nm, it was necessary to interpolate the AERONET AOD values using the Ångström power-law formula (Ångström, 1929):

$$AOD_{\lambda} = AOD_{\lambda 0} \cdot \left(\frac{\lambda_0}{\lambda}\right)^{\dot{a}}, \quad (2)$$

where λ refers to 550 nm, and λ_0 = 440 nm, and $\dot{a}$ is the Ångström exponent calculated using AOD measurements within the 440-675 nm interval (Eck et al., 1999; Giles et al., 2019)

https://doi.org/10.5194/egusphere-2026-1107
Preprint. Discussion started: 6 March 2026

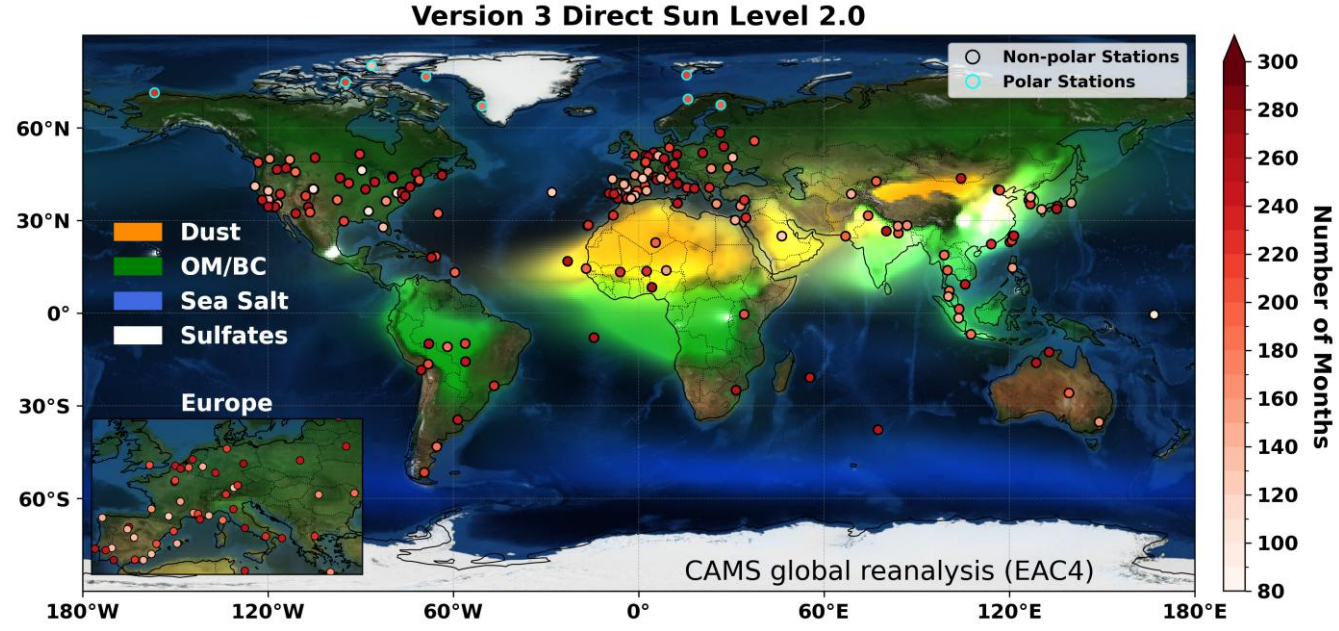

Figure 1: Locations of the AERONET stations fulfilling the criteria for extensive and continuous data records during the 2003-2024 period. Each station is coloured based on its available number of monthly records. The stations located northern of 65° N are outlined in cyan (polar stations), while all others are outlined in black (non-polar stations). For the same 22-year period, the background shows the annual mean aerosol optical depth (AOD) at 550 nm for each aerosol subtype based on EAC4, illustrating the spatial distribution of dust (orange), organic matter and black carbon (green), sea salt (blue), and sulfate (white). Map source: NASA Earth Observatory.

2.3 Statistical analysis

2.3.1 Evaluation method

The 3-hourly CAMS AOD fields (i.e., EAC4 and CTRL) were evaluated against the 178 AERONET stations presented in Fig. 1. For each station, the CAMS AOD from the nearest model grid cell was used for the spatial collocation. A sensitivity analysis was also performed using distance-weighted averages of the surrounding CAMS grid cells, but this approach did not lead to any noticeable differences in the results; therefore, for simplicity, only the nearest-grid-cell method is applied in this study. To ensure temporal consistency, instantaneous AERONET AOD observations within ±1 hour of each CAMS output time were averaged to obtain mean AOD values, which were then compared with the corresponding 3-hourly CAMS AOD fields.

The performance and uncertainties of the CAMS AOD are assessed using several statistical metrics, including the Pearson correlation coefficient (R; Eq. 3), mean absolute error (MAE; Eq. 4), root-mean-square error ($RMSE$; Eq. 5), relative mean bias (RMB; Eq. 6), percent mean fractional error ($\%MFE$; Eq. 7), percent fractional gross error ($\%FGE$; Eq. 8), and the index of agreement (IOA; Eq. 9), following the validation approach of Yumimoto et al. (2017) and Che et al. (2019).

The mathematical formulations of the evaluation metrics are provided below:

https://doi.org/10.5194/egusphere-2026-1107
Preprint. Discussion started: 6 March 2026

$$R = -\frac{\sum_{i=1}^{N}(O_i - \bar{O})(M_i - \bar{M})}{\sqrt{\sum_{i=1}^{N}(O_i - \bar{O})^2 \sum_{i=1}^{N}(M_i - \bar{M})^2}}\,, \tag{3}$$

$$MAE = \frac{1}{N}\sum_{i=1}^{N}|M_i - O_i|\,, \tag{4}$$

$$RMSE = \sqrt{\frac{1}{N}\sum_{i=1}^{N}(M_i - O_i)^2}\,, \tag{5}$$

$$RMB = \frac{\bar{M}}{\bar{O}}\,, \tag{6}$$

$$\%MFE = \frac{2}{N}\sum_{i=1}^{N}\frac{|M_i - O_i|}{M_i + O_i}\cdot 100\,, \tag{7}$$

$$\%FGE = \frac{2}{N}\sum_{i=1}^{N}\frac{M_i - O_i}{M_i + O_i}\cdot 100\,, \tag{8}$$

$$IOA = 1 - \frac{\sum_{i=1}^{N}(O_i - M_i)^2}{\sum_{i=1}^{N}(|O_i - \bar{O}| + |M_i - \bar{M}|)^2}\,, \tag{9}$$

where N represents the total number of matched AOD pairs between the model (M, i.e., EAC4 or CTRL) and the ground-based observations (O, i.e, AERONET). The R evaluates the strength and direction of the linear relationship between the model and observations, with values closer to 1 indicating stronger agreement. It ranges from -1 (perfect anticorrelation) to 1 (perfect correlation), with 0 indicating no linear correlation. The MAE provides a complementary measure of the average absolute difference between modelled and observed AOD, treating all deviations equally and therefore offering a more robust indication of general error magnitude, especially in the presence of outliers. The $RMSE$ quantifies the average magnitude of the error, giving more weight to larger discrepancies; lower values suggest better model performance. The RMB expresses the mean ratio between model and observed AOD and helps identify overall overestimation ($RMB > 1$) or underestimation ($RMB < 1$) tendencies. The $\%MFE$ quantifies overall modelling error without giving undue weight to outliers, with values ranging from 0% (perfect agreement) to 200%; values below 50% are generally considered acceptable for aerosol models. The $\%FGE$ assesses the symmetric bias between model and observations, distinguishing both underestimation and overestimation; like $\%MFE$, it ranges from 0% to 200%, with lower values indicating better performance. The IOA, introduced by Willmott (1981), measures the degree of model accuracy and ranges from 0 (no agreement) to 1 (perfect agreement), with values above 0.6 typically reflecting reasonable model skill. Using this combination of metrics allows for a balanced and nuanced evaluation, as each metric highlights different types of errors—whether absolute, relative, or directional—in the comparison between EAC4/CTRL and AERONET AOD.

https://doi.org/10.5194/egusphere-2026-1107
Preprint. Discussion started: 6 March 2026

2.3.2 Trend analysis

In this study, the AOD trend analysis is performed using the non-parametric Mann–Kendall (M-K) test (Mann, 1945; Kendall, 1975) combined with Sen's slope estimator (Sen, 1968). The Mann–Kendall test and Sen's slope estimator were implemented using the Python package pyMannKendall (Hussain et al., 2019; https://github.com/mmhs013/pyMannKendall). The M-K test is commonly used to evaluate the statistical significance of monotonic trends in environmental time series, as it does not require the data to follow a specific distribution. Sen's slope (k) provides a robust estimate of the magnitude and direction of the trend by calculating the median of all pairwise slopes between data points, while the M–K test evaluates the statistical significance and direction of the trend (Gui et al., 2021). The Sen's slope is expressed as follows (Sen, 1968):

$$k = median\left(\frac{X_j - X_i}{t_j - t_i}\right), \forall\, j > i \tag{10}$$

where X_i and X_j are the values of the variables (in our case, the monthly AOD anomalies, obtained by deseasonalizing the monthly data through subtraction of the long-term monthly means) at times t_i and t_j, respectively.

The M-K trend test, is calculated as follows:

$$S = \sum_{i=1}^{N-1} \sum_{j=i+1}^{N} sgn\left(X_j - X_i\right), \tag{11}$$

where N represents the total number of X values used for the estimation of the trend. From Eq. (11) it is obvious that the M-K trend test analyses the difference in sign between earlier and later data points in the time series. The $sgn(\,)$ is the sign function defined as:

$$sgn\left(X_j - X_i\right) = \begin{cases} +1, & X_j - X_i > 0 \\ 0, & X_j - X_i = 0 \\ -1, & X_j - X_i < 0 \end{cases} \tag{12}$$

The statistic S is approximately normally distributed with a mean of zero under the null hypothesis of no trend (Li, 2020). Its variance, which accounts for tied groups within the data, can be computed using the following formula:

$$Var(S) = \frac{N(N-1)(2N+5) - \sum_{j=1}^{P} t_j\left(t_j - 1\right)\left(t_j + 5\right)}{18}, \tag{13}$$

where P is the number of tied groups (repeated values in the time series).

Finally, the trend test is performed through the test statistic Z_{MK}, which is estimated through the formula:

$$Z_{MK} = \begin{cases} \dfrac{S-1}{\sqrt{Var(S)}}, & S > 0 \\ 0, & S = 0 \\ \dfrac{S+1}{\sqrt{Var(S)}}, & S < 0 \end{cases} \tag{14}$$

The statistical significance of the trend is determined by comparing the absolute value of Z_{MK} to a critical value from the standard normal distribution. If $|Z_{MK}| > Z_{critical}$, the null hypothesis of no trend is rejected, indicating that the observed trend

https://doi.org/10.5194/egusphere-2026-1107
Preprint. Discussion started: 6 March 2026

is statistically significant. Conversely, if $|Z_{MK}| \leq Z_{critical}$, the null hypothesis cannot be rejected, and the trend is considered not statistically significant. For the present study, the 95% significance level was considered with the critical value of ± 1.96. It should be noted that the M–K test assumes serial independence of the data, although some degree of autocorrelation is common in climatic time series. When autocorrelation is present in a time series, it can significantly affect the power and reliability of the MK test, particularly increasing the likelihood of detecting a false trend in the presence of positive autocorrelation (Kulkarni and von Storch, 1992; von Storch, 1995; Yue et al., 2002; Li et al., 2014; Collaud Coen et al., 2020). To address this, pre-whitening techniques are commonly applied to remove the influence of serial correlation before conducting trend analysis. In this study, we use the classical pre-whitening method proposed by von Storch (1995) and evaluated in depth by Yue and Wang (2002). Their simulation-based analysis revealed that while pre-whitening can effectively remove lag 1 autocorrelation, particularly in short to medium-length datasets where autocorrelation can significantly bias trend detection.

In the current study, the trend analysis is applied at multiple geospatial and temporal scales. Specifically, we estimate the trends of the AOD globally, as well as over selected ROIs dominated by different aerosol species. To capture temporal variability and assess the evolution of trends over time, the analysis was performed not only for the complete 2003–2024 study period but also for shorter sub-periods. Additionally, we assessed the EAC4/CTRL AOD trends against the AERONET observations to enable a direct comparison between model- and ground-based aerosol load trends over the 2003–2024 period.

2.4 Regions of Interest (ROIs)

Despite the global perspective, we further defined 18 regions of interest (ROIs) to assess long-term regional trends while accounting for variability in anthropogenic and natural aerosol loading. The ROIs were selected based on the dominant fractional contribution of CAMS speciated AOD components (dust, sea salt, black carbon, organic matter, and sulfate) to total AOD, as shown in Fig. 2, following the Eq. (1), and consistent with regional definitions adopted in previous studies (e.g., Chen et al. 2019; Gui et al. 2021). Regions were assigned to the aerosol type exhibiting the largest systematic contribution to total AOD, ensuring that each ROI represents a well-established aerosol-dominant regime. The 18 ROIs comprise three mineral dust–dominated regions: North Africa (NAC), the Middle East (ME), and northwestern China (NWC); five biomass-burning–dominated regions: Amazon (AMZ), Central Africa (CA), Southeast Asia (SEA), Canadian fires zone (CFZ), and Siberian fires zone (SFZ); five anthropogenic-pollution–dominated regions: eastern China (EC), South Asia (SA), eastern United States (EUS), western United States (WUS), and Central Europe (CEU); two sea-salt–dominated oceanic regions: South Pacific Ocean (SPO) and South Atlantic–Indian Ocean (SAIO); and three mixed regimes influenced by seasonal dust transport: Atlantic dust transport zone (ADTZ), western Mediterranean (WME), and eastern Mediterranean (EME). The geographical boundaries of all ROIs are provided in Table 1.

ROIs	Geographical boundaries	Dominant Aerosol Regime
North Africa (NAC)	9.5–31°N, 13.5 W–25°E	Mineral dust
Middle East (ME)	12.5–38°N, 36–65°E	Mineral dust

https://doi.org/10.5194/egusphere-2026-1107
Preprint. Discussion started: 6 March 2026

Northwestern China (NWC)	35-44ºN, 73.5–98.5ºE	Mineral dust
Amazon (AMZ)	0–15.5ºS, 49.5–75.5ºW	Biomass burning
Central Africa (CA)	4ºN 14ºS, 14.5–36ºE	Biomass burning
Southeast Asia (SEA)	9ºS 10ºN, 96–127ºE	Biomass burning
Canadian fires zone (CFZ)	68-125ºN, 50-65ºW	Biomass burning
Siberian fires zone (SFZ)	60–70ºN, 90–135ºE	Biomass burning
Eastern China (EC)	22–44ºN, 104–121ºE	Urban/Pollution
South Asia (SA)	10–30ºN, 72–90ºE	Urban/Pollution
Eastern United states (EUS)	25–45ºN, 72–99ºW	Urban/Pollution
Western United states (WUS)	35–48ºN, 100–125ºW	Urban/Pollution
Central Europe (CEU)	44–58ºN, 0–33ºE	Urban/Pollution
South Pacific Ocean (SPO)	47–65ºS, 80–150ºW	Sea salt
South Atlantic-Indian Ocean (SAIO)	45–60ºS, 10ºW 140ºE	Sea salt
Atlantic Dust Transport zone (ADTZ)	10–30ºN, 18–62ºW	Mixed/ Seasonal Dust Outbreaks
Western Mediterranean (WME)	34–43ºN, 11.5ºW–13ºE	Mixed/ Seasonal Dust Outbreaks
Eastern Mediterranean (EME)	32–43ºN, 14–35ºE	Mixed/ Seasonal Dust Outbreaks

Table 1: Geographical boundaries of the 18 regions of interest (ROIs) considered in this study and their associated dominant aerosol regimes, based on EAC4 climatology for the period 2003–2024.

The 18 ROIs are presented in Fig. 2, along with the computed climatological mean EAC4 AOD (2003–2024) and the fractional contribution of each aerosol subtype (i.e., dust, sea salt, organic matter, black carbon, and sulfate – Following Eq. (1). Figure 2 highlights both the spatial variability in aerosol loading and the dominant aerosol types across different climatic and geographic regions.

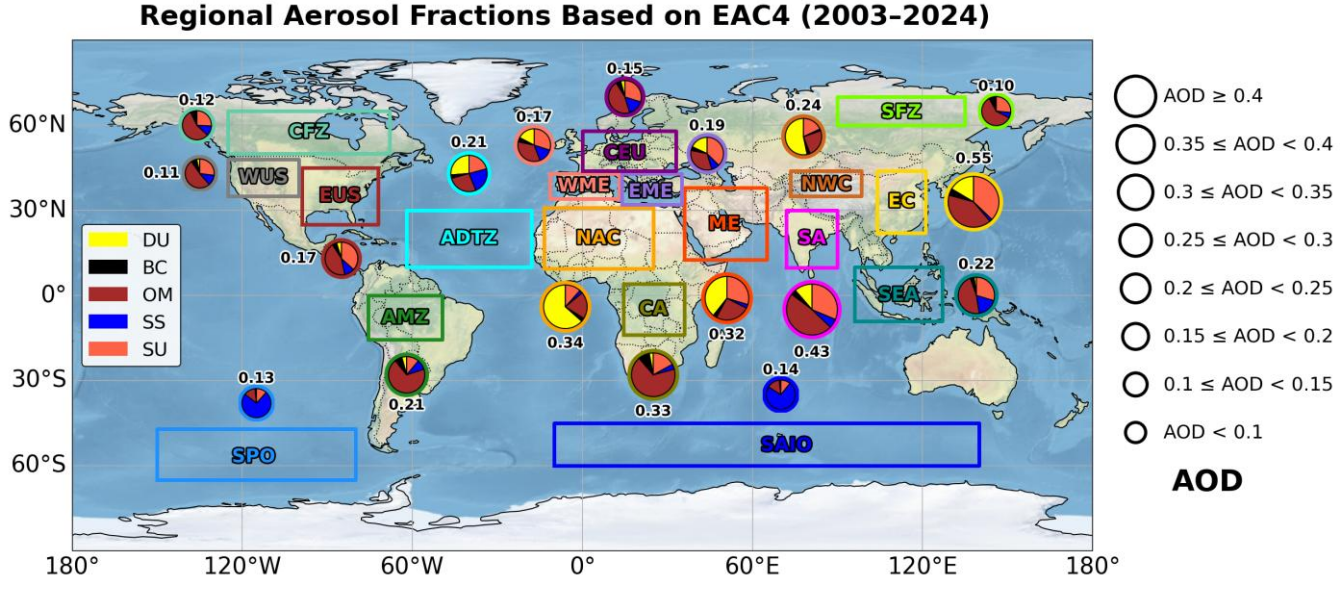

https://doi.org/10.5194/egusphere-2026-1107
Preprint. Discussion started: 6 March 2026

Figure 2: The geographical locations of the 18 regions of interest (ROIs): North Africa (NAC), the Middle East (ME), northwestern China (NWC), Amazon (AMZ), Central Africa (CA), Southeast Asia (SEA), Canadian fires zone (CFZ), Siberian fires zone (SFZ), eastern United States (EUS), western United States (WUS), central Europe (CEU), South Pacific Ocean (SPO), South Atlantic–Indian Ocean (SAIO), Atlantic Dust Transport Zone (ADTZ), western Mediterranean (WME), eastern Mediterranean (EME), South Asia (SA), and eastern China (EC). Next to each region, a pie chart illustrates the fractional contribution of five major aerosol subtypes based on EAC4 (2003–2024): dust (DU, yellow), black carbon (BC, black), organic matter (OM, brown), sea salt (SS, blue), and sulfate (SU, coral). The size of each pie chart is proportional to the regional climatological mean aerosol optical depth (AOD) over the 2003–2024 period based on EAC4. The legend at the right of the figure indicates the scaling of pie chart size with respect to the different AOD magnitudes, while the corresponding climatological AOD values for each region are also displayed near each pie chart.

3 Results

3.1 Aerosol Optical Depth evaluation

3.1.1 Global scale

First, we assessed the global performance of EAC4 and CTRL AOD against observations from the 178 AERONET stations. As illustrated in Fig. 3, both CAMS configurations show generally good agreement with ground-based AERONET measurements. However, EAC4 (Fig. 3b) demonstrates superior performance, characterized by smaller deviations from the observations (R = 0.84, RMSE = 0.12, MAE = 0.07, MFE = 46.1%, FGE = 0.7%, RMB = 1.0, and IOA = 0.9, based on 1,657,564 collocated data pairs). In contrast, the CTRL simulation (Fig. 3a), which does not assimilate satellite observations, captures the observed AOD variability but with reduced skill (R = 0.75, RMSE = 0.16, MAE = 0.08, MFE = 53.8%, FGE = 20.8%, RMB = 0.87, and IOA = 0.85). These results clearly demonstrate that the assimilation of satellite-based observations in EAC4 substantially improves the agreement between modelled and ground-based AOD observations.

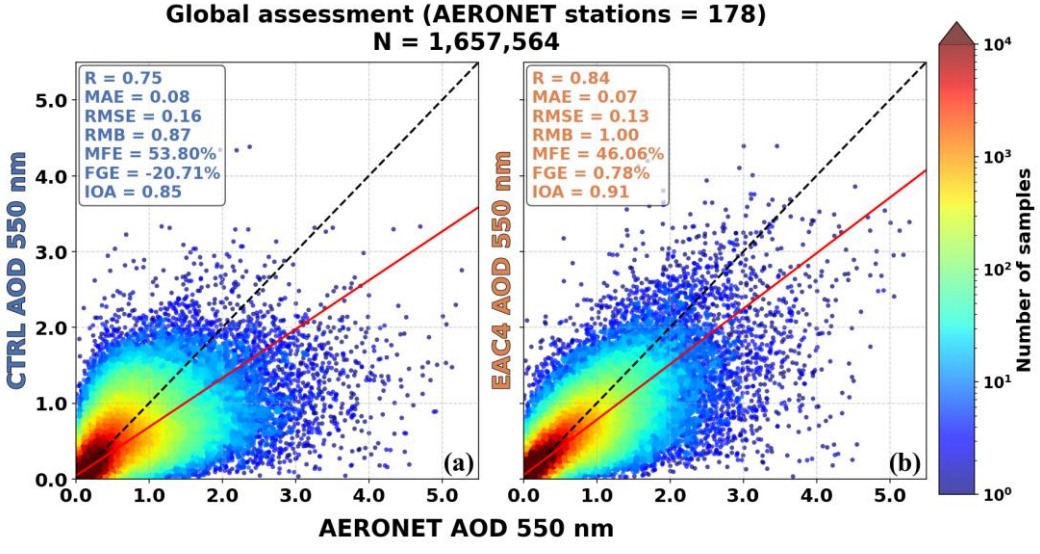

Figure 3: Evaluation of (a) CTRL, and (b) EAC4 AOD against the 178 ground-based AERONET stations on a global scale. The scatter points are coloured according to the number of collocated samples in each bin (N = total number of collocated data points). The statistical metrics for the AOD comparison of each panel include the correlation coefficient (R), the mean absolute error (MAE),

https://doi.org/10.5194/egusphere-2026-1107
Preprint. Discussion started: 6 March 2026

the root-mean-square error (RMSE), the relative mean bias (RMB), the mean fractional error expressed as a percentage (%MFE), and the fractional gross error expressed as a percentage (%FGE), and (f) index of agreement (IOA). The black dashed line represents the 1:1 line, while the red line shows the linear regression fit.

As an alternative and more detailed comparison of the two CAMS configurations, we analysed the AOD differences (ΔAOD), defined as EAC4 − AERONET and CTRL − AERONET, as a function of AERONET AOD. The station selection procedure is described in Section 2.2, and the geographic distribution of the sites is shown in Fig. 1. Figure 4b presents box–whisker plots of ΔAOD (y-axis)—with EAC4 − AERONET shown in orange and CTRL − AERONET in blue—plotted against the corresponding AERONET AOD values (x-axis). The AERONET AOD is binned into ten equal-width intervals (0.0–0.1, 0.1–0.2, etc.), with the final bin including all cases where AERONET AOD exceeds 0.9. The number of collocated observations within each AOD bin is indicated above the respective classes.

Figure 4a reveals several important features regarding the performance of the EAC4 vs CTRL AOD products against AERONET across the different AOD classes. At low AERONET AOD values (0.0–0.2), both products show very small ΔAOD values centred near zero, indicating good overall agreement with AERONET. These low-AOD regimes also contain most of the global collocated samples, as reflected in the high sample counts in the first bins (~72.5 % of the total sample). As the AERONET AOD increases, systematic differences emerge: both CAMS products increasingly underestimate AOD, but the negative bias is clearly more pronounced in the CTRL. The ΔAOD values for the CTRL decrease more steeply with increasing AERONET AOD, demonstrating that the underestimation intensifies under moderate and high aerosol loadings. In contrast, EAC4 exhibits a systematically smaller negative bias across all bins, showing that the assimilation of satellite AOD substantially mitigates this tendency. The spread of the box–whisker distributions also grow with increasing AOD, reflecting greater variability and uncertainty under high-aerosol conditions; however, the EAC4 distributions remain consistently narrower than those of the CTRL, further illustrating the stabilizing effect of the assimilation. At very high AOD (>0.7), where sample sizes become much smaller, the underestimation becomes substantial for both CAMS products, although EAC4 still performs noticeably better than the CTRL. Overall, while both CAMS products reproduce low-AOD conditions well, EAC4 provides a significantly improved representation of AOD at moderate and high aerosol loadings, correcting a large part of the systematic underestimation present in the CTRL.

Additionally, Fig. 4b presents the histograms of ΔAOD, together with the corresponding linear-regression statistics for the AOD evaluation (EAC4 vs. AERONET and CTRL vs. AERONET). The metrics are shown separately for EAC4 (orange fonts) and CTRL (blue fonts). The definitions of these metrics are provided in detail in Section 2.3.1. The evaluation metrics clearly demonstrate that EAC4 achieves substantially improved agreement with AERONET relative to the CTRL. In addition to its higher correlation and lower MAE and RMSE, EAC4 exhibits an RMB of 1.00 and an IOA of 0.91, reflecting an almost perfect correction of mean bias and a markedly improved consistency in temporal variability. The ΔAOD distribution for EAC4 is also more symmetric and sharply centred near zero, with noticeably narrower spread and greatly reduced extreme negative and positive deviations, indicating a substantial reduction in overall error magnitude. The most pronounced improvement appears in the fractional gross error (%FGE), which increases from −20.7% (CTRL) to 0.78% (EAC4). This substantial reduction

https://doi.org/10.5194/egusphere-2026-1107
Preprint. Discussion started: 6 March 2026

demonstrates that the systematic underestimation characterizing the CTRL is largely eliminated through the satellite assimilation in EAC4.

The pie charts shown on the right-hand side of Fig. 4b depict the relative contributions of the CAMS aerosol components (DU, BC, OM, SS, and SU) to the total AOD for EAC4 and CTRL, as estimated using Eq. (1) averaged over the 178 AERONET stations included in this study. A pronounced reduction in the dust fraction is evident in EAC4 (~19%) compared with CTRL (~29%), corresponding to an approximately 50% larger relative dust contribution in the CTRL simulation and indicating a tendency for CTRL to overestimate the contribution of mineral dust to the total AOD. In contrast, EAC4 shows a substantially higher contribution from organic matter (44% compared with 38% in CTRL), together with enhanced contributions from black carbon (~23%), sea salt (~19%), and, to a lesser extent, sulfate (~5%) relative to CTRL. These changes in aerosol-speciated fractions reflect a redistribution of the total AOD budget toward fine-mode and marine aerosols driven by the assimilation of satellite-based AOD observations. Consistent with this redistribution, EAC4 reproduces the AERONET mean AOD with remarkable accuracy (0.185 versus 0.184), whereas CTRL clearly underestimates the mean AOD. The standard deviation of AOD in EAC4 is also slightly lower than that of AERONET, suggesting a moderate smoothing effect associated with AOD assimilation, while CTRL underestimates both the mean and the variability of AOD.

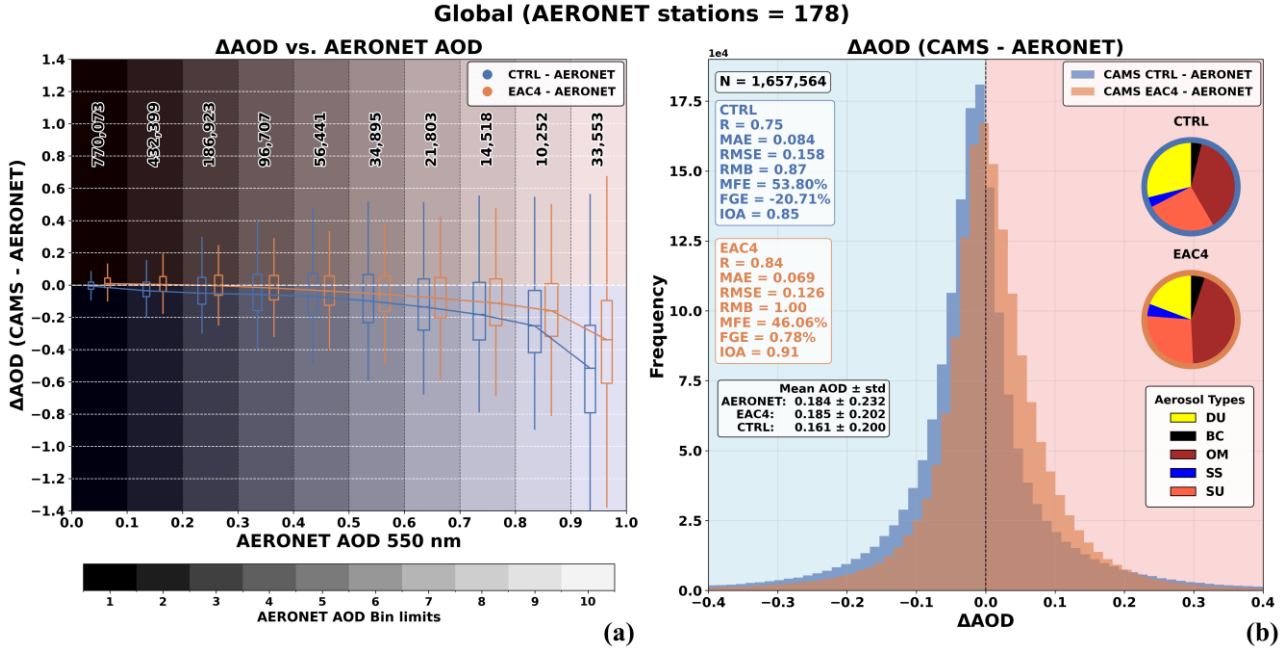

Figure 4: (a) Box–whisker plots of the AOD differences (ΔAOD) (y-axis) (displaying the 75/25 percentiles at the boxes, and the median in the centre line, while the whiskers are displaying the ±1.5 IQR from the 25/75 percentiles, respectively) between CTRL – AERONET (blue) and EAC4 – AERONET (orange) as a function of the AERONET AOD (x-axis). The AERONET AOD values are grouped into equal-width classes (0.0–0.1, 0.1–0.2, …), with the number of ΔAOD pairs shown above each bin. The background shading highlights the individual AOD classes. (b) Histograms of ΔAOD for CTRL (blue) and EAC4 (orange). The total number of collocated pairs (N) and the evaluation metrics (R, MAE, RMSE, RMB, %MFE, %FGE, IOA) are reported separately for each product. Pie charts indicate the relative contributions of the CAMS aerosol subtypes (DU, BC, OM, SS, SU) to the total AOD for

https://doi.org/10.5194/egusphere-2026-1107
Preprint. Discussion started: 6 March 2026

CTRL and EAC4. The mean AERONET AOD, together with the mean ± standard deviation of CTRL and EAC4, are also shown. Background colours in both panels denote over- and underestimation.

3.1.2 Station-level evaluation

To further assess model performance at the station level, site-specific evaluation metrics were computed for all AERONET stations and grouped into three categories: measures of agreement (R and IOA), absolute error metrics (MAE and RMSE), and relative and bias-related metrics (RMB, %MFE, and %FGE). The full spatial distributions of these metrics for EAC4 and CTRL are shown in Figs. S1–S3 of the Supplement.

Overall, EAC4 exhibits consistently strong performance across the AERONET network. The majority of stations show high correlation and agreement with AERONET observations, low absolute errors, and relatively small biases. Most sites are characterized by RMSE values below 0.20 and MAE values below 0.10, while mean biases remain close to unity at a large fraction of stations. Relative error metrics further indicate that large fractional errors are uncommon, confirming that EAC4 captures both the magnitude and variability of AOD across a wide range of aerosol regimes. Despite some localized discrepancies, these results demonstrate robust station-level performance of EAC4 on a global scale.

In contrast, the CTRL configuration, shows systematically weaker performance at many stations. Compared with EAC4, CTRL exhibits lower correlations, larger absolute and relative errors, and stronger systematic biases, with a pronounced tendency to underestimate AOD. The degradation in performance is evident across all metric categories, indicating that the absence of satellite assimilation substantially limits the model's ability to reproduce observed AOD variability at the site level. Taken together, the station-level evaluation confirms that the assimilation of satellite observations in EAC4 leads to a marked improvement in the representation of AOD relative to CTRL.

3.1.3 Regional scale evaluation

To assess the reliability of AOD over the selected regions of interest (ROIs; Fig. 5), which are characterized by different dominant aerosol types, the regional performance of both CAMS configurations (EAC4 and CTRL) was evaluated against AERONET observations. A summary of the regional statistics, including the number of AERONET sites, total sample size, mean AERONET AOD, and evaluation metrics for CTRL and EAC4 (R, MAE, RMSE, RMB, %MFE, %FGE, and IOA), is provided in Table S1 of the Supplement. ROIs denoted by "–" correspond to regions excluded from the analysis due to the absence of AERONET stations (SFZ, SPO, and SAIO). In addition, regional scatterplots for both CAMS configurations are also provided (Figs. S4–S5).

Overall, CAMS reproduces the spatial and temporal variability of AOD reasonably well across most ROIs; however, systematic differences emerge between the two configurations. In nearly all regions, EAC4 exhibits higher correlation and agreement with AERONET observations, together with lower absolute and relative errors, confirming that assimilation consistently improves regional model performance.

https://doi.org/10.5194/egusphere-2026-1107
Preprint. Discussion started: 6 March 2026

In dust-dominated regions such as North Africa (NAC), CTRL substantially underestimates AOD (RMB = 0.91), while EAC4 shows an even stronger underestimation (RMB = 0.84), but with markedly improved temporal agreement (R = 0.79 vs 0.58; IOA = 0.83 vs 0.69) and reduced errors (MAE = 0.13 vs 0.17; RMSE = 0.22 vs 0.28). This indicates that assimilation improves the representation of day-to-day variability despite the persistent underestimation of coarse-mode dust. Such underestimation is consistent with previous studies showing that global models tend to under-represent coarse dust particles (≥ 5–10 µm) and are affected by uncertainties in removal processes and wind biases, particularly away from source regions (Adebiyi and Kok, 2020; Ansmann et al., 2017; Evan, 2018). Over the Middle East, EAC4 improves all evaluation metrics (R = 0.83 vs 0.65; RMB = 0.96 vs 1.13; IOA = 0.89 vs 0.76), indicating enhanced temporal agreement and reduced bias. In regions influenced by long-range transported Saharan dust (e.g., ADTZ), EAC4 shows excellent agreement with AERONET (R = 0.91, RMB = 1.09, IOA = 0.95), clearly outperforming CTRL.

In biomass-burning regions, both configurations capture AOD variability reasonably well, but CTRL generally exhibits stronger biases and larger errors. Over the Amazon (AMZ), EAC4 performs exceptionally well (R = 0.93, IOA = 0.96), while over the Canadian Fire Zone (CFZ), CTRL strongly underestimates AOD (RMB = 0.56). EAC4 substantially reduces errors and improves agreement (IOA increases from 0.71 to 0.85), although a tendency toward overestimation (RMB = 1.27) remains, consistent with known uncertainties in GFAS emissions related to fire persistence assumptions during periods of missing fire radiative power (FRP) observations (Kaufman et al., 2003; Di Giuseppe et al., 2017). Over Southeast Asia, assimilation improves correlation and error statistics, although challenges persist due to possible cloud contamination and complex terrain limiting satellite availability (Zhang et al., 2022).

For pollution-dominated regions, EAC4 again consistently outperforms CTRL. Over Eastern China, assimilation improves both correlation (R = 0.85 vs 0.74) and RMSE (0.26 vs 0.33), while reducing the mean bias toward unity (RMB = 0.99 vs 1.10). Similar improvements are observed over Southern Africa, the Eastern and Western United States, and Central Europe. Over the Mediterranean basins (WME and EME), EAC4 improves all metrics, although episodic dust transport continues to affect short-term agreement. Residual discrepancies may partly reflect uncertainties in the MACCity anthropogenic emissions inventory, which does not account for recent emission reductions and therefore cannot be fully corrected through AOD assimilation alone (Granier et al., 2011).

As a more detailed diagnostic, we analyse the behaviour of the AOD differences (ΔAOD = CAMS − AERONET) as a function of AERONET AOD, resolved into ten AERONET AOD bins and examined separately for each ROI and for both EAC4 and CTRL (Figs. 5–6). In addition, regional ΔAOD histograms summarize the overall bias characteristics (see also Table S1). The corresponding ΔAOD histograms for each of the ten AERONET AOD bins are provided in the Supplement (Figs. S6–S15), allowing a direct assessment of how uneven sampling across AERONET AOD bins influences the aggregated regional statistics, as illustrated below for North Africa.

Across nearly all ROIs, the ΔAOD histograms reveal that CTRL is characterized by broader distributions and stronger systematic biases, whereas EAC4 produces narrower and more symmetric distributions centred closer to zero. This indicates that the assimilation of satellite AOD reduces both the mean bias and the variability of model–observation differences. The

https://doi.org/10.5194/egusphere-2026-1107
Preprint. Discussion started: 6 March 2026

ΔAOD–AERONET relationships further show a consistent tendency in CTRL toward increasing AOD underestimation with rising AERONET AOD, particularly for values exceeding ~0.3–0.4. In contrast, EAC4 exhibits a much weaker dependence of ΔAOD on aerosol loading, demonstrating that assimilation stabilizes model performance across a wide range of AOD conditions. Only at the highest AOD values—where sample sizes decrease—do both configurations exhibit stronger negative excursions, although the underestimation remains systematically smaller in EAC4.

In major dust-dominated regions, the regional ΔAOD distributions indicate predominantly negative CTRL biases that intensify with increasing AOD, reflecting an under-representation of dust loading. EAC4 substantially reduces this negative bias and narrows the ΔAOD spread, although a residual underestimation persists, particularly over North Africa (NAC), consistent with known limitations in representing coarse-mode dust. In regions dominated by transported finer Saharan dust, the ΔAOD distributions in EAC4 become more symmetric, suggesting improved constraints on dust outflow and long-range transport. An apparent inconsistency arises for NAC when comparing the binned ΔAOD analysis with the bulk statistics in Table S1, where EAC4 appears to underestimate AOD more strongly than CTRL. This discrepancy is largely explained by uneven sampling across AERONET AOD bins. For AERONET AOD between 0.1 and 0.4—accounting for roughly 50% of the collocations—a substantial fraction of CTRL boxplots lies above zero, indicating weak overestimation or reduced negative bias. These frequent low-to-moderate AOD cases disproportionately influence the aggregated metrics, partly compensating for the strong underestimation at high AOD (≥ 0.7), which represents only ~14% of the samples. Consequently, bulk statistics can give the misleading impression that CTRL performs better overall, whereas the binned analysis clearly shows that EAC4 reduces the negative bias during the strongest dust events (Figs. S6a–S15a). A different behavior is observed over the Middle East (ME), where CTRL exhibits persistent overestimation across a broad AOD range (approximately 0.0–0.5), which is not offset by high-AOD underestimation. As a result, no similar contradiction between bulk and binned statistics arises for this region.

In biomass-burning regions, CTRL again displays wider ΔAOD distributions and larger departures from zero, particularly during intense smoke episodes. EAC4 reduces both the central bias and the spread of ΔAOD, most notably over the Amazon (AMZ) and Southeast Asia (SEA), where smoke loadings exhibit strong seasonal variability. Over the Canadian Fire Zone (CFZ), CTRL shows positive ΔAOD tails consistent with overestimated smoke emissions, while EAC4 shifts the ΔAOD distribution closer to zero and suppresses large outliers, indicating that assimilation corrects much of the excess aerosol loading, albeit with a slight tendency toward overestimation.

In regions dominated by anthropogenic emissions, CTRL exhibits pronounced AOD-dependent biases with contrasting regional behaviour. Over Eastern China (EC) and Southern Asia (SA), CTRL tends to overestimate AOD at low to moderate AERONET AOD, whereas over Central Europe (CEU), the Eastern United States (EUS), and the Western United States (WUS), the bias is predominantly negative across most of the AOD range. In all pollution-dominated regions, CTRL shows an increasingly negative ΔAOD at higher AOD, reflected in a negative ΔAOD–AERONET slope. EAC4 consistently mitigates these biases by reducing both low-AOD overestimation and high-AOD underestimation, yielding ΔAOD distributions that are more symmetric and centred closer to zero. This behaviour suggests that, in the absence of assimilation constraints, the control simulation is more sensitive to prescribed anthropogenic emissions and less responsive to regional mitigation effects. Although

https://doi.org/10.5194/egusphere-2026-1107
Preprint. Discussion started: 6 March 2026

some spread and weak residual biases remain—particularly in regions characterized by complex aerosol mixtures such as the Mediterranean basin—the ΔAOD distributions clearly demonstrate that assimilation improves both the representativeness of the mean AOD and the stability of day-to-day variability.

Finally, the regional pie charts in Fig. 6 illustrate how satellite AOD assimilation modifies the relative contributions of individual aerosol components (DU, BC, OM, SS, and SU) to the total AOD, estimated following Eq. (1). Across nearly all ROIs, the fractional contribution of dust is systematically lower in EAC4 than in CTRL, while the contribution of OM generally increases. This effect is most pronounced in dust-dominated regions. Over North Africa, for example, dust contributes 80.1% of the total AOD in CTRL but only 67.3% in EAC4, while the organic matter contribution increases from 17.8% to 21.1%. Similar shifts are observed over the Middle East, the Mediterranean basins, and the ATDZ, where the strongly dust-dominated aerosol mixture in CTRL becomes more balanced in EAC4, with increased contributions from SU, SS, and OM. In biomass-burning regions, OM remain dominant in both configurations, with only minor differences between simulations, while in pollution-dominated regions such as EC, CEU, and the EUS, assimilation similarly reduces the DU fraction and leads to a more even partitioning among OM, SU, and UU. Overall, these results show that satellite AOD assimilation substantially redistributes the simulated aerosol burden in addition to improving agreement with AERONET in terms of total AOD. However, since the assimilation system optimizes the fit to total AOD by adjusting the total aerosol mixing ratio while keeping the relative fractional contributions of individual species fixed within the assimilation window, the aerosol speciation itself is not independently constrained by observations. Therefore, the differences in composition between EAC4 and CTRL should be interpreted with caution, as they may reflect structural aspects of the assimilation approach rather than a true improvement in aerosol speciation.

https://doi.org/10.5194/egusphere-2026-1107
Preprint. Discussion started: 6 March 2026

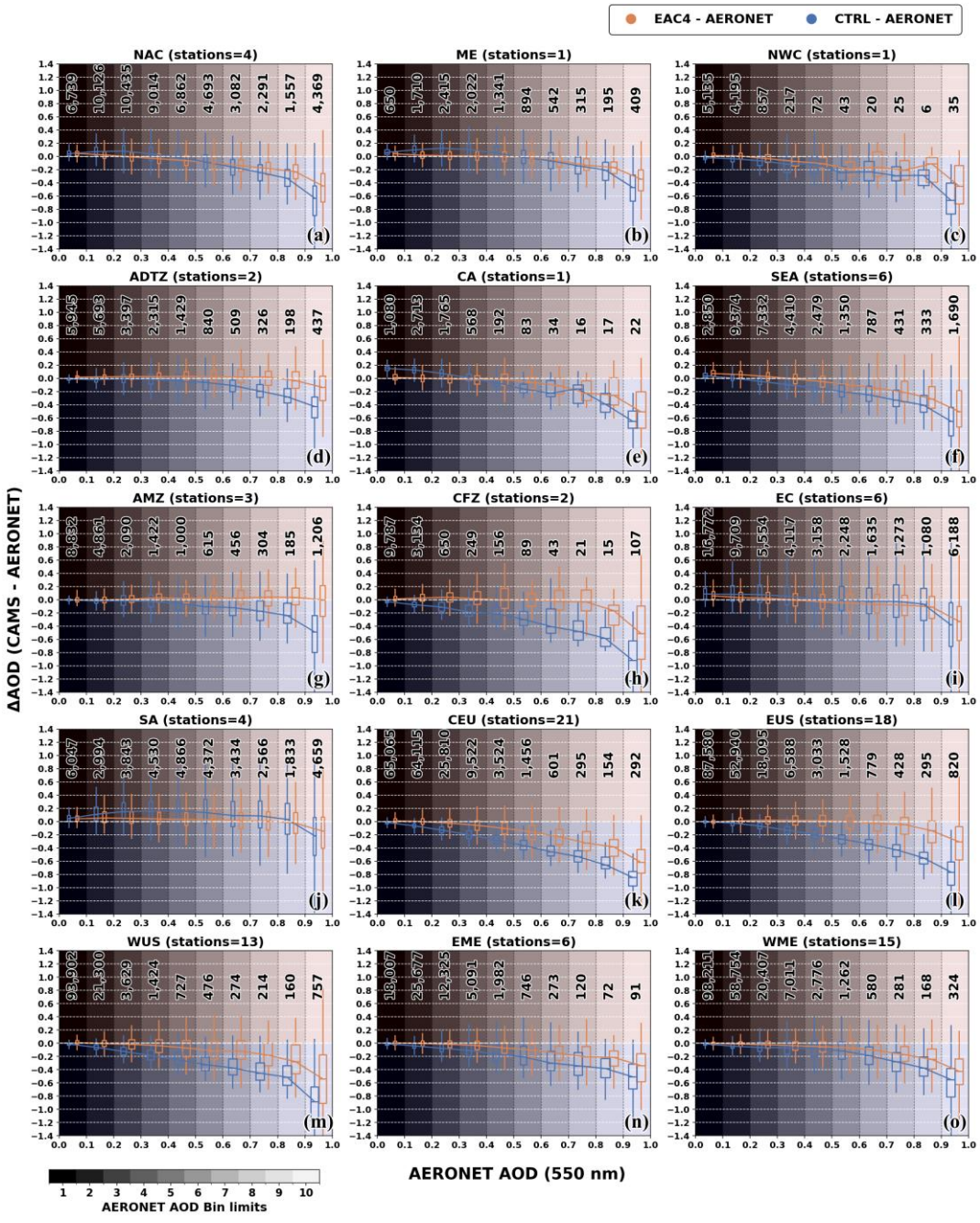

Figure 5: Regional box–whisker plots of the AOD differences (ΔAOD) (y-axis) (displaying the 75/25 percentiles at the boxes, and the median in the centre line, while the whiskers are displaying the ±1.5 IQR from the 25/75 percentiles, respectively) between CTRL – AERONET (blue) and EAC4 – AERONET (orange) as a function of the AERONET AOD (x-axis). The AERONET AOD values are grouped into equal-width classes (0.0–0.1, 0.1–0.2, …), with the number of ΔAOD pairs shown above each bin. The background shading highlights the individual AOD classes. Background colours in both panels denote over- and underestimation.

https://doi.org/10.5194/egusphere-2026-1107
Preprint. Discussion started: 6 March 2026

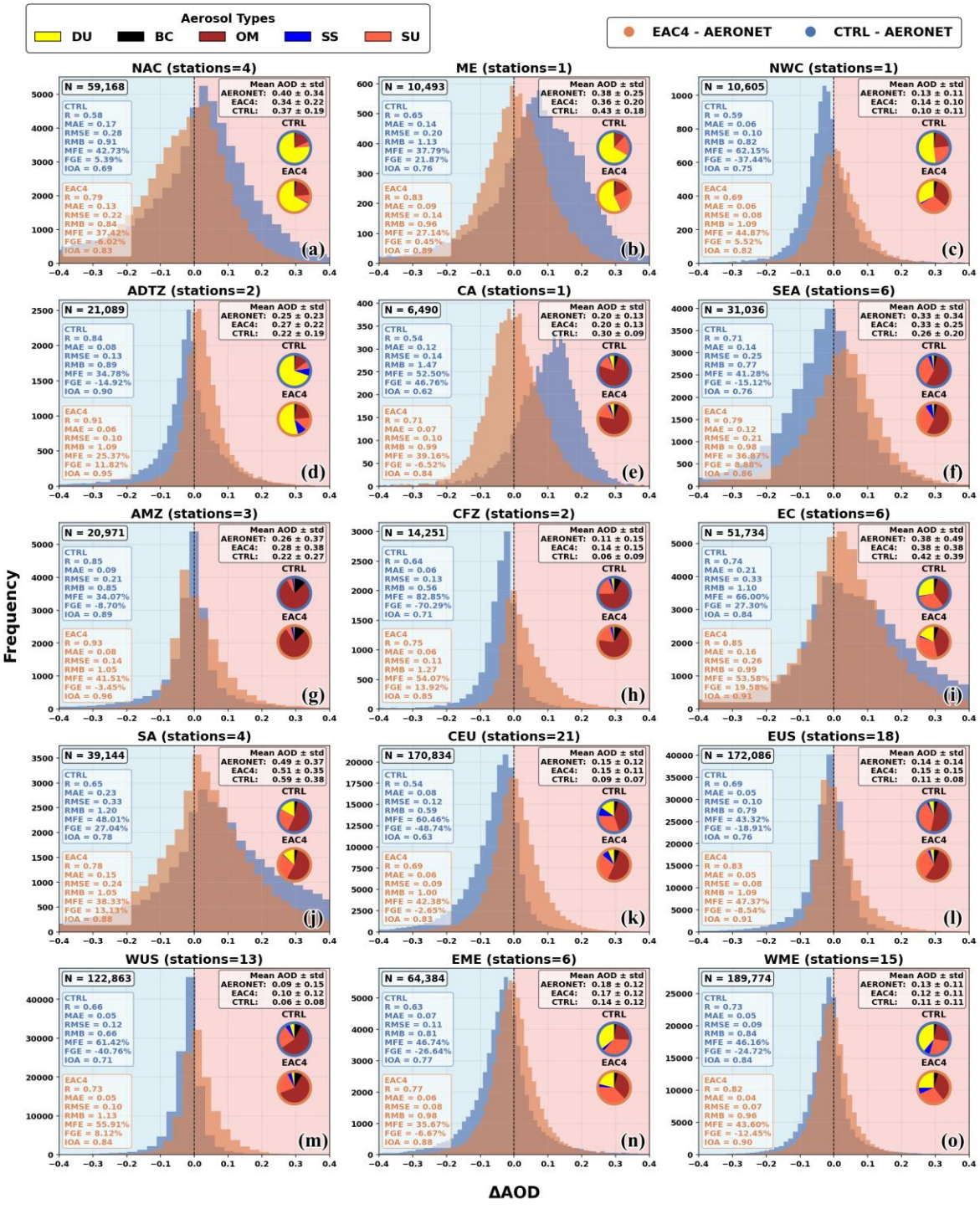

545 **Figure 6: Regional histograms of ΔAOD for CTRL (blue) and EAC4 (orange). The total number of collocated pairs (N) and the evaluation metrics (R, MAE, RMSE, RMB, %MFE, %FGE, IOA) are reported separately for each product. Pie charts indicate the relative contributions of the CAMS aerosol subtypes (DU, BC, OM, SS, SU) to the total AOD for CTRL and EAC4. The mean**

https://doi.org/10.5194/egusphere-2026-1107
Preprint. Discussion started: 6 March 2026

AERONET AOD, together with the mean ± standard deviation of CTRL and EAC4, are also shown. Background colours in both panels denote over- and underestimation.

3.2 Assessment of Aerosol Optical Depth Trends

3.2.1 Station-level assessment

Following the evaluation of CAMS AOD performance, this section examines the consistency of CAMS-derived AOD trends with those obtained from AERONET at the station level over the 2003–2024 study period. The spatial distribution of the AERONET stations, together with the corresponding AOD trends estimated from AERONET and from both CAMS configurations (EAC4 and CTRL), is shown in Fig. 7. The methodology used for trend estimation is described in detail in Section 2.3.2. Stations exhibiting trends that are statistically significant at the 95% confidence level are indicated by lime-outlined triangles.

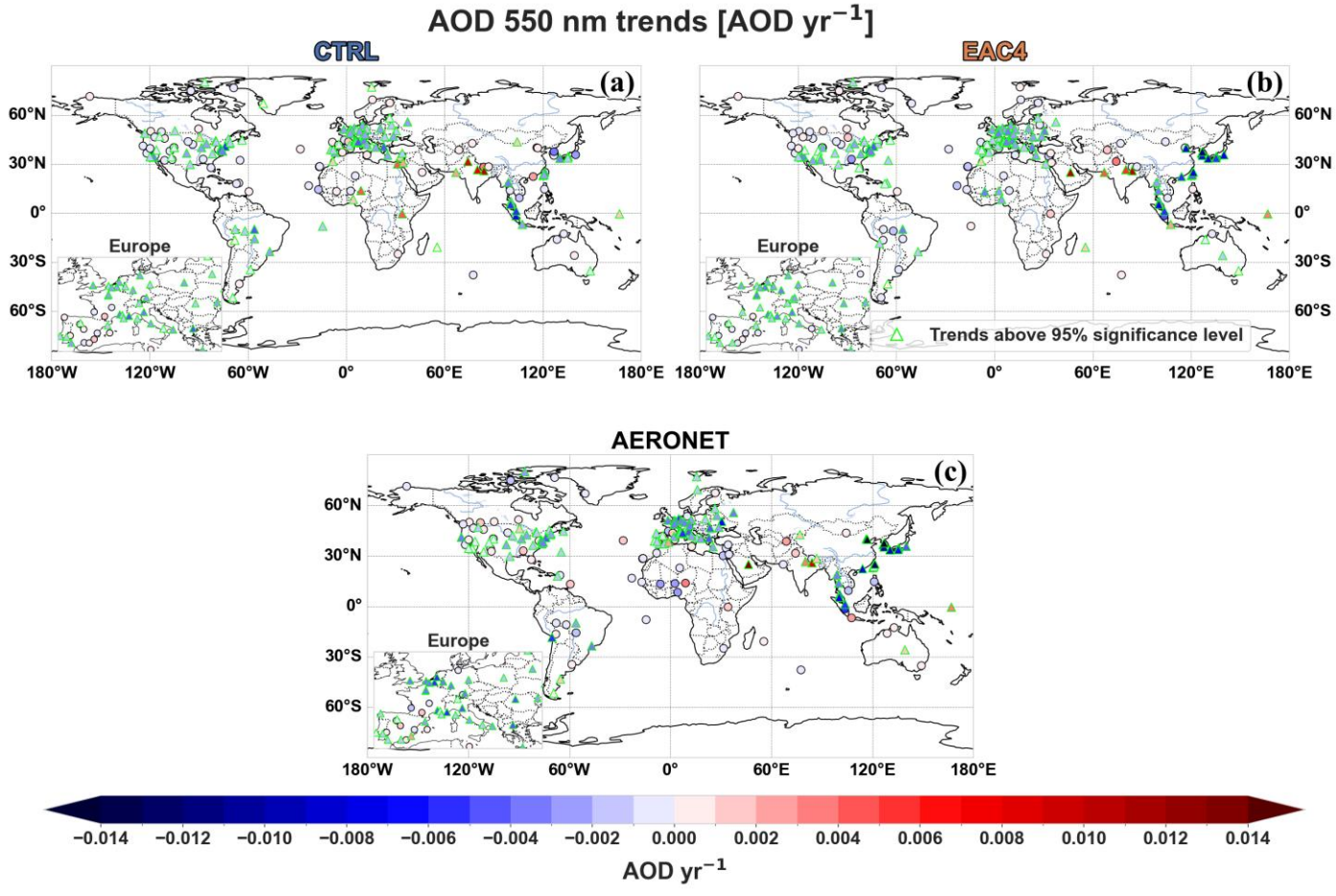

Figure 7: The AOD trends (AOD yr^{-1}) at 550 nm over the 178 AERONET stations based on (a) CTRL, (b) EAC4 and (c) AERONET. The lime-colored triangles indicate stations with trends above the 95% significance level.

https://doi.org/10.5194/egusphere-2026-1107
Preprint. Discussion started: 6 March 2026

Overall, both CAMS configurations reproduce the large-scale spatial patterns of AERONET-derived AOD trends, including predominantly negative trends over Europe, and North America (particularly the eastern United States), as well as positive trends over South Asia. However, EAC4 shows systematically better consistency with AERONET than CTRL, both in terms of trend sign and magnitude. The differences are most pronounced at stations exhibiting relatively strong positive or negative trends (e.g., in East Asia). In such cases, CTRL more frequently departs from the AERONET-derived trends, either by underestimating their magnitude or, in a few instances, by reproducing the opposite trend sign. By contrast, EAC4 rarely misrepresents the sign of the trend and generally shows smaller deviations from the AERONET estimates.

An alternative visualization of the AOD trend comparison is presented in Fig. 8, where the trends derived from EAC4 and CTRL are plotted directly against the corresponding AERONET trends for all 178 stations. In both panels, points lying along the 1:1 line indicate perfect agreement, while departures from this line reflect differences in trend magnitude and/or sign. The color scale denotes the total number of months contributing to each trend estimate, providing an indication of the temporal robustness of the trends. Stations with trends that are statistically significant at the 95% confidence level in both CAMS and AERONET are highlighted with lime-outlined triangles. The dashed envelopes (±0.005 and ±0.01 AOD yr^{-1}) illustrate increasing absolute deviation thresholds and provide a direct measure of how closely the simulated trends reproduce the observed trend magnitudes, independent of sign.

Figure 8 reveals a strong linear relationship between EAC4 and AERONET AOD trends, with a correlation coefficient of R = 0.86, a small mean bias error (MBE = 0.02 × 10^{-2}), and a relatively low RMSE (0.0019). In contrast, CTRL exhibits substantially weaker agreement with AERONET (R = 0.46, MBE = 0.09 × 10^{-2}, RMSE = 0.0033; Fig. 6.13a), highlighting the impact of the absence of satellite-based AOD assimilation in the control simulation. Consistently, EAC4 shows a noticeably reduced scatter around the 1:1 line compared to CTRL, indicating a more constrained and accurate reproduction of observed trend magnitudes.

To further quantify the agreement in trend magnitude, we evaluate the absolute deviation from the 1:1 line between CAMS and AERONET trends. For EAC4, 97.2% of stations exhibit $|\Delta trend| \leq 0.005$ AOD yr^{-1}, and all stations fall within ±0.01 AOD yr^{-1}. By comparison, CTRL shows lower fractions within the same thresholds, with 91.0% of stations within ±0.005 AOD yr^{-1} and 95.5% within ±0.01 AOD yr^{-1}. This confirms that assimilation improves the quantitative consistency of simulated AOD trends with AERONET observations. When restricting the analysis to stations with statistically significant trends in both CAMS and AERONET, a similar behaviour is observed: 95.3% of EAC4 stations fall within ±0.005 AOD yr^{-1} compared with 94.7% for CTRL, while 100.0% (EAC4) and 98.7% (CTRL) lie within ±0.01 AOD yr^{-1}. The persistence of these differences indicates that the improved agreement in EAC4 is not driven solely by weak or noisy trends.

The ability of EAC4 and CTRL to reproduce the sign of the AOD trends is assessed using the quadrant structure of the scatter plots in Fig. 8. Stations for which CAMS and AERONET exhibit the same trend sign fall within quadrants B1 (both negative) and A2 (both positive), whereas quadrants A1 and B2 indicate opposite-sign trends. Based on this classification, the overall sign agreement is 78.1% for EAC4 (121 stations in B1 and 18 in A2) and 80.9% for CTRL (114 in B1 and 30 in A2). Although CTRL shows a marginally higher sign agreement, sign consistency alone does not imply accurate trend representation. As

https://doi.org/10.5194/egusphere-2026-1107
Preprint. Discussion started: 6 March 2026

demonstrated by the absolute deviation analysis, EAC4 consistently exhibits smaller departures from the 1:1 line than CTRL across all tolerance thresholds, indicating a more faithful reproduction of trend magnitudes despite the slightly lower sign agreement.

Despite the overall strong performance of EAC4, a small cluster of five stations with statistically significant trends exhibits comparatively larger deviations from the 1:1 line. Four of these stations (Chen-Kung_Univ, EPA-NCU, Taipei_CWB, and Lulin) are located in Taiwan, while the fifth (XiangHe) is situated near Beijing in northeastern China. The larger discrepancies over Taiwan may be related to the island's complex topography and the relatively coarse spatial resolution of CAMS (≈80 km), which frequently spans land–ocean transitions and may not fully capture the local conditions sampled by AERONET. Retrieval uncertainties in the assimilated satellite observations over such heterogeneous surfaces may also contribute. For XiangHe—and to a lesser extent the nearby Beijing site—the discrepancies likely reflect a combination of uncertainties in emission trends, potential biases in assimilated observations over mixed urban–rural environments, and limitations in resolving station-scale variability.

Overall, the improved performance of EAC4 reflects the benefits of assimilation in constraining long-term aerosol variability in CAMS. Nevertheless, remaining discrepancies in both configurations highlight the combined influence of model uncertainties, potential biases in the assimilated AOD fields, emission assumptions, and the representativeness of individual AERONET stations.

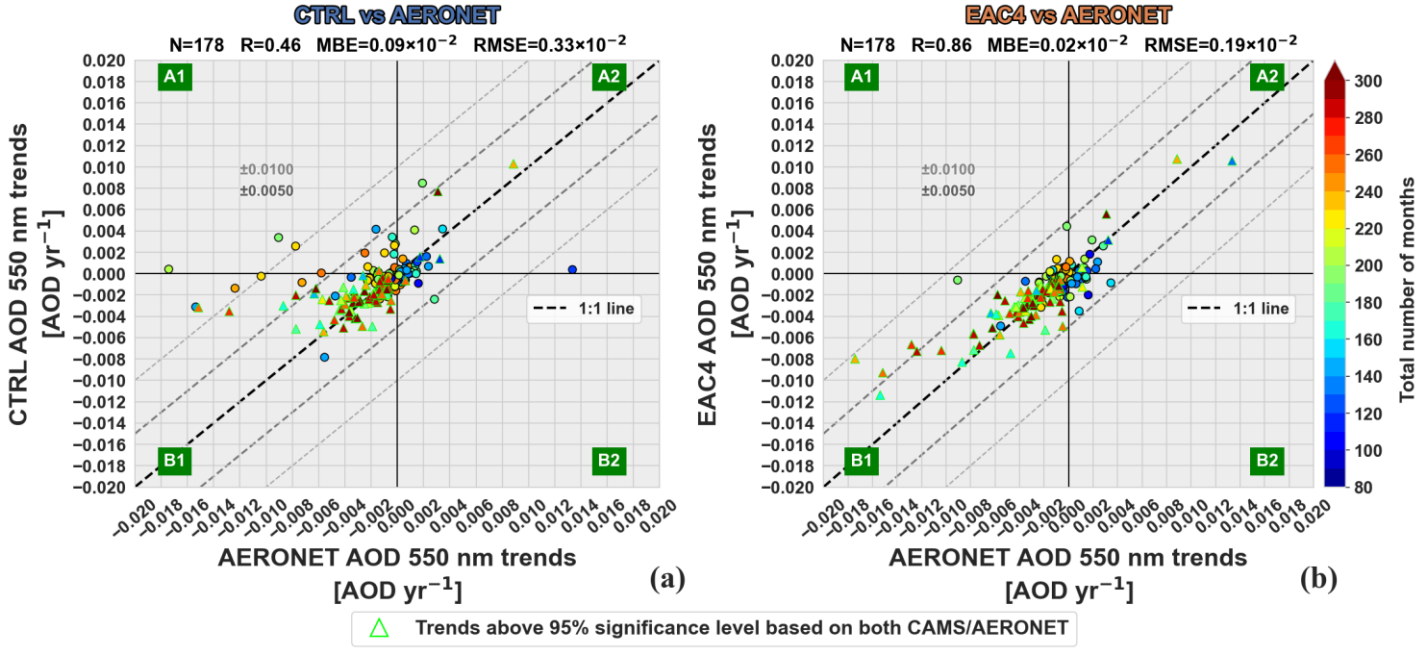

Figure 8: Scatter plots of AOD (550 nm) trends (AOD yr⁻¹) from (a) CTRL and (b) EAC4 versus AERONET over 178 stations. Marker color indicates the total number of months contributing to each trend estimate. Lime-outlined triangles denote stations where trends are statistically significant at the 95% confidence level in both CAMS configurations and AERONET. The dashed black line represents the 1:1 correspondence between modeled and observed trends, while the additional dashed envelopes indicate

https://doi.org/10.5194/egusphere-2026-1107
Preprint. Discussion started: 6 March 2026

increasing absolute deviation thresholds (±0.005, and ±0.01 AOD yr^{-1}) around the 1:1 line, illustrating the degree of quantitative agreement in trend magnitude.

3.2.2 Regional scale assessment

Following the station-level evaluation of AOD trends, a regional summary of AOD trends is presented in Table 2. For each region, the table reports the number of available AERONET stations and the total sample size, together with the mean AOD, its standard deviation, and the linear AOD trend (in $\times 10^{-3}$ yr^{-1}) derived from AERONET, EAC4, and CTRL. An additional GLOBAL row summarizes the same metrics for all available stations worldwide, comprising a total of 178 sites. Regions denoted by "–" correspond to ROIs excluded from the analysis due to the absence of AERONET stations (i.e., SFZ, SPO, and SAIO). The regional comparison reveals systematic differences between the assimilated EAC4 product and the free-running CTRL simulation when evaluated against AERONET. Overall, EAC4 shows closer agreement with AERONET-derived AOD trends in both sign and magnitude, highlighting the importance of satellite AOD assimilation for capturing long-term aerosol variability.

In anthropogenic pollution regions, including Central Europe (CEU), the eastern and western United States (EUS and WUS), and South Asia (SA), all three datasets generally agree on the sign of the trends but differ in magnitude. Over CEU and the United States, negative trends are consistently reproduced by both CAMS configurations, with only minor differences between EAC4 and CTRL, suggesting that gradual emission reductions are already reasonably represented in the free-running model and that assimilation mainly refines the trend magnitude. Over South Asia, all datasets indicate increasing AOD trends; however, CTRL exhibits a substantially stronger increase than both AERONET and EAC4, implying that, in the absence of assimilation, the control simulation may overemphasize emission growth or fail to capture regional mitigation effects. A notable exception among pollution-dominated regions is eastern China (EC), where AERONET indicates a strong negative trend that is partially captured by EAC4 but entirely missed by CTRL, which shows a near-neutral to weakly positive trend. This pronounced divergence underscores the inability of the free-running simulation to represent rapid, policy-driven emission reductions without observational constraints, demonstrating that assimilation is essential not only for adjusting trend magnitude but also for reproducing the correct trend direction.

In biomass-burning regions, including the Amazon (AMZ), Central Africa (CA), Southeast Asia (SEA), and the Canadian fires zone (CFZ), both CAMS configurations generally reproduce the sign of the AERONET-derived trends, which are weak to moderately positive or negative. Differences between EAC4 and CTRL are comparatively small, reflecting the strong interannual variability of fire emissions and the limited robustness of long-term trend estimates in these regions.

In dust-dominated regions, the comparison of AOD trends reveals some inconsistencies between AERONET and the CAMS configurations, although the trends are generally weak and should be interpreted with caution. Over North Africa (NAC), both AERONET and EAC4 indicate small positive trends, whereas CTRL shows a weak negative trend, indicating a fundamental inconsistency in the free-running simulation. Over northwestern China (NWC), AERONET and CTRL suggest a weak positive trend, while EAC4 shows a weak negative trend; however, the small trend magnitudes across all datasets limit the robustness

https://doi.org/10.5194/egusphere-2026-1107
Preprint. Discussion started: 6 March 2026

of this discrepancy. In the Middle East (ME), all datasets indicate positive AOD trends, but CTRL substantially underestimates the trend magnitude relative to both AERONET and EAC4.

In regions characterized by complex aerosol mixtures and seasonal dust intrusions, such as the eastern and western Mediterranean (EME and WME), all three datasets consistently show weak negative AOD trends close to zero, indicating good agreement in both sign and magnitude. This consistency suggests that, despite episodic dust events, the long-term AOD trend signal over the Mediterranean remains limited and is similarly represented in both assimilated and free-running simulations. In contrast, over the Atlantic dust transport zone (ADTZ), both CAMS configurations fail to reproduce the sign of the AERONET-derived trend, although the trend magnitudes remain close to zero.

Taken together, the regional AOD trend analysis demonstrates that satellite AOD assimilation substantially improves the representation of long-term aerosol trends in the CAMS reanalysis. The closer agreement between EAC4 and AERONET trends, compared with CTRL, confirms that observational constraints are essential for capturing regional aerosol trend signals, particularly in anthropogenic pollution regions. At the same time, many regions exhibit weak trend magnitudes that likely fall within combined observational and modeling uncertainties. Consequently, small trends should be interpreted with caution, as residual discrepancies may reflect limited trend robustness rather than physically meaningful changes.

Table 1: Summary of regional aerosol optical depth (AOD) statistics and AOD trends derived from collocated AERONET, CTRL, and EAC4 datasets over the Regions of Interest (ROIs) shown in Fig. 6.3. For each ROI, the table reports the number of available AERONET stations, the total number of collocated observations, the regional mean AOD, its standard deviation, and the linear AOD trends (in × 10^{-3} yr^{-1}) for each dataset. The GLOBAL row summarizes the same metrics for all available stations worldwide. ROIs labelled with "–" indicate regions excluded from the analysis due to the absence of collocated AERONET observations.

ROIs	AERONET stations	Sample size	AERONET			CTRL			EAC4		
			AOD	std	AOD trend (× 10^{-3} yr^{-1})	AOD	std	AOD trend (× 10^{-3} yr^{-1})	AOD	std	AOD trend (× 10^{-3} yr^{-1})
GLOBAL	178	1,657,564	0.18	0.23	**-1.72**	0.16	0.20	**-0.78**	0.19	0.20	**-1.48**
NAC	4	59,168	0.40	0.34	**-0.42**	0.37	0.19	**+0.94**	0.34	0.22	**-1.78**
ME	1	10,493	0.38	0.25	**+13.34**	0.43	0.18	**+0.38**	0.36	0.20	**+10.58**
NWC	1	10,605	0.13	0.11	**+1.45**	0.10	0.11	**+0.21**	0.14	0.10	**-0.52**
AMZ	3	20,971	0.26	0.37	**-1.46**	0.22	0.27	**-2.65**	0.28	0.38	**-2.19**
CA	1	6,490	0.20	0.13	**+1.32**	0.30	0.09	**+4.09**	0.20	0.13	**+1.37**
CFZ	2	14,251	0.11	0.15	**+0.13**	0.06	0.09	**+0.39**	0.14	0.15	**+0.41**
SEA	6	31,036	0.33	0.34	**-3.58**	0.26	0.20	**-4.11**	0.33	0.25	**-3.18**
SFZ	–	–	–	–	**–**	–	–	**–**	–	–	**–**
EC	6	51,734	0.38	0.49	**-7.85**	0.42	0.39	**+0.28**	0.38	0.38	**-4.32**
SA	4	39,144	0.49	0.37	**+3.23**	0.59	0.38	**+5.55**	0.51	0.35	**+3.92**

https://doi.org/10.5194/egusphere-2026-1107
Preprint. Discussion started: 6 March 2026

EUS	18	172,086	0.14	0.14	**-1.73**	0.11	0.08	**-2.15**	0.15	0.15	**-2.1**
WUS	13	122,863	0.09	0.15	**-0.5**	0.06	0.08	**-0.39**	0.10	0.12	**-0.71**
CEU	21	170,834	0.15	0.12	**-3.15**	0.09	0.07	**-2.03**	0.15	0.11	**-2.57**
ADTZ	2	21,089	0.25	0.23	**+0.27**	0.22	0.19	**-0.26**	0.27	0.22	**-0.47**
WME	15	189,774	0.13	0.11	**-0.35**	0.11	0.11	**-0.47**	0.12	0.11	**-0.79**
EME	6	64,384	0.18	0.12	**-1.96**	0.14	0.12	**-1.66**	0.17	0.12	**-1.51**
SPO	–	–	–	–	–	–	–	–	–	–	–
SAIO	–	–	–	–	–	–	–	–	–	–	–

3.3 Interannual Evolution of Regional Aerosol Optical Depth

Figure 9 presents the temporal evolution of regional EAC4 AOD, based on monthly mean values computed for the 18 ROIs over the 22-year period from 2003 to 2024. The respective regional time series are presented in the Supplement (Fig. S16). Over the dust dominated regions (i.e., the NAC, the ME, and the NWC), the monthly maximum AOD (up to 0.6) generally occurs between March and August (Figs. 9a–c). Over the ADTZ, maximum AOD values are observed from May to August, when the Saharan Air Layer (SAL) efficiently lifts dust to altitudes of 5–7 km, facilitating its long-range transport across the tropical Atlantic (Stuut et al., 2012; Adams et al., 2012; Muhs, 2013; Tsamalis et al., 2013). Due to cyclonic circulations over North Africa, the Mediterranean, and Europe, monthly AOD over the Mediterranean regions (EME and WME) (Gkikas et al., 2013; 2016) and CEU is also elevated during MAM and JJA, reflecting the influence of seasonal dust transport. Over the Mediterranean, monthly AOD shows clear seasonal and spatial variability, reflecting the influence of Saharan dust transport and prevailing circulation patterns (Varga et al., 2014; Gkikas et al., 2015). In March 2022, CAMS captured a strong dust outbreak over the WME, with monthly AOD values exceeding 0.3 due to intense advection from North Africa (Fig. 9p; WMO, 2023). In contrast, the May 2022 outbreak primarily affected the EME, where the monthly AOD was elevated, while WME remained less impacted (Fig. 9o; WMO 2023).

Across the regions dominated by biomass-burning activities (i.e., CA, AMZ, SEA, CFZ, and SFZ; Figs. 9e-i), higher monthly AODs are generally observed during JJA, with the exception of the AMZ and SEA, where the maximum values of monthly AODs are shifted to SON (Figs. 9h and 9f). From May to September 2023, CAMS captured the large-scale wildfires over the CFZ, with the resulting smoke plumes transported across the North Atlantic Ocean and reaching the Swiss Alps between late September and early October (Karanikolas et al., 2025; Masoom et al., 2025). The 2023 Canadian wildfires consumed nearly five times more biomass than the 2003–2020 reference average, underlining the growing severity of fire activity in boreal regions (Kaiser et al., 2024). This is consistent with the observed long-term increase in burnt area across Canada and Alaska (Calef et al., 2015; Hanes et al., 2019), a trend that is expected to be intensified in the future (Flannigan et al., 2005; Amiro et al., 2009; Park et al., 2023; Lund et al., 2023; Allen et al., 2024). Over SEA, a reduction in extreme fire events is observed—such as those recorded in 2006, 2015, and 2019, which were characterized by elevated monthly AOD values (Fig. 9f). In

https://doi.org/10.5194/egusphere-2026-1107
Preprint. Discussion started: 6 March 2026

particular, the intense wildfire episode of 2015 was driven by exceptional regional meteorological conditions, with extensive peatland fires in Indonesia linked to strong El Niño–induced drought (Flemming and Innes, 2024). The subsequent decline during the past five years likely reflects the effectiveness of stricter Indonesian government regulations aimed at limiting agricultural fires (Kaiser et al., 2024). Over SFZ, fire activity has shown a marked increase, particularly during the last decade compared with the previous one (Fig. 9g). This trend may be linked to the growing frequency and intensity of climate extremes, such as the prolonged heatwaves like the one that lead to the record-breaking wildfires of August 2021 (Flemming and Innes, 2024).

In relation to anthropogenic emissions, a significant decline in monthly AOD is observed over EC, followed by EUS and CEU, consistent with reductions driven by emission-control strategies (Ridley et al., 2018; Zheng et al., 2018; Quaas et al., 2022). By contrast, over SA and ME, monthly AOD exhibits an increasing trend, reflecting the rise in anthropogenic emissions, particularly over India and Iran (Satheesh et al., 2017). Over the WUS, the evolution of monthly AOD over the 22-year period appears more complex, as it is strongly influenced by extreme fire events (Fig. 9m). Notably, the severe wildfires of September 2020 and August 2021 stand out, with monthly AOD values reaching ~0.4. These events rank among the most significant fires recorded over WUS since 1980 (MacDonald et al., 2023). The large amounts of smoke from the September 2020 event were lofted into the free troposphere, and within only 3–4 days the plumes were transported from the WUS to central Europe (Peterson et al., 2018; Baars et al., 2021; Ceamanos et al., 2023), with a clear impact over EUS, where elevated AOD values were recorded during September 2020 (Fig. 9m).

Over the oceanic regions, namely the SPO and SAIO (Figs. 9q–r), AOD exhibits a generally constant pattern, with monthly values around 0.1–0.15. Notably, over the SPO, an increase in monthly AOD is observed in January 2020 reaching ~0.2. This peak in AOD during January–February 2020 coincides with the rapid transition from a strong La Niña (NDJ 2019–2020, ONI ≈ –1.2) to a weak El Niño (DJF/JFM 2020, ONI ≈ +0.5), based on the NOAA Oceanic Niño Index (ONI; https://www.cpc.ncep.noaa.gov/products/analysis_monitoring/ensostuff/ONI_v5.php, last access: 19 February 2026). The transition in the El Niño–Southern Oscillation (ENSO) likely induced anomalous wind patterns and locally enhanced wind speeds, which may have contributed to the observed AOD increase through enhanced sea spray production (Monahan et al., 1986; Smith et al., 1993). In addition, part of the elevated AOD values may be attributed to the long-range transport of smoke layers from the 2019–2020 Australian bushfires (Hirsch and Koren, 2021). Pyrocumulonimbus events associated with these fires lifted large amounts of smoke particles into the atmosphere, which were subsequently transported over the SPO, influencing regional AOD (Li et al., 2021). Similar to the SPO, AOD over the SAIO is not solely influenced by sea salt particles. Prevailing wind patterns facilitate the long-range transport of aerosols from adjacent dust sources (e.g., southern Africa and South America; Ginoux et al., 2012; Kok et al., 2023), seasonal large-scale fires, and emissions from international shipping, local industries, and biofuel and fossil fuel combustion in southern Africa (Dentener et al., 2006; Flemming et al., 2017; Kaiser et al., 2012; 2024), all of which contribute significantly to the observed AOD variability over this oceanic region.

https://doi.org/10.5194/egusphere-2026-1107
Preprint. Discussion started: 6 March 2026

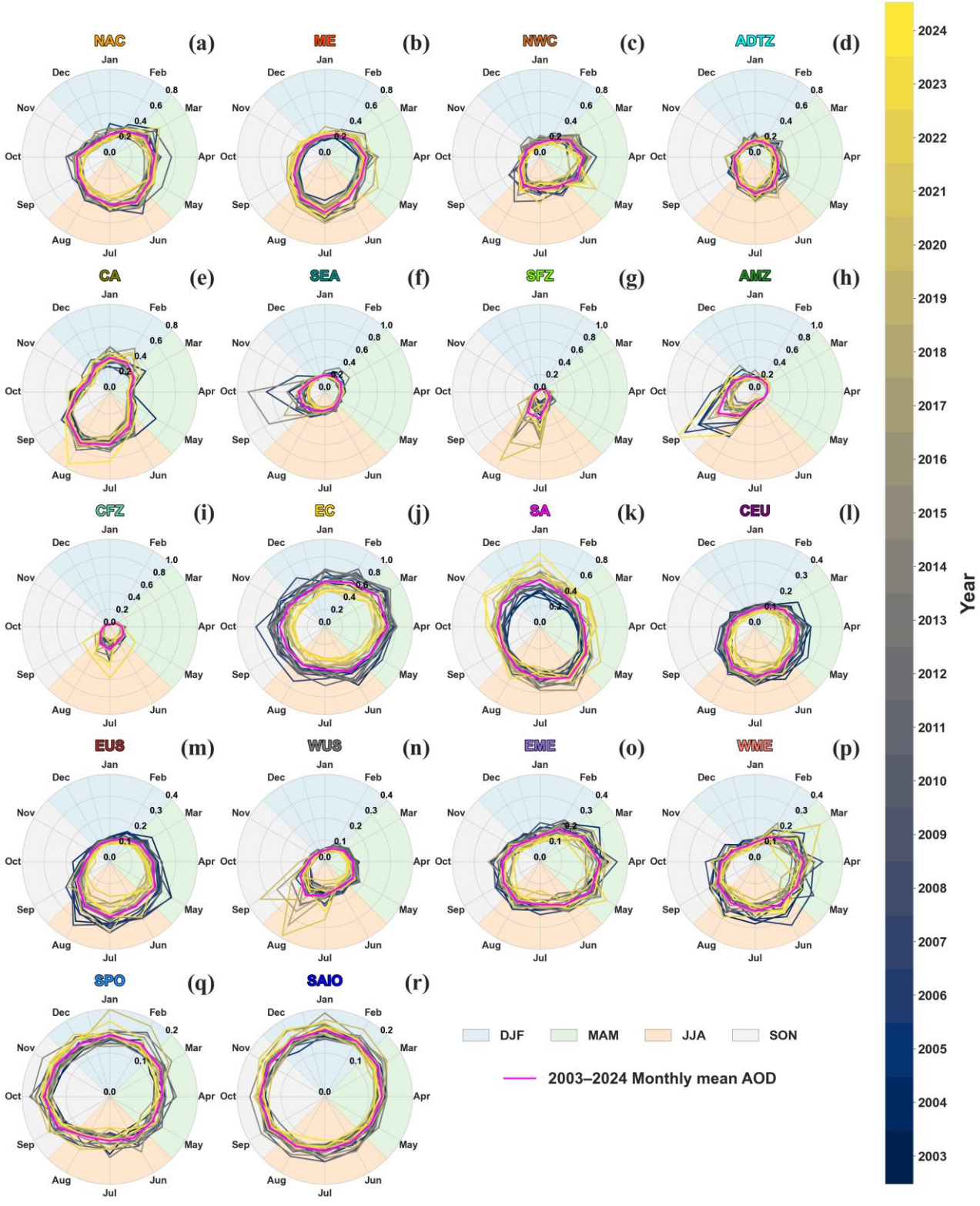

https://doi.org/10.5194/egusphere-2026-1107
Preprint. Discussion started: 6 March 2026

Figure 9: Temporal evolution of regional monthly averaged aerosol optical depth (AOD) for the 18 regions of interest (ROIs) (a-r). Each year is represented by a coloured ring with 12 directions, where each direction corresponds to a specific month. The distance from the centre of the ring indicates the regional monthly mean AOD value, and the colour of the ring represents the year. A magenta-coloured ring highlights the monthly mean AOD over the period 2003–2024. Seasonal variations are indicated by background colours: light blue for DJF, light green for MAM, light orange for JJA, and light grey for SON.

3.4 Global Distribution and Decadal Evolution of AOD Trends: Impact of Satellite Data Assimilation

In this section, annual AOD trends derived from the EAC4 and CTRL configurations are analysed at a spatial resolution of 0.75° × 0.75° for the full period 2003–2024, as well as for two sub-periods corresponding to the decades 2003–2013 and 2014–2024. This temporal subdivision is primarily used to illustrate the evolution of AOD trends over time, while potential non-linear behaviour, variability, and trend reversals in EAC4 are examined in greater detail in the following section using sliding-window trend analyses. The global spatial distributions of AOD trends are shown in Figs. 10–11, where grid cells with statistically significant trends ($p < 0.05$) are indicated by black outlines. A detailed description of the trend estimation methodology is provided in Section 2.1.2. Throughout this section, EAC4 is used as the primary dataset for the description and physical interpretation of the AOD trends, whereas the CTRL configuration is included for comparison only, in order to highlight the key differences between the assimilated and free-running model simulations on the diagnosed trends. Aerosol-speciated AOD trends are additionally presented in the Supplement for both EAC4 and CTRL (Figs. S17–S26).

Over the entire 22-year period (Fig. 10a), statistically significant negative trends in annual AOD are mainly observed over eastern China—reaching values as low as −0.026 AOD yr^{-1}—as well as over North Africa, central Europe, and the eastern United States. In contrast, widespread positive trends are evident across much of the Middle East and South Asia, with the strongest increases occurring over the Indian Peninsula, where trends reach up to +0.015 AOD yr^{-1}. The CTRL configuration shows notable differences, particularly over eastern China, where positive AOD trends are simulated in clear contradiction to both the EAC4 results and documented emission reduction policies (Zheng et al., 2018; Quaas et al., 2022). In addition, positive trends over the Middle East are weaker in magnitude and more spatially diffuse, extending westward toward the Sahel. Although positive trends persist over the sub-Sahel and central Africa—regions strongly influenced by biomass-burning activity—negative trends are simulated over the South Atlantic Ocean, where long-range transport of biomass-burning aerosols typically occurs (Zuidema et al., 2016). This contrasting behaviour is examined in more detail in the following paragraph.

When the analysis is separated into the two decades (Figs. 10b–c), pronounced regional shifts in both the magnitude and sign of AOD trends become apparent. During the first decade (2003–2013; Fig. 10b), statistically significant decreases in annual AOD are observed over the eastern United States, South America, Europe, the sub-Sahel region of North Africa, and Indonesia. In contrast, positive AOD trends dominate across large parts of the globe, including most oceanic regions, the Middle East, India, eastern China, and northern Siberia. The strongest positive trends during this period occur over eastern China and India, reaching up to +0.02 and +0.016 AOD yr^{-1}, respectively. During the second decade (2014–2024; Fig. 10c), increasing AOD trends persist over the Middle East and India, with particularly pronounced increases over the Middle East and more spatially confined but intensified trends over the northeastern Indo-Gangetic Plain. By contrast, the negative trends over the eastern United States and Europe weaken during the second decade relative to the first. The CTRL configuration exhibits a distinctly

https://doi.org/10.5194/egusphere-2026-1107
Preprint. Discussion started: 6 March 2026

different decadal evolution, with the largest discrepancies relative to EAC4 emerging during the 2014–2024 period (Figs. 11b–c). While the first decade shows broadly comparable large-scale patterns between the two configurations, the second decade is characterized in CTRL by widespread positive AOD trends over large parts of North Africa and substantially weaker negative trends over eastern China. This contrasting behaviour during the later period largely explains the differences in global AOD trends between EAC4 and CTRL, underscoring the dominant role of the second decade in driving the divergence between the assimilated and free-running CAMS simulations.

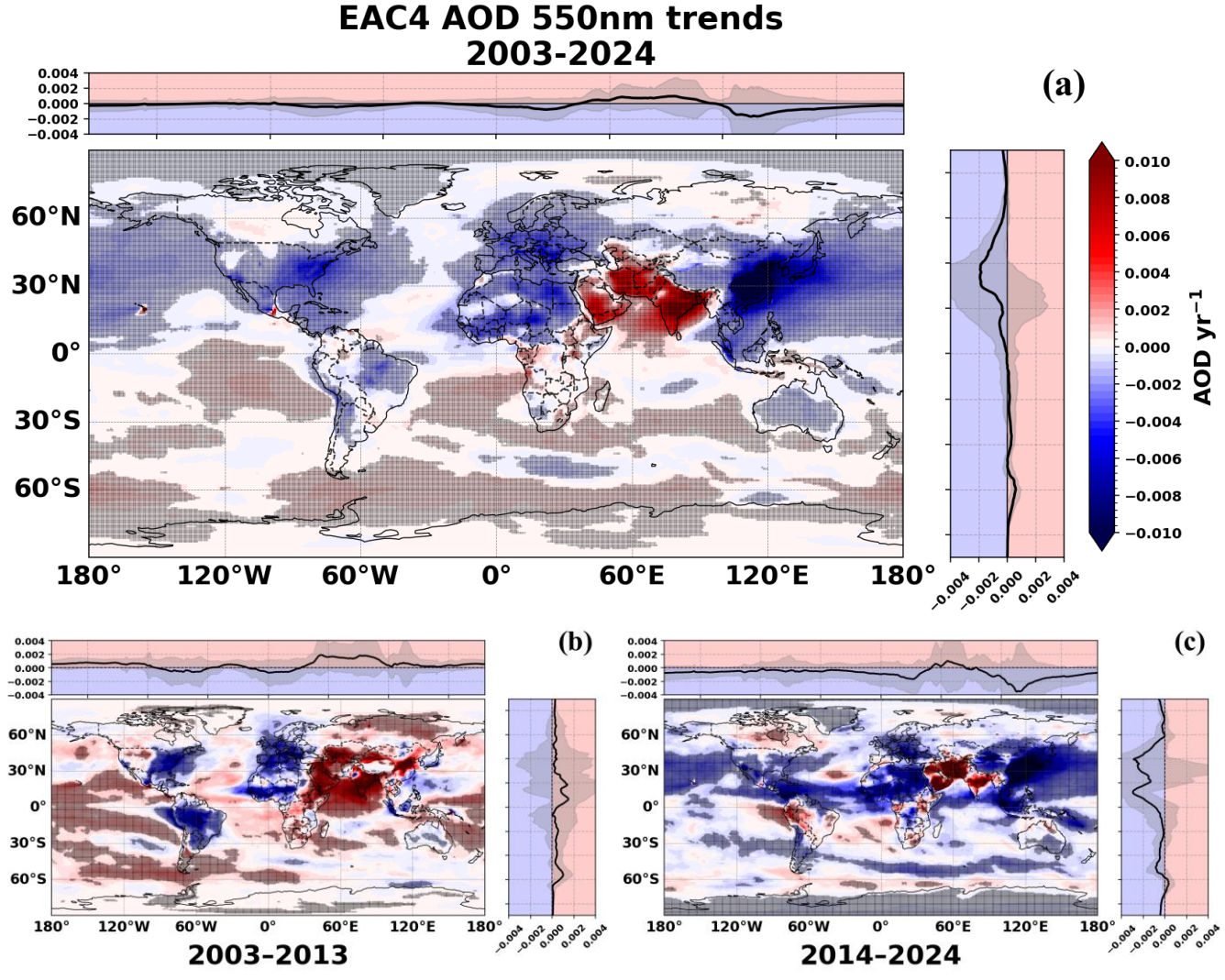

Figure 10: Geographical distribution of the annual EAC4 AOD trends at 550 nm, analysed at 0.75° × 0.75° grid resolution for (a) the full period 2003–2024, as well as for the two sub-periods, namely (b) 2003–2013 and (c) 2014–2024. Grid cells with statistically significant trends ($p < 0.05$) are highlighted with black outlines. The side panels show the corresponding zonal (right) and meridional (top) mean AOD trends.

https://doi.org/10.5194/egusphere-2026-1107
Preprint. Discussion started: 6 March 2026

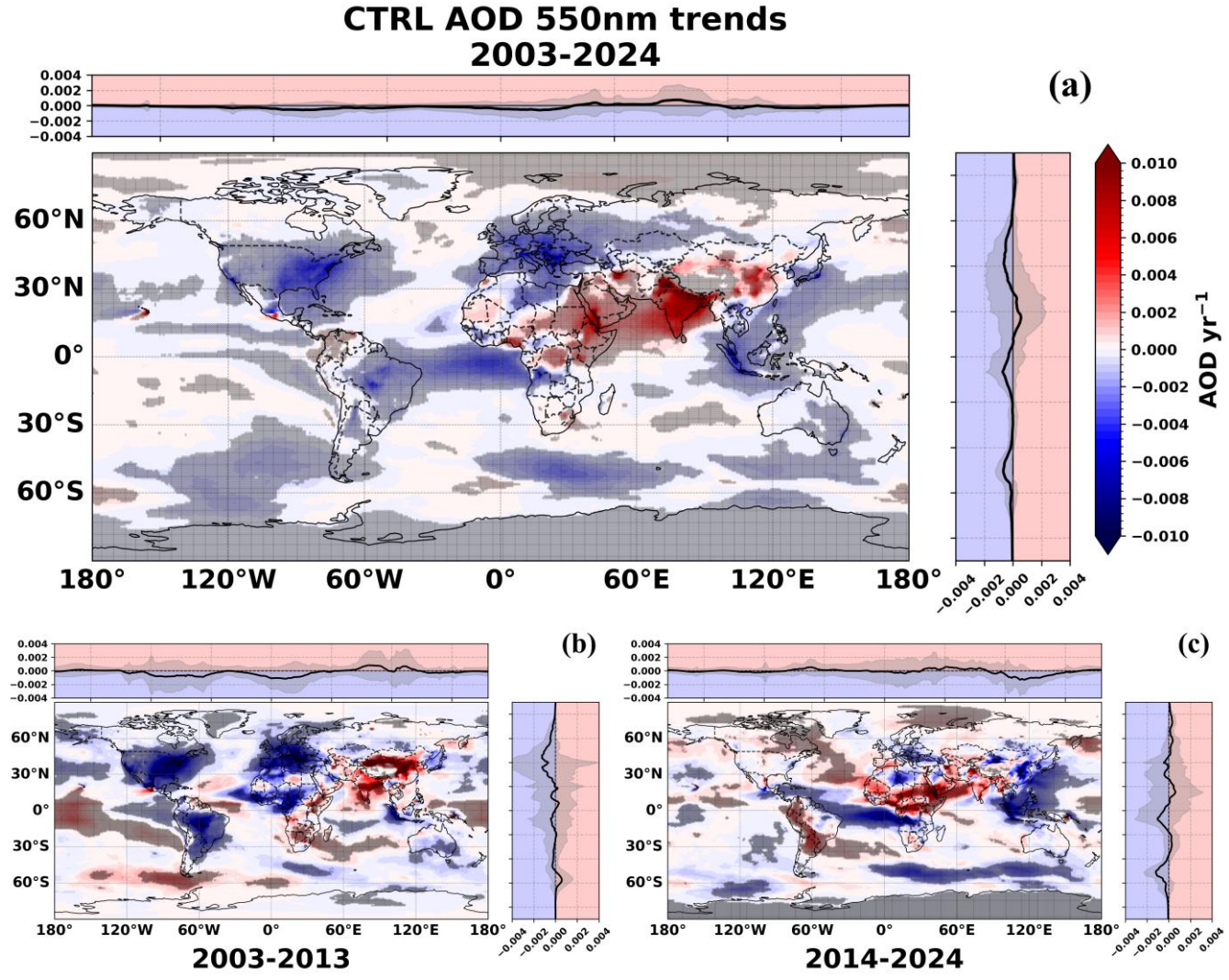

Figure 11: Geographical distribution of the annual CTRL AOD trends at 550 nm, analysed at 0.75° × 0.75° grid resolution for (a) the full period 2003–2024, as well as for the two sub-periods, namely (b) 2003–2013 and (c) 2014–2024. Grid cells with statistically significant trends ($p < 0.05$) are highlighted with black outlines. The side panels show the corresponding zonal (right) and meridional (top) mean AOD trends.

Over eastern China, the most pronounced reversal in AOD trends is observed, with trends shifting from strongly positive during 2003–2013 (up to +0.02 AOD yr^{-1}) to markedly negative during 2014–2024, reaching values as low as −0.035 AOD yr^{-1} (Figs. 10b–c). This transition is most likely attributable to the implementation of stringent emission control measures over the past decade (Zheng et al., 2018; Quaas et al., 2022). This interpretation is further supported by the strong negative trends in sulfate and organic matter optical depths (SUOD and OMOD), which dominate the contribution to the total AOD trends over the region. While AOD trends reached values of up to +0.025 AOD yr^{-1} during the early part of the record (approximately until 2008), they subsequently transitioned rapidly to negative values. These finer-scale temporal variations, derived from

https://doi.org/10.5194/egusphere-2026-1107
Preprint. Discussion started: 6 March 2026

overlapping 10-year moving windows, are examined in detail in the following section. In parallel with declining aerosol emissions over eastern China, AOD trends over the northern Pacific Ocean also reverse from positive during 2003–2013 to negative during 2014–2024. Given that the Taklamakan and Gobi Deserts are major dust source regions influencing eastern China (Chen et al., 2024), the concurrent negative trends in dust optical depth (DOD) suggest a secondary, yet non-negligible, contribution from reduced dust emissions to the observed AOD decline (Fig. S17). In the CTRL configuration, the negative trends in OMOD and SUOD are substantially weaker than those in EAC4 (Figs. S19–S23), highlighting the limitations of the MACCity emission inventory in capturing the effects of recent emission control policies. As discussed in Section 3.1, these discrepancies likely stem from the use of MACCity anthropogenic emissions (Granier et al., 2011), which do not account for recent emission reductions and therefore underestimate the impact of emission control measures.

Over Indonesia, negative AOD trends intensify markedly during the second decade, increasing in magnitude by nearly 80% and reaching values as low as −0.016 AOD yr^{-1} over Sumatra and Singapore (Fig. 10c). Aerosol-speciated trend analysis indicates that organic matter is the dominant contributor to these strong negative AOD trends (Figs. S21b–c). Moreover, the close agreement between CTRL and EAC4 over this region suggests that the observed decline in AOD is not primarily driven by changes in anthropogenic emissions. Given the known limitations of the MACCity inventory in representing recent anthropogenic emission changes, the pronounced AOD reduction is therefore more likely attributable to a decrease in biomass-burning activity.

Over the Middle East and South Asia, AOD trends remain persistently positive and intensify from 2003–2013 (approximately +0.015 AOD yr^{-1}) to 2014–2024 (up to +0.02 AOD yr^{-1}), consistent with reported increases in anthropogenic emissions in these regions (Satheesh et al., 2017). However, aerosol-speciated trend analyses indicate that this increase is not driven solely by organic matter and sulfate aerosols (Figs. S21b–c), but also by a substantial contribution from enhanced dust emissions, as reflected in positive DOD trends (Figs. S17b–c). A similarly complex behavior is evident in the CTRL configuration, although the positive trends are generally weaker across both decades (Fig. 11b–c).

Over North Africa, a pronounced increase in both the magnitude and spatial extent of statistically significant negative AOD trends is evident during the second decade. Specifically, during 2014–2024, negative AOD trends expand across most of North Africa, encompassing the Sahel and large portions of the Sahara Desert. The strongest declines, reaching up to −0.009 AOD yr^{-1}, occur over northeastern countries such as Libya, Egypt, and Sudan, which include major dust source regions such as the Libyan and Nubian deserts. Following this intensification of negative trends over North Africa, AOD trends over the open Atlantic Ocean, far from the North African coastal regions, shift from positive during 2003–2013 to negative during 2014–2024, whereas AOD trends in the near-coastal Atlantic remain persistently negative over both decades. This pattern suggests a reduction in long-range aerosol transport along the westerly circulation toward downwind regions, including South America and the Caribbean, where trends change from approximately +0.002 AOD yr^{-1} in the first decade to nearly −0.01 AOD yr^{-1} in the second decade. Aerosol-speciated analyses indicate a substantial contribution from dust to these changes, while reductions in biomass-burning activity over the Sahel and sub-Sahel regions are the primary driver of the negative AOD trends observed over the Atlantic Ocean (Figs. S17c, S19c, and S21c).

https://doi.org/10.5194/egusphere-2026-1107
Preprint. Discussion started: 6 March 2026

Notably, during the second decade (2014–2024), DOD trends over the northwestern Sahara are positive and statistically significant (Fig. S17c). However, this signal is largely masked in the total AOD trend maps by concurrent declines in other aerosol components (Fig. 10c). In contrast, the CTRL configuration exhibits markedly different behavior during the second decade (Fig. 11c). While differences relative to EAC4 are minimal during 2003–2013 (Figs. 10b and 11b), negative AOD trends in CTRL during 2014–2024 are largely confined to northern North Africa, mainly over parts of Libya and Algeria, whereas most other areas display predominantly positive trends. These positive trends closely follow the spatial distribution of organic matter optical depth (OMOD; Fig. S22c) and, to a lesser extent, DOD (Fig. S18c), indicating a stronger influence of biomass-burning-related aerosols in the absence of satellite-based AOD assimilation. This behaviour likely reflects an overestimation of biomass-burning emissions in the CTRL simulation, consistent with documented uncertainties in the GFAS fire emission product, although a concurrent overestimation of dust emissions cannot be excluded. In particular, persistence assumptions applied during periods of missing FRP observations can artificially prolong fire emissions, leading to enhanced organic matter loadings (Kaufman et al., 2003; Di Giuseppe et al., 2017). In addition, the positive CTRL DOD trends may partly reflect enhanced biomass-burning activity associated with land-use changes, such as deforestation and vegetation degradation, which increase surface erodibility and dust mobilization (Yu and Ginoux, 2022; Meng et al., 2025).

Over the Taklamakan Desert in northwestern China, AOD trends over the full 22-year period are negligible (Fig. 10a), owing to nearly compensating trends across the two decades, shifting from +0.012 AOD yr^{-1} during 2003–2013 to −0.02 AOD yr^{-1} during 2014–2024 (Figs. 10b–c). This behaviour highlights substantial temporal variability in regional dust emissions, further supported by the dominant contribution of DOD trends in this region (Figs. S17b–c). A comparable pattern is also evident in the CTRL configuration (Figs. 11b–c).

Over the Mediterranean basin, differences between the two decades are limited and primarily confined to the western Mediterranean, where AOD trends transition from weakly negative to weakly positive. This behaviour may reflect enhanced dust transport from western North African sources; however, the trends remain weak and statistically insignificant and therefore do not support robust conclusions. Nevertheless, the spatial pattern is consistent with the corresponding DOD trends (Fig. S17c). A similar, slightly stronger increase is observed in the CTRL configuration (Fig. 11c), likewise associated with positive DOD trends.

In the Southern Hemisphere, near-zero trends over the full period mask pronounced decadal shifts, particularly over South America and central Africa (Figs. 10b–c). During 2003–2013, negative AOD trends dominate over South America, encompassing the Amazon Basin and extending southward into Bolivia and Paraguay, with values reaching −0.01 AOD yr^{-1}. During 2014–2024, these trends reverse sign and become positive, reaching up to +0.005 AOD yr^{-1}, primarily driven by enhanced biomass-burning emissions, as indicated by organic matter optical depth trends (Figs. S21b–c). Over central Africa, the opposite behaviour is observed: weak positive AOD trends during 2003–2013 (up to +0.005 AOD yr^{-1}) transition to statistically significant negative trends during 2014–2024, reaching values as low as −0.06 AOD yr^{-1} and closely linked to OMOD trends (Figs. S21b–c). Overall, the CTRL configuration broadly agrees with EAC4 over South America and central

https://doi.org/10.5194/egusphere-2026-1107
Preprint. Discussion started: 6 March 2026

Africa, although it exhibits substantially stronger negative AOD trends over central Africa during the second decade, extending into the South Atlantic Ocean.

3.5 Regional Aerosol Optical Depth Trends

Building on the global AOD trend analysis over the full 22-year period and the two sub-periods (2003–2013 and 2014–2024) presented in the previous section, we apply sliding-window trend analyses to further assess the robustness and temporal evolution of the diagnosed EAC4 trends. Because both the sign and magnitude of trends can depend on the length of the analysis period, this approach allows a more precise identification of the timing, persistence, and potential reversals of trend signals. The analysis is performed for the 18 regions of interest (ROIs; Fig. 2) over the period 2003–2024, using varying start years and window lengths with a minimum duration of 10 years. The grouping of the different ROIs follows the dominant aerosol-type contributions illustrated by the pie charts in Fig. 2, which indicate the prevailing fractional contribution of CAMS aerosol components to total AOD in each ROI. The results are presented by region type, beginning with dust-dominated regions (e.g., North Africa, the Middle East, and northwestern China), followed by biomass-burning regions (e.g., Central Africa, Southeast Asia, and the Amazon), anthropogenic pollution regions (e.g., eastern China and South Asia), remote Southern Hemisphere oceanic regions (South Pacific Ocean and South Atlantic–Indian Ocean), and finally regions characterized by a heterogeneous aerosol burden and pronounced seasonal dust outbreaks, such as the Mediterranean Basin. To support the interpretation of the total AOD trends and to identify the dominant drivers associated with individual aerosol components, aerosol-speciated sliding-window trends for dust (DU), sea salt (SS), organic matter (OM), black carbon (BC), and sulfate (SU) aerosols are additionally provided in the Supplement (Figs. S27–S51).

3.5.1 Dust

As illustrated in Fig. 12, the sliding-window trend analysis over North Africa (NAC) reveals significant declines in AOD for windows starting in the early 2000s. For windows beginning around 2007–2009, the trends weaken and show mostly insignificant reversals; however, from approximately 2010 onward, negative trends re-emerge and become statistically significant. During the most recent decade, these declines further intensify and become more consistent, indicating a sustained reduction in AOD, with trend magnitudes reaching down to $-0.006\ yr^{-1}$.

The aerosol-speciated trend analysis provides further insight into the drivers of this behaviour. DOD trends over NAC (Fig. S27) are generally negative but weak and statistically insignificant during the earlier sub-periods, becoming stronger and statistically significant during the most recent decade. This behaviour is consistent with satellite-based DOD trend analyses by Logothetis et al. (2021), who used the MIDAS dataset (Gkikas et al., 2021) to derive global and regional dust trends and reported a widespread decline in dust activity over NAC, accompanied by a reduction in Saharan dust export after 2010. Similar decreasing AOD trends over NAC were reported by Che et al. (2019), who analysed long-term aerosol variability

https://doi.org/10.5194/egusphere-2026-1107
Preprint. Discussion started: 6 March 2026

using the MERRA-2 reanalysis (1980–2016) and attributed a substantial fraction of the inter-decadal AOD variability in this dust-dominated region to meteorological changes, particularly reduced surface wind speeds.

In parallel, organic matter optical depth (OMOD) exhibits strong and statistically significant negative trends across nearly all sub-periods, with a tendency toward stronger declines after approximately 2009, indicating a substantial contribution of organic aerosols to the total AOD decrease (Fig. S29). Sulfate aerosols play a more minor role, with significant negative trends emerging only after about 2013 (Fig. S31). It should be noted that NAC includes large parts of the Sahel and sub-Sahel, regions characterized by pronounced biomass-burning activity. The observed decline in organic matter—and to a lesser extent sulfate—is therefore consistent with reported reductions in biomass-burning emissions in recent years. This interpretation is further supported by Wei et al. (2020), who identified a long-term decline in fire activity across northern sub-Saharan Africa during 2001–2016, primarily driven by cropland expansion and increased drought frequency leading to reduced fuel availability. Additionally, Zhang et al. (2025), using long-term AERONET observations of aerosol optical and microphysical properties, reported predominantly negative trends in both AOD and absorbing aerosol optical depth (AAOD) over North Africa, accompanied by weak or insignificant changes in the Ångström exponent. This behaviour indicates an overall reduction in aerosol loading—driven by both coarse-mode dust and fine-mode aerosols—rather than a fundamental shift in aerosol type, in agreement with the declining dust and organic matter contributions identified here.

Over the Middle East (ME), the trend evolution exhibits an essentially opposite behaviour. Windows starting in the early 2000s are characterized by significant positive trends, followed by a brief transition to significant negative trends for start years around 2007–2008. Subsequently, positive trends re-emerge and intensify, with the strongest increases occurring during the most recent decade, reaching up to +0.007 yr^{-1}. This behaviour is consistent with satellite-based analyses by Klingmüller et al. (2016), who used MODIS AOD retrievals to identify pronounced positive AOD trends over large parts of the ME during the early 2000s, primarily driven by enhanced dust emissions associated with declining soil moisture and increasing aridity. They further showed that this dust-driven increase weakened after about 2012, consistent with the partial reversals and subsequent re-intensification captured by the sliding-window trends presented here. Similarly, Che et al. (2019) reported strong positive AOD trends during the early 2000s that turned negative when assessed using decadal-scale windows starting around 2005. Notaro et al. (2015) further demonstrated that changes in dust activity over the Arabian Peninsula can be closely associated with large-scale climate variability, particularly El Niño–Southern Oscillation (ENSO) and the Pacific Decadal Oscillation (PDO), underscoring the influence of ocean–atmosphere teleconnections on regional dust variability. The aerosol-speciated trend analysis indicates that organic matter, sulfate, and dust all contribute to the observed AOD trends over the ME, highlighting the complex aerosol regime of the region, which is influenced by dust emissions, biomass burning, and anthropogenic pollution (Figs. S27, S29, and S31).

Finally, over northwestern China (NWC), AOD trends are significantly positive until the mid-2000s, reaching values of up to +0.004 yr^{-1}, before reversing to statistically significant negative trends from approximately 2009 onward. The strongest declines occur during the most recent decade, with magnitudes reaching −0.005 yr^{-1}. Unlike NAC and ME, the overall 22-year trend over NWC remains weak and statistically insignificant, reflecting a pronounced but largely compensating transition from

https://doi.org/10.5194/egusphere-2026-1107
Preprint. Discussion started: 6 March 2026

increasing to decreasing tendencies over the study period. Aerosol-speciated trend analysis indicates that dust is the dominant driver of AOD variability over NWC, with DOD largely controlling both the positive trends during the early period and the subsequent decline (Fig. S27). This behaviour is in very good agreement with Che et al. (2019), who reported a clear reversal of AOD trends over NWC, from increasing tendencies in earlier decades to declining trends in more recent periods, primarily driven by meteorological changes affecting dust emissions, especially surface wind speed. Importantly, their long-term analysis further indicates that AOD trends over NWC exhibit multiple sign reversals when examined using sliding windows starting as early as the 1980s, with several transitions evident up to windows beginning in the mid-2000s.

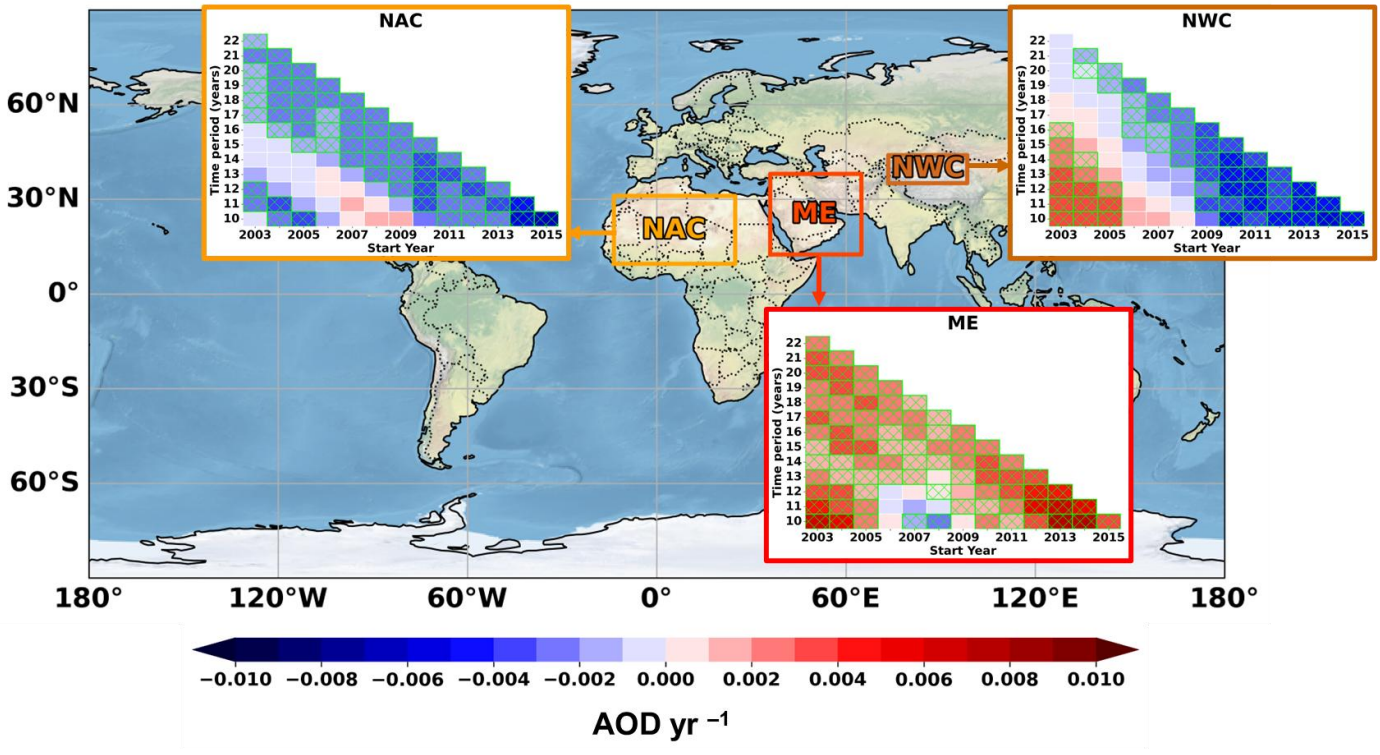

Figure 12: Regional aerosol optical depth (AOD) trends at different time intervals for the dust-dominated regions, with at least 10-year time series (the acronym full names of the regions are presented in Fig. 2). The x-axis shows the starting year, while the y-axis represents the length of the time series used to calculate the trend. The colors of the rectangles indicate the magnitude of the trend (units: AOD yr^{-1}), and the lime-hatched rectangles denote trends that are above the 95% significance level.

3.5.2 Biomass-Burning

Across regions dominated by biomass-burning activity, the most pronounced AOD trends—both in magnitude and statistical significance—are observed over the Amazon Basin (AMZ), Central Africa (CA), and Southeast Asia (SEA) (Fig. 13).

Over the AMZ, the sliding-window analysis reveals marked declines in AOD for windows starting in the early 2000s, with statistically significant negative trends between 2003 and 2006 reaching values as low as −0.005 yr^{-1}. Around 2007–2008,

https://doi.org/10.5194/egusphere-2026-1107
Preprint. Discussion started: 6 March 2026

these trends weaken and lose statistical significance, indicating a transitional phase. From approximately 2009 onward, the trends reverse sign, with moderate positive tendencies emerging during the most recent decade and reaching up to +0.002 yr^{-1}. This evolution is consistent with Che et al. (2019), who reported strong inter-decadal variability over the AMZ, including negative AOD trends during the early 2000s. Similarly, Gui et al. (2021), using MISR type-segregated AOD data (2001–2018), showed that variability and trends over the AMZ are primarily controlled by small, spherical aerosols associated with biomass-burning activity, with predominantly negative trends for windows starting in the early to mid-2000s and reversals toward positive tendencies around 2009–2010.

In contrast, Central Africa exhibits a clear reversal from significant positive AOD trends for windows starting in the early 2000s to statistically significant negative trends for windows beginning around 2010. Trend magnitudes transition from values as high as +0.005 yr^{-1} to declines of up to −0.004 yr^{-1}, indicating a shift toward decreasing AOD levels during the most recent decade. A similar reversal was reported by Che et al. (2019), who identified positive AOD trends over CA for early-2000s windows analysed at decadal scales. Consistently, Gui et al. (2021) found a comparable transition, with decreasing AOD in later years primarily linked to a reduced contribution from non-spherical aerosols, indicative of declining biomass-burning activity. This interpretation is further supported by recent estimates showing that, while African fire-related carbon emissions accounted for nearly half of the global total during the 2000s, their relative contribution has since declined to approximately 40% (Kaiser et al., 2024).

Over Southeast Asia, the sliding-window trends indicate a more persistent decline in AOD. Most windows exhibit negative trends, many of which are statistically significant, particularly for start years in the early 2000s and again from around 2010 onward. Trend magnitudes reach down to −0.004 yr^{-1}, whereas positive trends are rare, weak, and statistically insignificant. Overall, SEA emerges as a region characterized by a sustained downward trajectory in AOD, in contrast to the more variable or reversing patterns observed in other biomass-burning regions. A similar evolution was reported by Che et al. (2019), who identified negative AOD trends during the early 2000s followed by a brief transition toward positive tendencies in the mid-2000s. Furthermore, Gui et al. (2021) documented pronounced negative AOD trends over SEA for windows starting from around 2011 onward, although their trends are generally weaker and less statistically significant than those identified here. The reported reduction in fire intensity over SEA is likely linked to stricter governmental regulations aimed at limiting agricultural burning practices (Kaiser et al., 2024).

For the Canadian fires zone (CFZ), sliding-window trends are more heterogeneous. Windows starting in the early 2000s exhibit weak and mostly statistically insignificant positive trends. Between approximately 2006 and 2010, several negative trends emerge, some of which are relatively strong and statistically significant, particularly for window lengths of 10–15 years. In subsequent years, weak positive tendencies reappear but remain inconsistent. As a result, no robust long-term AOD trend can be identified for this region, indicating relatively stable aerosol conditions over the full 22-year period.

In contrast, the Siberian fires zone (SFZ) shows a more coherent temporal evolution. Windows starting in the early 2000s are characterized by strong and statistically significant positive AOD trends that persist until the mid-2000s. From around 2008 onward, the trend direction reverses, with negative trends becoming increasingly dominant. During the most recent decade,

https://doi.org/10.5194/egusphere-2026-1107
Preprint. Discussion started: 6 March 2026

this decline is further reinforced, with several statistically significant negative trends evident, particularly for window lengths of 13–17 years.

Finally, aerosol-speciated analyses indicate that, across biomass-burning-dominated regions, the observed increases or decreases in total AOD are primarily driven by organic matter aerosols, while other aerosol components contribute more weakly but remain statistically significant in many cases (Figs. S32–E36).

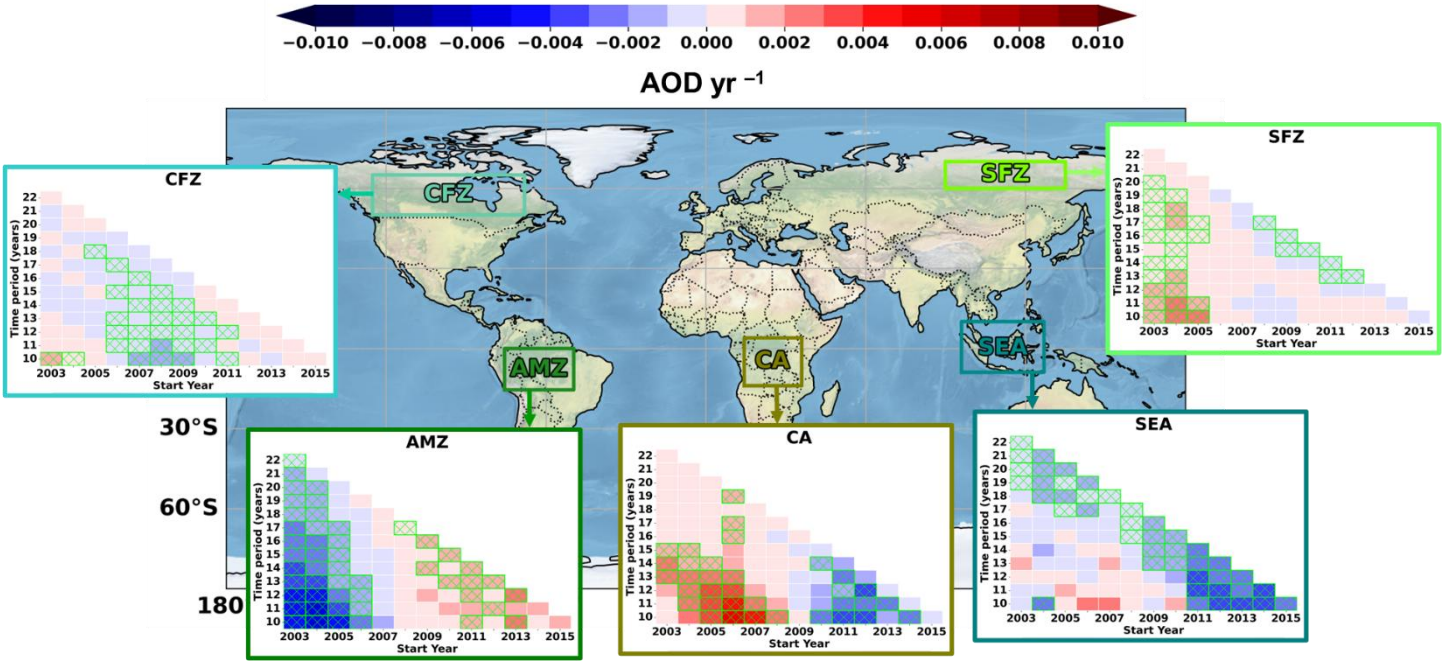

Figure 13: Regional aerosol optical depth (AOD) trends at different time intervals for the biomass-burning-dominated regions, with at least 10-year time series (the acronym full names of the regions are presented in Fig. 2). The x-axis shows the starting year, while the y-axis represents the length of the time series used to calculate the trend. The colors of the rectangles indicate the magnitude of the trend (units: AOD yr^{-1}), and the lime-hatched rectangles denote trends that are above the 95% significance level.

3.5.3 Urban/Pollution

As shown in Fig. 14, the sliding-window trend analysis over regions primarily influenced by anthropogenic emissions reveals a marked contrast between South Asia (SA) and the other regions considered. SA stands out as the only region exhibiting a persistent increase in AOD, with nearly all windows showing positive and statistically significant trends, particularly for windows starting in the early 2000s. This upward tendency persists over most of the study period, with trend magnitudes reaching up to +0.009 yr^{-1}, indicating an overall increase in aerosol loading over SA during the past two decades. This behaviour is consistent with reported persistent anthropogenic emissions across the region (Satheesh et al., 2017).

In contrast, all other anthropogenic-pollution regions exhibit predominantly declining AOD trends, albeit with varying magnitudes and degrees of persistence. Over eastern China (EC), one of the most robust signals is observed, characterized by

https://doi.org/10.5194/egusphere-2026-1107
Preprint. Discussion started: 6 March 2026

a sustained and statistically significant decrease in AOD across nearly all windows, particularly for start years after 2005, with trend magnitudes reaching down to −0.019 yr^{-1}. Over the eastern United States (EUS), negative and statistically significant trends dominate most windows, indicating a steady decline in AOD over the study period, with values reaching −0.004 yr^{-1}. The western United States (WUS) displays a more heterogeneous evolution, with weak and mostly insignificant trends during the early 2000s followed by more consistent, stronger declines in later years. Over central Europe (CEU), the sliding-window analysis reveals a widespread decrease in AOD, with statistically significant negative trends across nearly all windows and magnitudes reaching −0.003 yr^{-1}.

Overall, anthropogenic-pollution regions present a coherent picture of declining AOD over the past two decades, with South Asia representing a clear exception characterized by a persistent and statistically significant increase in aerosol loading. The widespread decreases observed over EC, EUS, WUS, and CEU are consistent with large-scale reductions in anthropogenic emissions documented in previous studies (Ridley et al., 2017; Zheng et al., 2018; Quaas et al., 2022). The increasing AOD over SA is primarily driven by enhanced fine-mode aerosols, with organic matter and sulfate contributing most strongly to the positive trends (Figs. S39 and S41). This is consistent with aerosol-type analyses by Zhang et al. (2025), who reported increasing contributions from weakly absorbing and scattering fine-mode aerosols over South Asia. Conversely, Zhang et al. (2025) also documented pronounced decreases in fine-mode anthropogenic aerosols over eastern China, the United States, and Europe, affecting both organic matter and sulfate components, in agreement with the widespread negative AOD trends identified here (Figs. S39 and S41).

Comparable AOD trends across these regions have been reported in other independent studies, including Che et al. (2019) and Gui et al. (2021), providing additional confidence in the robustness of the trends identified here. For eastern China, it is also noteworthy that dust optical depth (DOD) trends contribute significantly to the total AOD decrease (Fig. S37). Reduced dust emissions over the broader Taklamakan and Gobi Desert regions—major dust source areas influencing China (Chen et al., 2024)—have therefore played a non-negligible role in shaping the observed negative AOD trends.

https://doi.org/10.5194/egusphere-2026-1107
Preprint. Discussion started: 6 March 2026

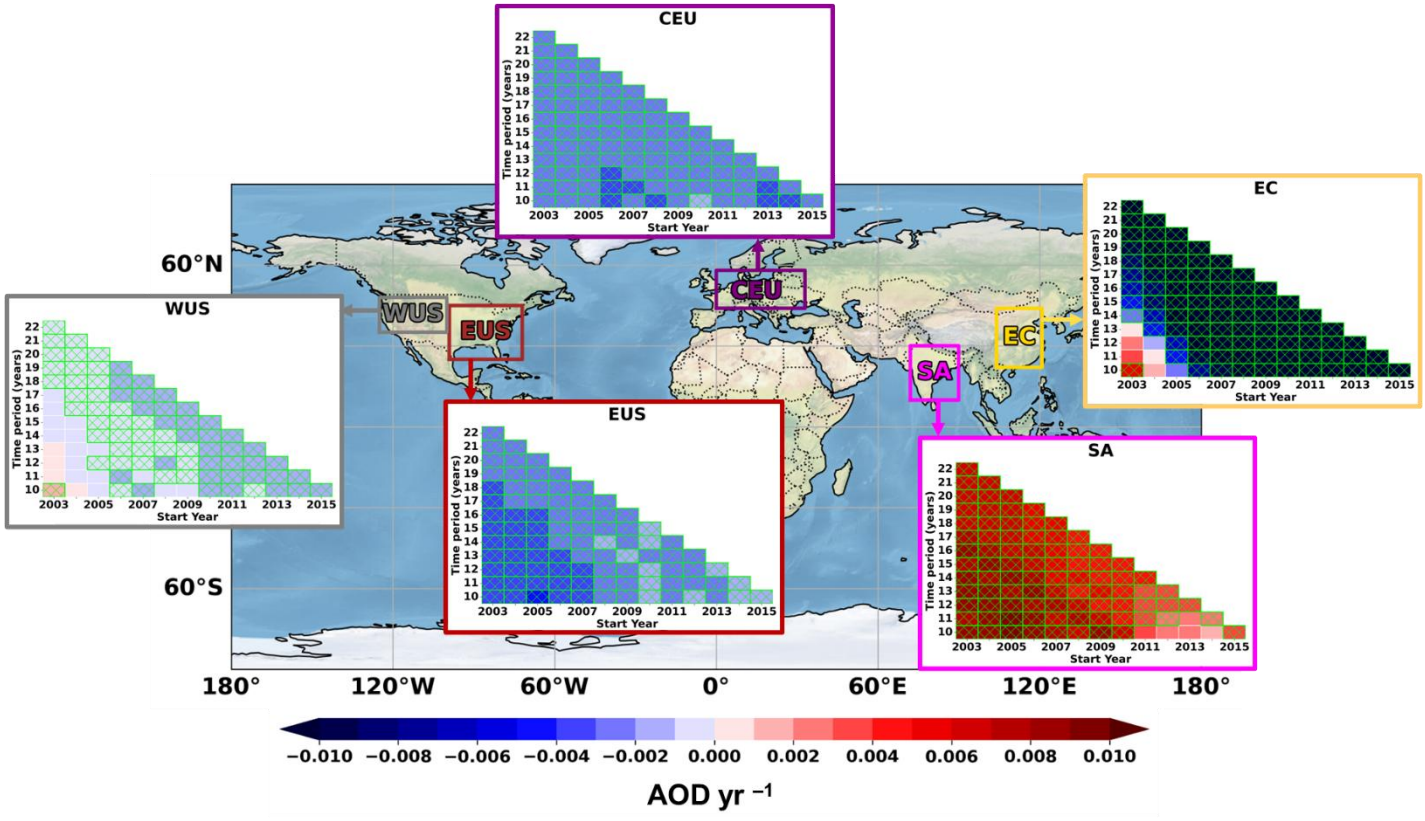

Figure 14: Regional aerosol optical depth (AOD) trends at different time intervals for the urban/pollution-dominated regions, with at least 10-year time series (the acronym full names of the regions are presented in Fig. 2). The x-axis shows the starting year, while the y-axis represents the length of the time series used to calculate the trend. The colors of the rectangles indicate the magnitude of the trend (units: AOD yr^{-1}), and the lime-hatched rectangles denote trends that are above the 95% significance level.

3.5.4 Sea Salt

Over the remote Southern Oceanic regions—the South Pacific Ocean (SPO) and the South Atlantic–Indian Ocean (SAIO)—where AOD is largely controlled by natural sea salt emissions (Fig. S43), the sliding-window analysis reveals more modest and less systematic trends than those observed over continental regions (Fig. 15).

Over the SPO, the strongest and most statistically significant trends occur during the early 2000s, with several windows starting between 2003 and 2005 exhibiting significant positive tendencies. Around 2010, a distinct negative and statistically significant trend emerges; however, this signal is short-lived and does not persist in subsequent windows. Outside these periods, AOD trends weaken and become less coherent, with no sustained long-term tendency evident.

Over the SAIO region, the temporal evolution is more complex. During the early 2000s, most windows show positive AOD trends, several of which are statistically significant. Around 2007–2008, these positive signals weaken and become less consistent. In the most recent part of the record, corresponding to window start years around 2014–2015, the trend direction reverses, with negative tendencies becoming apparent.

https://doi.org/10.5194/egusphere-2026-1107
Preprint. Discussion started: 6 March 2026

Overall, the remote oceanic regions are characterized by episodic rather than persistent AOD changes, with the early 2000s standing out as a period of relatively stronger and more significant trends. Further investigation is required to assess the role of meteorological drivers—such as changes in wind speed, circulation patterns, and sea surface temperature—which directly influence sea-salt aerosol emissions (Monahan et al., 1986; Smith et al., 1993). In addition, the potential contribution of long-range aerosol transport by the westerlies from adjacent continental regions should be considered, including episodic intrusions of dust or smoke originating from South America, southern Africa, and Australia. For example, dust outbreaks from the Patagonian Desert and the Lake Eyre Basin—two major contributors to Southern Hemisphere dust emissions (Prospero et al., 2002; Gkikas et al., 2021)—as well as seasonal biomass-burning activity, may intermittently enhance aerosol loadings over these remote oceanic basins.

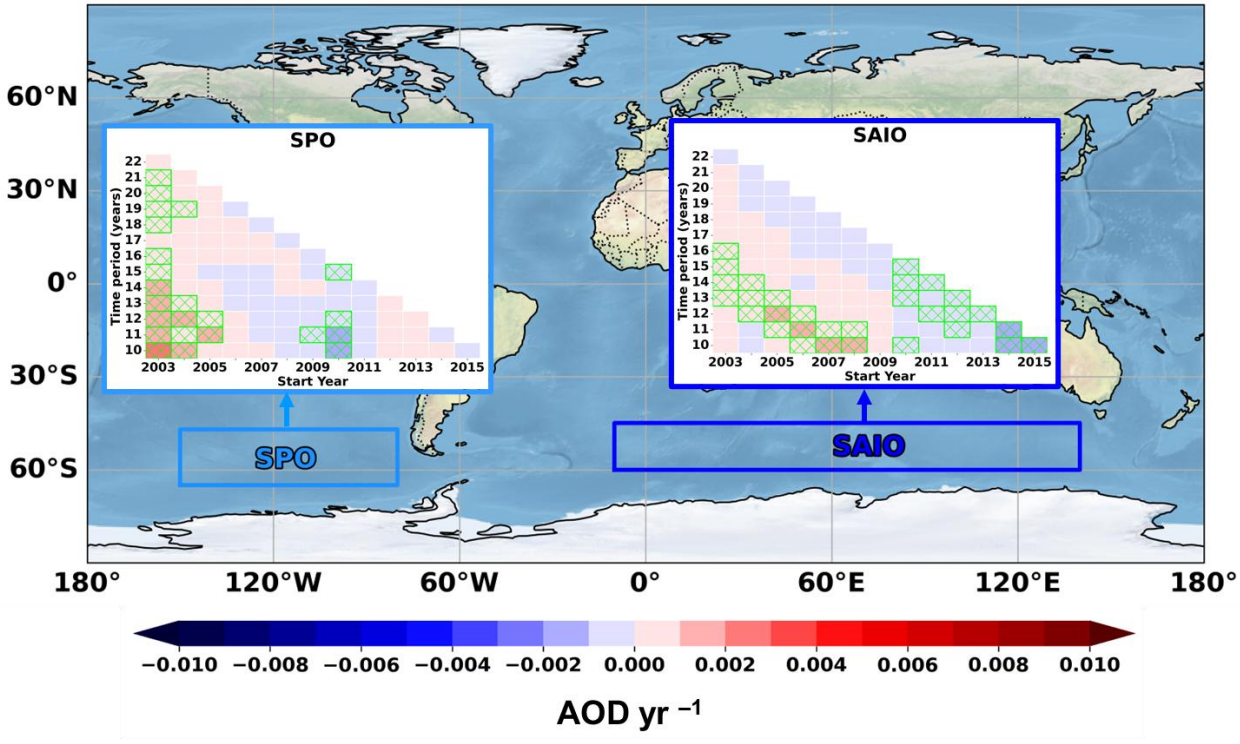

Figure 15: Regional aerosol optical depth (AOD) trends at different time intervals for the salt-dominated regions, with at least 10-year time series (the acronym full names of the regions are presented in Fig. 2). The x-axis shows the starting year, while the y-axis represents the length of the time series used to calculate the trend. The colors of the rectangles indicate the magnitude of the trend (units: AOD yr^{-1}), and the lime-hatched rectangles denote trends that are above the 95% significance level.

3.5.5 Tropical Atlantic Ocean and Mediterranean

Over regions characterized by complex aerosol regimes influenced by seasonal dust outbreaks, the sliding-window analysis reveals diverse and often intricate AOD trend behaviour (Fig. 16).

https://doi.org/10.5194/egusphere-2026-1107
Preprint. Discussion started: 6 March 2026

Over the western Mediterranean (WME), the analysis indicates predominantly negative AOD trends, with magnitudes reaching down to −0.004 yr^{-1}. Strong and statistically significant declines dominate windows starting in the early 2000s, particularly for window lengths of 10–15 years. For windows beginning after approximately 2009, the trends weaken and, in some cases, lose statistical significance, indicating a less persistent downward signal. From about 2012 onward, a partial reversal emerges, with several windows exhibiting weak positive tendencies that are largely statistically insignificant. Aerosol-speciated trend analysis shows that dust optical depth (DOD) exhibits statistically significant positive trends during this later period, suggesting that changes in dust contributions play a dominant role in shaping the observed partial reversal of AOD trends (Fig. S47).

In contrast, the eastern Mediterranean (EME) displays a more robust and coherent evolution. Negative and statistically significant AOD trends dominate nearly all windows throughout the record, with magnitudes reaching −0.003 yr^{-1} and little evidence of weakening over time. Although both regions are part of the broader Mediterranean basin, their temporal evolution differs markedly: the WME exhibits pronounced variability, including periods of negative trends followed by recent positive tendencies, consistent with reported increases in winter dust outbreaks in the WME during recent years (Cuevas-Agulló et al., 2024), whereas the EME shows a more persistent and spatially coherent downward trend.

Overall, these results are broadly consistent with the findings of Logothetis et al. (2021), who reported Mediterranean basin DOD trends ranging approximately from −0.006 to +0.002 yr^{-1}. A comparable DOD trend pattern over the 2003–2024 period is also identified in the present study when considering the global DOD trend maps discussed in the previous section (Fig. S17). However, because Logothetis et al. (2021) treated the Mediterranean as a single region in their sliding-window analysis, the differing behaviour of the western and eastern sub-basins could not be resolved. The present regional subdivision therefore provides additional insight into the heterogeneous nature of AOD trends across the Mediterranean basin.

Over the Atlantic dust transport zone (ADTZ), AOD trends are more heterogeneous. Windows starting in the early 2000s show weak or statistically insignificant tendencies, whereas windows beginning after about 2009 reveal more pronounced and often statistically significant declines, with magnitudes reaching down to −0.003 yr^{-1}. Notably, while AOD decreases over the ADTZ during the most recent decade, parts of the WME exhibit the opposite tendency. This contrasting behaviour likely reflects regional differences in dust optical depth trends, as positive dust trends over the northwestern Sahara during the second decade may enhance the transport of dust layers toward the western Mediterranean (Fig. S17c), highlighting the complexity of aerosol sources and transport pathways influencing the region.

Aerosol-speciated trend analysis provides further insight into the drivers of these changes. Dust optical depth trends over the ADTZ show weak positive tendencies for windows starting around 2008 (Fig. E42), with alternating statistically significant and non-significant behaviour, indicating a limited and temporally variable dust contribution. In contrast, the decline in total AOD over the ADTZ (Fig. 16) is primarily driven by reductions in organic matter and sulfate aerosols, consistent with decreased biomass-burning activity over the Sahel and sub-Sahel regions. This reduction likely limits the westward transport of smoke aerosols over the Atlantic, thereby lowering the aerosol burden over the ADTZ. Overall, while mineral dust remains a major aerosol component in the region, changes in biomass-burning-related aerosols play a key role in shaping recent AOD trends.

https://doi.org/10.5194/egusphere-2026-1107
Preprint. Discussion started: 6 March 2026

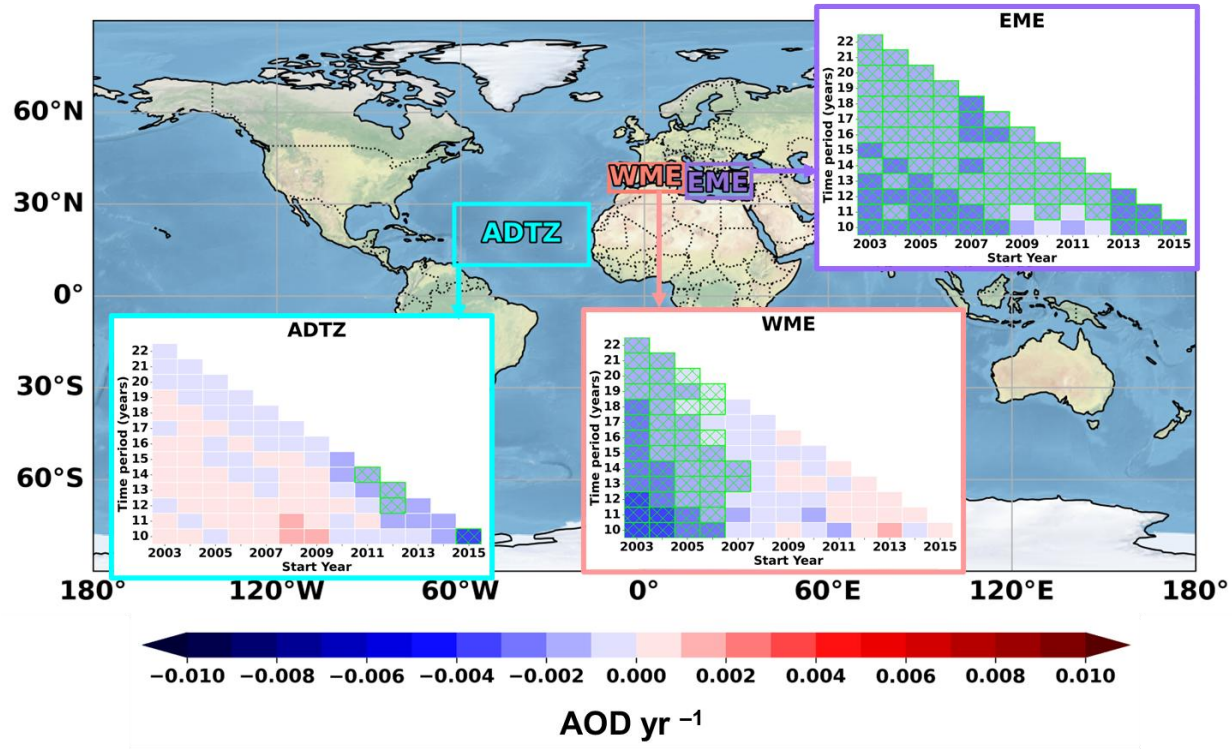

Figure 16: Regional aerosol optical depth (AOD) trends at different time intervals for the regions characterized by a complex aerosol regime and seasonal dust outbreaks, with at least 10-year time series (the acronym full names of the regions are presented in Fig. 2). The x-axis shows the starting year, while the y-axis represents the length of the time series used to calculate the trend. The colors of the rectangles indicate the magnitude of the trend (units: AOD yr^{-1}), and the lime-hatched rectangles denote trends that are above the 95% significance level.

4 Summary and conclusions

This study provides a comprehensive assessment of global and regional aerosol optical depth (AOD) variability and trends at 550 nm using the fourth-generation ECMWF Atmospheric Composition Reanalysis (EAC4) and the corresponding free-running simulation (CTRL) over the 2003–2024 period. Ground-based AERONET observations were used as an independent reference to evaluate the ability of EAC4 to reproduce both AOD magnitudes and long-term trends prior, and to quantify the added value of assimilation by directly comparing EAC4 with CTRL**,** to analysing the global and regional evolution of aerosols. A rigorous station-selection strategy was applied to ensure robust trend estimation, resulting in a high-quality dataset of 178 AERONET stations with extensive and continuous records.

The evaluation against AERONET confirms that CAMS reproduces global AOD variability with high skill, with EAC4 clearly outperforming CTRL. EAC4 achieves a correlation of R = 0.84, RMSE = 0.12, MAE = 0.07, and IOA = 0.90 (based on more than 1.6 million collocated pairs), while CTRL exhibits systematically weaker agreement and a pronounced underestimation of AOD, demonstrating the substantial benefit of satellite assimilation. Regional performance depends on the dominant aerosol type: variability is well captured in anthropogenic and biomass-burning regions, while larger uncertainties persist in dust-

https://doi.org/10.5194/egusphere-2026-1107
Preprint. Discussion started: 6 March 2026

dominated areas, particularly over North Africa, where coarse dust remains underrepresented in both configurations. CAMS successfully reproduces long-range Saharan dust transport across the Atlantic, while discrepancies in biomass-burning regions—most notably the Canadian fire zone—likely reflect uncertainties in fire emission estimates. CAMS-derived long-term AOD trends show strong agreement with AERONET observations at stations with statistically significant trends, with EAC4 again outperforming CTRL in both trend magnitude and consistency. For EAC4, a correlation of R = 0.89, low bias (MBE = 0.052×10^{-2}), and small error (RMSE = 0.0021) are obtained. The magnitude of observed trends is accurately reproduced at most sites, with 88 out of 92 stations exhibiting absolute trend differences smaller than 0.005 AOD yr^{-1}. EAC4 correctly captures the sign of the AOD trend at 96.7% of stations, successfully reproducing all negative trends, while CTRL shows weaker agreement and more frequent underestimation of trend magnitudes. Remaining discrepancies in EAC4 are confined to a small cluster of stations in Taiwan and northeastern China, where complex terrain, coarse model resolution, satellite retrieval uncertainties, and emission-related limitations likely contribute to the misrepresentation of trend magnitude or sign.

Trend analyses over the full 22-year period and over two sub-periods (2003–2013 and 2014–2024) reveal clear decadal shifts in both the magnitude and sign of AOD trends, with aerosol-speciated trends clarifying the mechanisms behind these transitions. The most pronounced change occurs over eastern China, where trends reverse from positive during the first decade to strongly negative during the second, reflecting a sharp decline in sulfate and organic matter AOD following the implementation of stringent air-quality policies. Negative trends also intensify over North Africa and the Sahel, coinciding with reductions in dust optical depth and a weakening of trans-Atlantic dust transport. In contrast, South Asia and the Middle East maintain persistent positive trends across both decades, driven by continued increases in sulfate and organic aerosols, and by enhanced dust loading over the Middle East. Biomass-burning regions exhibit more complex behaviour: Central Africa shifts from increasing to decreasing trends, associated with declining organic aerosol contributions in the later period, while the Amazon shows the opposite transition, linked to increasing organic aerosol from intensified fire activity. Sliding-window trend analyses further demonstrate that the inferred sign and magnitude of AOD trends strongly depend on the selected time window, especially in regions dominated by natural aerosol sources. While anthropogenic regions exhibit robust and temporally consistent declines driven by fine-mode aerosol reductions (primarily sulfate), dust- and biomass-burning-dominated regions show pronounced variability in both total and speciated AOD, reflecting the combined influence of meteorological factors, and surface changes. A summary and highlight figure of the regional aerosol-speciated trend analysis for the full 2003–2024 period and the two decadal sub-periods (2003–2013 and 2014–2024), is presented in Fig. 17.

https://doi.org/10.5194/egusphere-2026-1107
Preprint. Discussion started: 6 March 2026

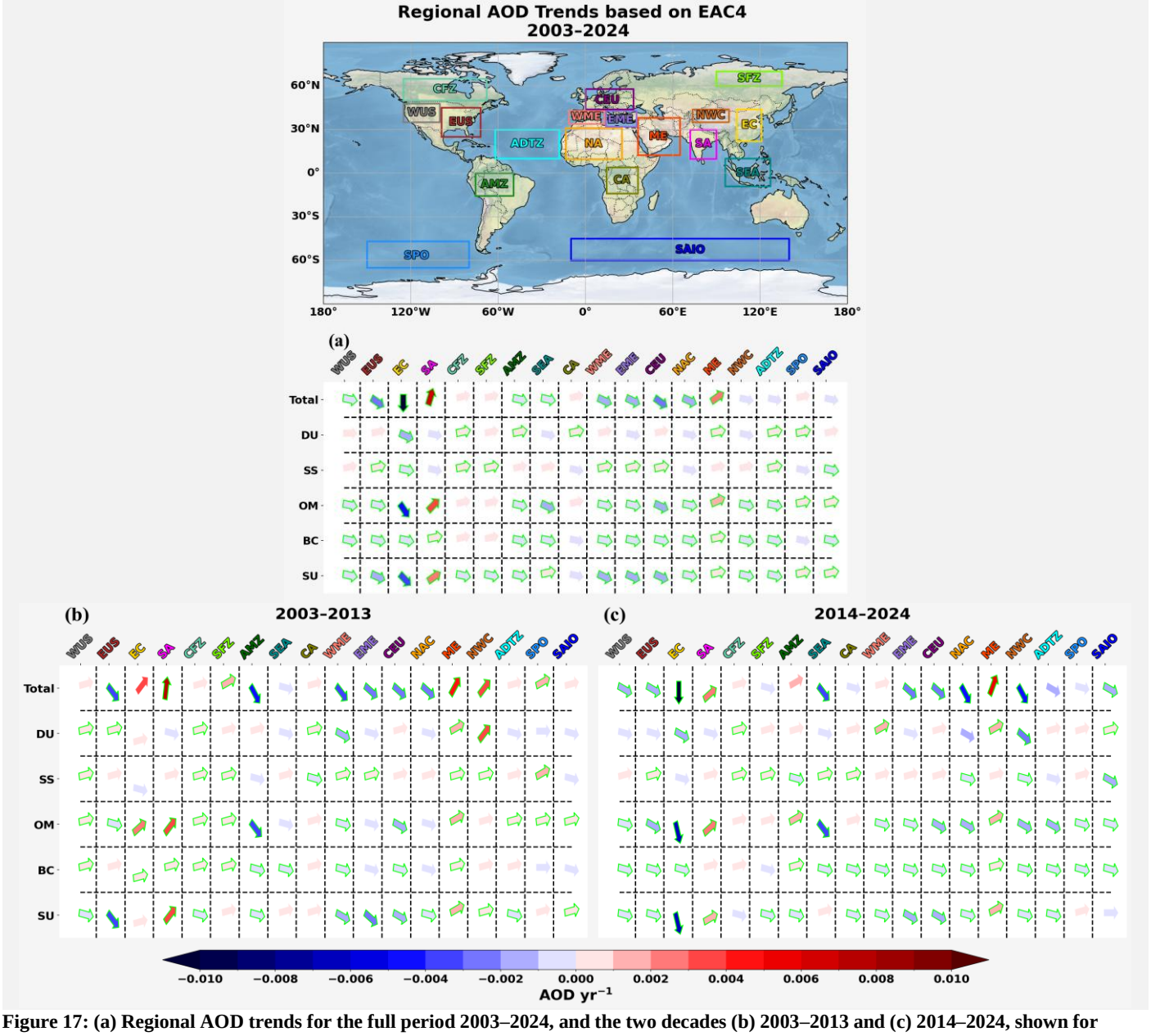

Figure 17: (a) Regional AOD trends for the full period 2003–2024, and the two decades (b) 2003–2013 and (c) 2014–2024, shown for total AOD and individual aerosol components (DU: dust, SS: sea salt, OM: organic matter, BC: black carbon, and SU: sulfate). Arrows indicate the direction and relative magnitude of the linear trend, with arrow orientation and colors proportional to the trend sign and magnitude (AOD yr⁻¹). Lime-outlined arrows denote statistically significant trends ($p < 0.05$). Top panel displays the geographical locations of the 18 ROIs (as presented in Fig. 2).

Over regions where the most pronounced shifts in AOD trend patterns are observed, further work is required to better quantify the role of different driving mechanisms in modulating the diagnosed aerosol trends. While this study has explicitly and in an introductory way examined the contributions of individual aerosol components to the total AOD signal, it remains essential to

https://doi.org/10.5194/egusphere-2026-1107
Preprint. Discussion started: 6 March 2026

assess how changes in atmospheric circulation, wind regimes, precipitation, and humidity interact with these components to shape long-term AOD variability. In desert regions, variations in soil moisture, vegetation cover, and surface winds can strongly influence dust emissions and transport, whereas in biomass-burning regions, climate-driven changes in fire frequency and intensity may modulate organic aerosol production. For example, increased aridity and land degradation can enhance dust mobilization, while higher precipitation and vegetation growth can stabilize soils and suppress dust emissions, leading to reduced AOD. These considerations highlight the need for future studies that explicitly link aerosol-speciated trends with meteorological drivers and land–atmosphere interactions, thereby providing a more complete understanding of the mechanisms governing long-term AOD evolution and strengthening the basis for future climate and air-quality assessments.

Data availability. The CAMS global reanalysis (EAC4) data used in this study were obtained from the Copernicus Atmosphere Monitoring Service (CAMS) Atmosphere Data Store (ADS) (Copernicus Atmosphere Monitoring Service, 2020; https://doi.org/10.24381/d58bbf47, accessed on 19-02-2026). The CAMS reanalysis dataset is described in Inness et al. (2019). The Aerosol Robotic Network (AERONET) data are publicly available and can be accessed through the official website at: https://aeronet.gsfc.nasa.gov/. The derived datasets generated in this study—including the regional monthly mean values for all regions of interest (ROIs), global total AOD trends, aerosol-speciated trends, and the corresponding AERONET-based trend and evaluation metrics—will be made publicly available through a Zenodo repository upon publication. These derived products correspond exclusively to the EAC4 dataset.

Author contributions. Conceptualization, A.M., S.K., A.G.; methodology, A.M., S.K., A.G.; software, A.M.; validation, A.M.; writing—original draft preparation, A.M; writing—review and editing, A.M., A.G., S.A.L., J.F., S.R., M.A., A.B., K.T., V.A., S.K.; funding acquisition, S.K. All authors have read and agreed to the published version of the manuscript.

Financial support. This work was supported from COST Action CA21119 Harmonia: International network for harmonization of atmospheric aerosol retrievals from ground-based photometers, supported by COST (European Cooperation in Science and Technology) and ACTRIS Switzerland 2025-2028 grant (Swiss contribution to the ACTRIS ERIC) funded by the Swiss State Secretariat for Education and Research and Innovation (SERI).

Acknowledgment. We gratefully acknowledge the Copernicus Atmosphere Monitoring Service (CAMS) for creating and distributing the CAMS global reanalysis (EAC4) products. We are particularly grateful to the ECMWF team for providing the

https://doi.org/10.5194/egusphere-2026-1107
Preprint. Discussion started: 6 March 2026

CTRL simulation runs used in this study. We also acknowledge the AERONET network and its principal investigators and site managers for providing high-quality sun-photometer observations, calibration, and data products.

Competing interests. At least one of the (co-)authors is a member of the editorial board of Atmospheric Chemistry and Physics.

Disclaimer.

Special issue statement.

References

Ackerman, T. P. and Toon, O. B.: Absorption of visible radiation in atmosphere containing mixtures of absorbing and nonabsorbing particles, Appl. Opt., 20, 3661–3668, doi:10.1364/AO.20.003661, 1981.

Adams, A. M., Prospero, J. M., and Zhang, C.: CALIPSO-derived three-dimensional structure of aerosol over the Atlantic basin and adjacent continents, J. Climate, 25, 6862–6879, doi:10.1175/JCLI-D-11-00672.1, 2012.

Adebiyi, A. A. and Kok, J. F.: Climate models miss most of the coarse dust in the atmosphere, Sci. Adv., 6, eaaz9507, doi:10.1126/sciadv.aaz9507, 2020.

Allen, R. J., Samset, B. H., Wilcox, L. J., and Fisher, R. A.: Are Northern Hemisphere boreal forest fires more sensitive to future aerosol mitigation than to greenhouse gas–driven warming?, Sci. Adv., 10, eadl4007, doi:10.1126/sciadv.adl4007, 2024.

Amiro, B., Cantin, A., Flannigan, M., and de Groot, W.: Future emissions from Canadian boreal forest fires, Can. J. For. Res., 39, 383–395, doi:10.1139/X08-154, 2009.

Ångström, A.: On the atmospheric transmission of sun radiation and on dust in the air, Geogr. Ann., 11, 156–166, doi:10.2307/519399, 1929.

Ansmann, A., Rittmeister, F., Engelmann, R., Basart, S., Jorba, O., Spyrou, C., Remy, S., Skupin, A., Seifert, P., Hiebsch, A., Baars, H., and Wandinger, U.: Profiling of Saharan dust from the Caribbean to western Africa – Part 2: Shipborne lidar measurements versus forecasts, Atmos. Chem. Phys., 17, 14987–15006, doi:10.5194/acp-17-14987-2017, 2017.

Baars, H., Radenz, M., Floutsi, A. A., Engelmann, R., Althausen, D., Heese, B., Ansmann, A., Flament, T., Dabas, A., Trapon, D., Reitebuch, O., Bley, S., and Wandinger, U.: Californian wildfire smoke over Europe: A first example of the aerosol observing capabilities of Aeolus compared to ground-based lidar, Geophys. Res. Lett., 48, e2020GL092194, doi:10.1029/2020GL092194, 2021.

Benedetti, A., Morcrette, J.-J., Boucher, O., Dethof, A., Engelen, R. J., Fisher, M., Flentje, H., Huneeus, N., Jones, L., Kaiser, J. W., Kinne, S., Mangold, A., Razinger, M., Simmons, A. J., Suttie, M., and the GEMS-AER team: Aerosol analysis and forecast in the European Centre for Medium-Range Weather Forecasts Integrated Forecast System: Data Assimilation. J. Geophys. Res., 114, D13205, https://doi.org/10.1029/2008JD011115, 2009.

https://doi.org/10.5194/egusphere-2026-1107
Preprint. Discussion started: 6 March 2026

Blake, L., Arola, A., Benedictow, A., Bennouna, Y., Bouarar, I., Cuevas, E., Errera, Q., Eskes, H. J., Griesfeller, J., Ilic, L., Kapsomenakis, J., Langerock, B., Li, C. W. Y., Mortier, A., Pison, I., Pitkänen, M., Richter, A., Schoenhardt, A., Schulz, M., Tarniewicz, J., Tsikerdekis, A., Warneke, T., and Zerefos, C.: Validation report for the CAMS global reanalyses of aerosol and reactive trace gases: 2003–2024, Copernicus Atmosphere Monitoring Service (CAMS) report, CAMS2_82_2023SC2_D82.4.2.1-2025, doi:10.24380/vv0t-8tcg, 2025.

Buchard, V., Randles, C. A., da Silva, A. M., Darmenov, A., Colarco, P. R., Govindaraju, R., Ferrare, R., Hair, J., Beyersdorf, A. J., Ziemba, L. D., and Yu, H.: The MERRA-2 aerosol reanalysis, 1980 onward. Part II: Evaluation and case studies, J. Clim., 30, 6851–6872, doi:10.1175/JCLI-D-16-0613.1, 2017.

Calef, M. P., Varvak, A., McGuire, A. D., Chapin III, F. S., and Reinhold, K. B.: Recent changes in annual area burned in interior Alaska: The impact of fire management, Earth Interact., 19, 1–17, doi:10.1175/EI-D-14-0025.1, 2015.

Casciaro, G., Cavaiola, M., and Mazzino, A.: Calibrating the CAMS European multi-model air quality forecasts for regional air pollution monitoring, Atmos. Environ., 287, 119259, doi:10.1016/j.atmosenv.2022.119259, 2022.

Ceamanos, X., Coopman, Q., George, M., Riedi, J., Parrington, M., and Clerbaux, C.: Remote sensing and model analysis of biomass burning smoke transported across the Atlantic during the 2020 Western US wildfire season, Sci. Rep., 13, 16014, doi:10.1038/s41598-023-39312-1, 2023.

Che, H., Gui, K., Xia, X., Wang, Y., Holben, B. N., Goloub, P., Cuevas-Agulló, E., Wang, H., Zheng, Y., Zhao, H., and Zhang, X.: Large contribution of meteorological factors to inter-decadal changes in regional aerosol optical depth, Atmos. Chem. Phys., 19, 10497–10523, doi:10.5194/acp-19-10497-2019, 2019.

Che, H., Xia, X., Zhu, J., Li, Z., Dubovik, O., Holben, B., Goloub, P., Chen, H., Estellés, V., Cuevas-Agulló, E., Blarel, L., Wang, H., Zhao, H., Zhang, X., Wang, Y., Sun, J., Tao, R., Zhang, X., and Shi, G.: Column aerosol optical properties and aerosol radiative forcing during a serious haze-fog month over North China Plain in 2013 based on ground-based sunphotometer measurements, Atmos. Chem. Phys., 14, 2125–2138, doi:10.5194/acp-14-2125-2014, 2014.

Che, H., Zhang, X., Li, Y., Zhou, Z., and Qu, J. J.: Horizontal visibility trends in China, 1981–2005, Geophys. Res. Lett., 34, L24706, doi:10.1029/2007GL031450, 2007.

Chen, J., Li, C., Ristovski, Z., Milic, A., Gu, Y., Islam, M. S., Wang, S., Hao, J., Zhang, H., He, C., Guo, H., Fu, H., Miljevic, B., Morawska, L., Thai, P., Lam, Y. F., Pereira, G., Ding, A., Huang, X., and Dumka, U. C.: A review of biomass burning: Emissions and impacts on air quality, health and climate in China, Sci. Total Environ., 579, 1000–1034, doi:10.1016/j.scitotenv.2016.11.025, 2017.

Chin, M., Diehl, T., Tan, Q., Prospero, J. M., Kahn, R. A., Remer, L. A., Yu, H., Sayer, A. M., Bian, H., Geogdzhayev, I. V., Holben, B. N., Howell, S. G., Huebert, B. J., Hsu, N. C., Kim, D., Kucsera, T. L., Levy, R. C., Mishchenko, M. I., Pan, X., Quinn, P. K., Schuster, G. L., Streets, D. G., Strode, S. A., Torres, O., and Zhao, X.-P.: Multi-decadal aerosol variations from 1980 to 2009: a perspective from observations and a global model, Atmos. Chem. Phys., 14, 3657–3690, doi:10.5194/acp-14-3657-2014, 2014.

https://doi.org/10.5194/egusphere-2026-1107
Preprint. Discussion started: 6 March 2026

Choi, Y., Chen, S.-H., Huang, C.-C., Earl, K., Chen, C.-Y., Schwartz, C. S., and Matsui, T.: Evaluating the impact of assimilating aerosol optical depth observations on dust forecasts over North Africa and the East Atlantic using different data assimilation methods, *J. Adv. Model. Earth Sy.*, 12, e2019MS001890, doi:10.1029/2019MS001890, 2020.

Cohen, A. J., Brauer, M., Burnett, R., Anderson, H. R., Frostad, J., Estep, K., Balakrishnan, K., Brunekreef, B., Dandona, L., Dandona, R., Feigin, V., Freedman, G., Hubbell, B., Jobling, A., Kan, H., Knibbs, L., Liu, Y., Martin, R., Morawska, L., Pope, C. A., Shin, H., Straif, K., Shaddick, G., Thomas, M., van Dingenen, R., van Donkelaar, A., Vos, T., Murray, C. J. L., and Forouzanfar, M. H.: Estimates and 25-year trends of the global burden of disease attributable to ambient air pollution: an analysis of data from the Global Burden of Diseases Study 2015, Lancet, 389, 1907–1918, doi:10.1016/S0140-6736(17)30505-6, 2017.

Collaud Coen, M., Andrews, E., Bigi, A., Martucci, G., Romanens, G., Vogt, F. P. A., and Vuilleumier, L.: Effects of the prewhitening method, the time granularity, and the time segmentation on the Mann–Kendall trend detection and the associated Sen's slope, Atmos. Meas. Tech., 13, 6945–6964, doi:10.5194/amt-13-6945-2020, 2020.

Courtier, P., Thépaut, J.-N., and Hollingsworth, A.: A strategy for operational implementation of 4D-Var, using an incremental approach, *Q. J. R. Meteorol. Soc.*, 120, 1367–1387, doi:10.1002/qj.49712051912, 1994.

Copernicus Atmosphere Monitoring Service (CAMS) Atmosphere Data Store, DOI: 10.24381/d58bbf47 (Accessed on 19/02/2026).

Cuevas-Agulló, E., Barriopedro, D., García, R. D., Alonso-Pérez, S., González-Alemán, J. J., Werner, E., Suárez, D., Bustos, J. J., García-Castrillo, G., García, O., Barreto, Á., and Basart, S.: Sharp increase in Saharan dust intrusions over the western Euro-Mediterranean in February–March 2020–2022 and associated atmospheric circulation, Atmos. Chem. Phys., 24, 4083–4104, doi:10.5194/acp-24-4083-2024, 2024.

De Leeuw, G., Sogacheva, L., Rodriguez, E., Kourtidis, K., Georgoulias, A. K., Alexandri, G., Amiridis, V., Proestakis, E., Marinou, E., Xue, Y., and van der A, R.: Two decades of satellite observations of AOD over mainland China using ATSR-2, AATSR and MODIS/Terra: data set evaluation and large-scale patterns, Atmos. Chem. Phys., 18, 1573–1592, doi:10.5194/acp-18-1573-2018, 2018.

Dentener, F., Kinne, S., Bond, T., Boucher, O., Cofala, J., Generoso, S., Ginoux, P., Gong, S., Hoelzemann, J. J., Ito, A., Marelli, L., Penner, J. E., Putaud, J.-P., Textor, C., Schulz, M., van der Werf, G. R., and Wilson, J.: Emissions of primary aerosol and precursor gases in the years 2000 and 1750 – prescribed data-sets for AeroCom, Atmos. Chem. Phys., 6, 4321–4344, doi:10.5194/acp-6-4321-2006, 2006.

Di Giuseppe, F., Rémy, S., Pappenberger, F., and Wetterhall, F.: Improving forecasts of biomass burning emissions with the fire weather index, *J. Appl. Meteorol. Clim.*, 56, 2789–2799, doi:10.1175/JAMC-D-16-0405.1, 2017.

Di Tomaso, E., Schutgens, N. A. J., Jorba, O., and Pérez García-Pando, C.: Assimilation of MODIS Dark Target and Deep Blue observations in the dust aerosol component of NMMB-MONARCH version 1.0, *Geosci. Model Dev.*, 10, 1107–1129, doi:10.5194/gmd-10-1107-2017, 2017.

https://doi.org/10.5194/egusphere-2026-1107
Preprint. Discussion started: 6 March 2026

Ding, A. J., Huang, X., Nie, W., Sun, J. N., Kerminen, V.-M., Petäjä, T., Su, H., Cheng, Y. F., Yang, X.-Q., Wang, M. H., Chi, X. G., Wang, J. P., Virkkula, A., Guo, W. D., Yuan, J., Wang, S. Y., Zhang, R. J., Wu, Y. F., Song, Y., Zhu, T., Zilitinkevich, S., Kulmala, M., and Fu, C. B.: Black carbon enhances haze pollution in megacities in China, Geophys. Res. Lett., 43, 2873–2879, doi:10.1002/2016GL067745, 2016.

Eskes, H., Tsikerdekis, A., Ades, M., Alexe, M., Benedictow, A. C., Bennouna, Y., Blake, L., Bouarar, I., Chabrillat, S., Engelen, R., Errera, Q., Flemming, J., Garrigues, S., Griesfeller, J., Huijnen, V., Ilić, L., Inness, A., Kapsomenakis, J., Kipling, Z., Langerock, B., Mortier, A., Parrington, M., Pison, I., Pitkänen, M., Rémy, S., Richter, A., Schoenhardt, A., Schulz, M., Thouret, V., Warneke, T., Zerefos, C., and Peuch, V.-H.: Technical note: Evaluation of the Copernicus Atmosphere Monitoring Service Cy48R1 upgrade of June 2023, *Atmos. Chem. Phys.*, 24, 9475–9514, doi:10.5194/acp-24-9475-2024, 2024.

Evan, A. T.: Surface winds and dust biases in climate models, Geophys. Res. Lett., 45, 1079–1085, doi:10.1002/2017GL076353, 2018.

Hammer, M. S., Martin, R. V., Li, C., Torres, O., Manning, M., and Boys, B. L.: Insight into global trends in aerosol composition from 2005 to 2015 inferred from the OMI Ultraviolet Aerosol Index, Atmos. Chem. Phys., 18, 8097–8112, doi:10.5194/acp-18-8097-2018, 2018.

Hirsch, E., and Koren, I.: Record-breaking aerosol levels explained by smoke injection into the stratosphere, *Science*, 371(6535), 1269–1274, doi:10.1126/science.abe1415, 2021.

Holben, B. N., Eck, T. F., Slutsker, I., Tanré, D., Buis, J. P., Setzer, A., Vermote, E., Reagan, J. A., Kaufman, Y. J., Nakajima, T., Lavenu, F., Jankowiak, I., and Smirnov, A.: AERONET – A federated instrument network and data archive for aerosol characterization, Remote Sens. Environ., 66, 1–16, doi:10.1016/S0034-4257(98)00031-5, 1998.

Holben, B. N., Tanré, D., Smirnov, A., Eck, T. F., Slutsker, I., Abuhassan, N., Newcomb, W. W., Schafer, J. S., Chatenet, B., Lavenu, F., Kaufman, Y. J., Vande Castle, J., Setzer, A., Markham, B., Clark, D., Frouin, R., Halthore, R., Karnieli, A., O'Neill, N. T., Pietras, C., Pinker, R. T., Voss, K., and Zibordi, G.: Giles

Eck, T. F., Holben, B. N., Reid, J. S., Dubovik, O., Smirnov, A., O'Neill, N. T., Slutsker, I., and Kinne, S.: Wavelength dependence of the optical depth of biomass burning, urban, and desert dust aerosols, J. Geophys. Res., 104, 31333–31349, doi:10.1029/1999JD900923, 1999.

Flannigan, M. D., Logan, K. A., Amiro, B. D., Skinner, W. R., and Stocks, B. J.: Future area burned in Canada, Clim. Change, 72, 1–16, doi:10.1007/s10584-005-5935-y, 2005.

Flemming, J., Huijnen, V., Arteta, J., Bechtold, P., Beljaars, A., Blechschmidt, A.-M., Diamantakis, M., Engelen, R. J., Gaudel, A., Inness, A., Jones, L., Josse, B., Katragkou, E., Marécal, V., Peuch, V.-H., Richter, A., Schultz, M. G., Stein, O., and Tsikerdekis, A.: Tropospheric chemistry in the Integrated Forecasting System of ECMWF, Geosci. Model Dev., 8, 975–1003, doi:10.5194/gmd-8-975-2015, 2015.

Flemming, J., Benedetti, A., Inness, A., Engelen, R. J., Jones, L., Huijnen, V., Remy, S., Parrington, M., Suttie, M., Bozzo, A., Peuch, V.-H., Akritidis, D., and Katragkou, E.: The CAMS interim Reanalysis of Carbon Monoxide, Ozone and Aerosol for 2003–2015, Atmos. Chem. Phys., 17, 1945–1983, doi:10.5194/acp-17-1945-2017, 2017.

https://doi.org/10.5194/egusphere-2026-1107
Preprint. Discussion started: 6 March 2026

Flemming, J., and Innes, A.: Carbon monoxide, in: State of the Climate in 2023, Bull. Am. Meteorol. Soc., 105, S76–S79, doi:10.1175/BAMS-D-24-0116.1, 2024.

Gelaro, R., McCarty, W., Suárez, M. J., Todling, R., Molod, A., Takacs, L., Randles, C. A., Darmenov, A., Bosilovich, M. G., Reichle, R., Wargan, K., Coy, L., Cullather, R., Draper, C., Akella, S., Buchard, V., Conaty, A., da Silva, A. M., Gu, W., Kim, G. K., Koster, R., Lucchesi, R., Merkova, D., Nielsen, J. E., Partyka, G., Pawson, S., Putman, W., Rienecker, M., Schubert, S. D., Sienkiewicz, M., and Zhao, B.: The modern-era retrospective analysis for research and applications, version 2 (MERRA-2), J. Clim., 30, 5419–5454, doi:10.1175/JCLI-D-16-0758.1, 2017.

Giles, D. M., Sinyuk, A., Sorokin, M. G., Schafer, J. S., Smirnov, A., Slutsker, I., Eck, T. F., Holben, B. N., Lewis, J. R., Campbell, J. R., Welton, E. J., Korkin, S. V., and Lyapustin, A. I.: Advancements in the Aerosol Robotic Network (AERONET) Version 3 database – automated near-real-time quality control algorithm with improved cloud screening for Sun photometer aerosol optical depth (AOD) measurements, Atmos. Meas. Tech., 12, 169–209, doi:10.5194/amt-12-169-2019, 2019.

Ginoux, P., Chin, M., Tegen, I., Prospero, J. M., Holben, B., Dubovik, O., and Lin, S.-J.: Sources and distributions of dust aerosols simulated with the GOCART model, J. Geophys. Res., 106, 20255–20273, doi:10.1029/2000JD000053, 2001.

Ginoux, P., Prospero, J. M., Gill, T. E., Hsu, N. C., and Zhao, M.: Global-scale attribution of anthropogenic and natural dust sources and their emission rates based on MODIS Deep Blue aerosol products, Rev. Geophys., 50, RG3005, doi:10.1029/2012RG000388, 2012.

Gkikas, A., Hatzianastassiou, N., Mihalopoulos, N., Katsoulis, V., Kazadzis, S., Pey, J., Querol, X., and Torres, O.: The regime of intense desert dust episodes in the Mediterranean based on contemporary satellite observations and ground measurements, *Atmos. Chem. Phys.*, 13, 12135–12154, doi:10.5194/acp-13-12135-2013, 2013.

Gkikas, A., Houssos, E. E., Lolis, C. J., Bartzokas, A., Mihalopoulos, N., and Hatzianastassiou, N.: Atmospheric circulation evolution related to desert-dust episodes over the Mediterranean, Q. J. Roy. Meteor. Soc., 141, 1634–1645, doi:10.1002/qj.2466, 2015.

Gkikas, A., Basart, S., Hatzianastassiou, N., Marinou, E., Amiridis, V., Kazadzis, S., Pey, J., Querol, X., Jorba, O., Gassó, S., and Baldasano, J. M.: Mediterranean intense desert dust outbreaks and their vertical structure based on remote sensing data, *Atmos. Chem. Phys.*, 16, 8609–8642, doi:10.5194/acp-16-8609-2016, 2016.

Gkikas, A., Proestakis, E., Amiridis, V., Kazadzis, S., Di Tomaso, E., Tsekeri, A., Marinou, E., Hatzianastassiou, N., and Pérez García-Pando, C.: ModIs Dust AeroSol (MIDAS): a global fine-resolution dust optical depth data set, Atmos. Meas. Tech., 14, 309–334, doi:10.5194/amt-14-309-2021, 2021.

Garrigues, S., Ades, M., Remy, S., Flemming, J., Kipling, Z., Laszlo, I., Parrington, M., Inness, A., Ribas, R., Jones, L., Engelen, R., and Peuch, V.-H.: Impact of assimilating NOAA VIIRS aerosol optical depth (AOD) observations on global AOD analysis from the Copernicus Atmosphere Monitoring Service (CAMS), Atmos. Chem. Phys., 23, 10473–10487, https://doi.org/10.5194/acp-23-10473-2023, 2023.

https://doi.org/10.5194/egusphere-2026-1107
Preprint. Discussion started: 6 March 2026

Gui, K., Che, H., Li, L., Zheng, Y., Zhang, L., Zhao, H., Zhong, J., Yao, W., Liang, Y., Wang, Y., and Zhang, X.: The significant contribution of small-sized and spherical aerosol particles to the decreasing trend in total aerosol optical depth over land from 2003 to 2018, Engineering, 16, 82–92, doi:10.1016/j.eng.2021.05.017, 2022.

Gui, K., Che, H., Zheng, Y., Wang, Y., Zhang, L., Zhao, H., Li, L., Zhong, J., Yao, W., and Zhang, X.: Seasonal variability and trends in global type-segregated aerosol optical depth as revealed by MISR satellite observations, Sci. Total Environ., 787, 147543, doi:10.1016/j.scitotenv.2021.147543, 2021.

Granier, C., Bessagnet, B., Bond, T., D'Angiola, A., Denier van der Gon, H., Frost, G. J., Heil, A., Kaiser, J. W., Kinne, S., Klimont, Z., Kloster, S., Lamarque, J.-F., Liousse, C., Masui, T., Meleux, F., Mieville, A., Ohara, T., Raut, J.-C., Riahi, K., Schultz, M. G., Smith, S. G., Thompson, A., van Aardenne, J., van der Werf, G. R., and van Vuuren, D. P.: Evolution of anthropogenic and biomass burning emissions of air pollutants at global and regional scales during the 1980–2010 period, Climatic Change, 109, 163–190, doi:10.1007/s10584-011-0154-1, 2011.

Hanes, C. C., Wang, X., Jain, P., Parisien, M.-A., Little, J. M., and Flannigan, M. D.: Fire-regime changes in Canada over the last half century, Can. J. For. Res., 49, 256–269, doi:10.1139/cjfr-2018-029, 2019.

Hansen, J., Sato, M., and Ruedy, R.: Radiative forcing and climate response, J. Geophys. Res.-Atmos., 102, 6831–6864, doi:10.1029/96JD03436, 1997.

Haywood, J. and Boucher, O.: Estimates of the direct and indirect radiative forcing due to tropospheric aerosols: a review, Rev. Geophys., 38, 513–543, doi:10.1029/1999RG000078, 2000.

Huijnen, V., Williams, J., van Weele, M., van Noije, T., Krol, M., Dentener, F., Segers, A., Houweling, S., Peters, W., de Laat, J., Boersma, F., Bergamaschi, P., van Velthoven, P., Le Sager, P., Eskes, H., Alkemade, F., Scheele, R., Nédélec, P., and Pätz, H.-W.: The global chemistry transport model TM5: description and evaluation of the tropospheric chemistry version 3.0, Geosci. Model Dev., 3, 445–473, doi:10.5194/gmd-3-445-2010, 2010.

Hussain, M., Mahmud, I., and Zafar, S.: pyMannKendall: a Python package for non-parametric Mann–Kendall family of trend tests, J. Open Source Softw., 4, 1556, doi:10.21105/joss.01556, 2019.

Inness, A., Ades, M., Agustí-Panareda, A., Barré, J., Benedictow, A., Blechschmidt, A.-M., Dominguez, J. J., Engelen, R., Eskes, H., Flemming, J., Huijnen, V., Jones, L., Kipling, Z., Massart, S., Parrington, M., Peuch, V.-H., Razinger, M., Remy, S., Schulz, M., and Suttie, M.: The CAMS reanalysis of atmospheric composition, Atmos. Chem. Phys., 19, 3515–3556, doi:10.5194/acp-19-3515-2019, 2019.

Inness, A., Blechschmidt, A.-M., Bouarar, I., Chabrillat, S., Crepulja, M., Engelen, R., Eskes, H., Flemming, J., Gaudel, A., Hendrick, F., et al.: Data assimilation of satellite-retrieved ozone, carbon monoxide and nitrogen dioxide with ECMWF's Composition-IFS, *Atmos. Chem. Phys.*, 15, 5275–5303, doi:10.5194/acp-15-5275-2015, 2015.

IPCC: Climate Change 2021: The Physical Science Basis, Contribution of Working Group I to the Sixth Assessment Report of the Intergovernmental Panel on Climate Change, Cambridge University Press, doi:10.1017/9781009157896, 2021.

Jiang, J. H., Su, H., Huang, L., Wang, Y., Massie, S., Zhao, B., Omar, A., and Wang, Z.: Contrasting effects on deep convective clouds by different types of aerosols, Nat. Commun., 9, 3874, doi:10.1038/s41467-018-06280-4, 2018.

https://doi.org/10.5194/egusphere-2026-1107
Preprint. Discussion started: 6 March 2026

Kaiser, J. W., Heil, A., Andreae, M. O., Benedetti, A., Chubarova, N., Jones, L., Morcrette, J.-J., Razinger, M., Schultz, M. G., Suttie, M., and van der Werf, G. R.: Biomass burning emissions estimated with a global fire assimilation system based on observed fire radiative power, Biogeosciences, 9, 527–554, doi:10.5194/bg-9-527-2012, 2012.

Kaiser, J. W., Parrington, M., and Armenteras, D.: Biomass burning, in: State of the Climate in 2023, Bull. Am. Meteorol. Soc., 105, S76–S79, doi:10.1175/BAMS-D-24-0116.1, 2024.

Karanikolas, A., Torres, B., Momoi, M., Herreras-Giralda, M., Kouremeti, N., Gröbner, J., Doppler, L., and Kazadzis, S.: Retrieval of aerosol properties from direct solar irradiance measurements with high temporal resolution and spectral range, EGUsphere [preprint], doi:10.5194/egusphere-2025-2061, 2025.

Kaufman, Y. J., Ichoku, C., Giglio, L., Korontzi, S., Chu, D. A., Hao, W. M., Li, R.-R., and Justice, C. O.: Fires and smoke observed from the Earth Observing System MODIS instrument – products, validation, and operational use, Int. J. Remote Sens., 24, 1765–1781, doi:10.1080/01431160210144741, 2003.

Kendall, M. G.: Rank Correlation Methods, 4th Edn., Griffin, London, ISBN 0852641990, 1975.

Klingmüller, K., Pozzer, A., Metzger, S., Stenchikov, G. L., and Lelieveld, J.: Aerosol optical depth trend over the Middle East, *Atmos. Chem. Phys.*, 16, 5063–5073, doi:10.5194/acp-16-5063-2016, 2016.

King, M. D., Menzel, W. P., Kaufman, Y. J., Tanré, D., Gao, B. C., Platnick, S., Ackerman, S. A., Remer, L. A., Pincus, R., and Hubanks, P. A.: Cloud and aerosol properties, precipitable water, and profiles of temperature and water vapor from MODIS, IEEE T. Geosci. Remote, 41, 442–456, doi:10.1109/TGRS.2002.808226, 2003.

Kok, J. F., Storelvmo, T., Karydis, V. A., Adebiyi, A. A., Mahowald, N. M., Evan, A. T., He, C., and Leung, D. M.: Mineral dust aerosol impacts on global climate and climate change, Nat. Rev. Earth Environ., 4, 71–86, doi:10.1038/s43017-022-00379-5, 2023.

Kulkarni, A. and von Storch, H.: Simulationsexperimente zur Wirkung serieller Korrelation auf den Mann–Kendall Trendtest, Meteorol. Z., 4, 82–85, doi:10.1127/metz/4/1992/82, 1992.

Langerock, B., Arola, A., Benedictow, A., Bennouna, Y., Blake, L., Bouarar, I., Cuevas, E., Errera, Q., Eskes, H. J., Griesfeller, J., Ilić, L., Kapsomenakis, J., Li, C. W. Y., Mortier, A., Pison, I., Pitkänen, M., Richter, A., Schoenhardt, A., Schulz, M., Tarniewicz, J., Tsikerdekis, A., Warneke, T., and Zerefos, C.: Validation report for the CAMS global reanalyses of aerosol and reactive trace gases: 2003–2023, *Copernicus Atmosphere Monitoring Service (CAMS) report*, CAMS2_82_2023SC2_D82.4.2.1-2024, doi:10.24380/g8h7-kd21, 2024.

Levy, R. C., Remer, L. A., Kleidman, R. G., Mattoo, S., Ichoku, C., Kahn, R., and Eck, T. F.: Global evaluation of the Collection 5 MODIS dark-target aerosol products over land, Atmos. Chem. Phys., 10, 10399–10420, doi:10.5194/acp-10-10399-2010, 2010.

Levy, R. C., Munchak, L. A., Mattoo, S., Patadia, F., Remer, L. A., and Holz, R. E.: Towards a long-term global aerosol optical depth record: applying a consistent aerosol retrieval algorithm to MODIS and VIIRS-observed reflectance, Atmos. Meas. Tech., 8, 4083–4110, doi:10.5194/amt-8-4083-2015, 2015.

https://doi.org/10.5194/egusphere-2026-1107
Preprint. Discussion started: 6 March 2026

Levy, R. C., Mattoo, S., Sawyer, V., Shi, Y., Colarco, P. R., Lyapustin, A. I., Wang, Y., and Remer, L. A.: Exploring systematic offsets between aerosol products from the two MODIS sensors, Atmos. Meas. Tech., 11, 4073–4092, doi:10.5194/amt-11-4073-2018, 2018.

Li, J., Carlson, B. E., Dubovik, O., and Lacis, A. A.: Recent trends in aerosol optical properties derived from AERONET measurements, Atmos. Chem. Phys., 14, 12271–12289, doi:10.5194/acp-14-12271-2014, 2014.

Li, W., Xu, L., Liu, X., Zhang, J., Lin, Y., Yao, X., Gao, H., Zhang, D., Chen, J., Wang, W., Harrison, R. M., Zhang, X., Shao, L., Fu, P., Nenes, A., and Shi, Z.: Air pollution–aerosol interactions produce more bioavailable iron for ocean ecosystems, Sci. Adv., 3, e1601749, doi:10.1126/sciadv.1601749, 2017.

Li, Z., Guo, J., Ding, A., Liao, H., Liu, J., Sun, Y., Wang, T., Xue, H., Zhang, H., and Zhu, B.: Aerosol and boundary-layer interactions and impact on air quality, Natl. Sci. Rev., 4, 810–833, doi:10.1093/nsr/nwx117, 2017.

Li, J.: Pollution trends in China from 2000 to 2017: A multi-sensor view from space, Remote Sens., 12, 208, doi:10.3390/rs12020208, 2020.

Li, M., Shen, F., and Sun, X.: 2019–2020 Australian bushfire air particulate pollution and impact on the South Pacific Ocean, Sci. Rep., 11, 12288, doi:10.1038/s41598-021-91547-y, 2021.

Liu, J., Ren, C., Huang, X., Nie, W., Wang, J., Sun, P., Chi, X., and Ding, A.: Increased aerosol extinction efficiency hinders visibility improvement in eastern China, Geophys. Res. Lett., 47, e2020GL090167, doi:10.1029/2020GL090167, 2020.

Liu, J., Rühland, K. M., Chen, J., Xu, Y., Chen, S., Chen, Q., Huang, W., Xu, Q., Chen, F., and Smol, J. P.: Aerosol-weakened summer monsoons decrease lake fertilization on the Chinese Loess Plateau, Nat. Clim. Change, 7, 190–194, doi:10.1038/nclimate3220, 2017.

Liu, X., Gu, J., Li, Y., Cheng, Y., Qu, Y., Han, T., Wang, J., Tian, H., Chen, J., and Zhang, Y.: Increase of aerosol scattering by hygroscopic growth: observation, modeling, and implications on visibility, Atmos. Res., 132–133, 91–101, doi:10.1016/j.atmosres.2013.04.007, 2013.

Lohmann, U. and Feichter, J.: Global indirect aerosol effects: a review, Atmos. Chem. Phys., 5, 715–737, doi:10.5194/acp-5-715-2005, 2005.

Logothetis, S. A., Salamalikis, V., Gkikas, A., Kazadzis, S., Amiridis, V., and Kazantzidis, A.: 15-year variability of desert dust optical depth on global and regional scales, *Atmos. Chem. Phys.*, 21, 16499–16534, doi:10.5194/acp-21-16499-2021, 2021.

Lund, M. T., Nordling, K., Gjelsvik, A. B., and Samset, B. H.: The influence of variability on fire weather conditions in high latitude regions under present and future global warming, Environ. Res. Commun., 5, 065016, doi:10.1088/2515-7620/acdfad, 2023.

MacDonald, G., Wall, T., Enquist, C. A. F., LeRoy, S. R., Bradford, J. B., Breshears, D. D., Brown, T., and co-authors: Drivers of California's changing wildfires: a state-of-the-knowledge synthesis, Int. J. Wildland Fire, 32, 1039–1058, doi:10.1071/WF22155, 2023.

Mann, H. B.: Nonparametric tests against trend, Econometrica, 13, 245–259, doi:10.2307/1907187, 1945.

https://doi.org/10.5194/egusphere-2026-1107
Preprint. Discussion started: 6 March 2026

Maring, H., Savoie, D. L., Izaguirre, M. A., Custals, L., and Reid, J. S.: Mineral dust aerosol size distribution change during atmospheric transport, J. Geophys. Res., 108, 8592, doi:10.1029/2002JD002536, 2003.

Marticorena, B. and Bergametti, G.: Modeling the atmospheric dust cycle: 1. Design of a soil-derived dust emission scheme, J. Geophys. Res., 100, 16415–16430, doi:10.1029/95JD00690, 1995.

Masoom, A., Kazadzis, S., Modini, R. L., Gysel-Beer, M., Gröbner, J., Coen, M. C., Navas-Guzman, F., Kouremeti, N., Brem, B. T., Nowak, N. K., Martucci, G., Hervo, M., and Erb, S.: Long range transport of Canadian wildfire smoke to Europe in Fall 2023: aerosol properties and spectral features of smoke particles, EGUsphere [preprint], doi:10.5194/egusphere-2025-2755, 2025.

Meng, X., Yu, Y., and Ginoux, P.: Rise in dust emissions from burned landscapes primarily driven by small fires, Nat. Geosci., 1–7, doi:10.1038/s41561-025-01730-3, 2025.

Monahan, E. C., Spiel, D. E., and Davidson, K. L.: A model of marine aerosol generation via whitecaps and wave disruption, in: Oceanic Whitecaps, edited by: Monahan, E. and Niocaill, G. M., D. Reidel, Norwell, Mass., 167–174, 1986.

Moustaka, A., Korras-Carraca, M.-B., Papachristopoulou, K., Stamatis, M., Fountoulakis, I., Kazadzis, S., Proestakis, E., et al.: Assessing lidar ratio impact on CALIPSO retrievals utilized for the estimation of aerosol SW radiative effects across North Africa, the Middle East, and Europe, Remote Sens., 16, 1689, doi:10.3390/rs16101689, 2024.

Morcrette, J.-J., Boucher, O., Jones, L., Salmond, D., Bechtold, P., Beljaars, A., Benedetti, A., Bonet, A., Kaiser, J. W., Razinger, M., Schulz, M., Serrar, S., Simmons, A. J., Sofiev, M., Suttie, M., Tompkins, A. M., and Untch, A.: Aerosol analysis and forecast in the European Centre for Medium-Range Weather Forecasts Integrated Forecast System: Forward modeling, J. Geophys. Res., 114, D06206, doi:10.1029/2008JD011235, 2009.

Muhs, D. R.: The geologic records of dust in the Quaternary, Aeolian Res., 9, 3–48, doi:10.1016/j.aeolia.2012.08.001, 2013.

Park, C. Y., Takahashi, K., Li, F., Takakura, J., Fujimori, S., Hasegawa, T., Ito, A., Lee, D. K., and Thiery, W.: Impact of climate and socioeconomic changes on fire carbon emissions in the future: Sustainable economic development might decrease future emissions, Glob. Environ. Change, 80, 102667, doi:10.1016/j.gloenvcha.2023.102667, 2023.

Pedreira Júnior, A. L., Curado, L. F. A., Palácios, R. S., Santos, L. O. F., Querino, C. A. S., Querino, J. K. A. S., Rodrigues, T. R., and Marques, J. B.: Evaluation of Aerosol Optical Depth (AOD) estimated by Copernicus Atmosphere Monitoring Service (CAMS) in Brazil, Theor. Appl. Climatol., 156, 116, doi:10.1007/s00704-024-05335-5, 2025.

Peuch, V.-H., Engelen, R., Rixen, M., Dee, D., Flemming, J., Suttie, M., Ades, M., Agustí-Panareda, A., Ananasso, C., Andersson, E., Armstrong, D., Barré, J., Bousserez, N., Dominguez, J. J., Garrigues, S., Inness, A., Jones, L., Kipling, Z., Letertre-Danczak, J., … Thépaut, J.-N.: The Copernicus Atmosphere Monitoring Service: from research to operations, Bull. Am. Meteorol. Soc., 103, E2650–E2668, doi:10.1175/BAMS-D-21-0314.1, 2022.

Quaas, J., Jia, H., Smith, C., Albright, A. L., Aas, W., Bellouin, N., Boucher, O., Doutriaux-Boucher, M., Forster, P. M., Grosvenor, D., Jenkins, S., Klimont, Z., Loeb, N. G., Ma, X., Naik, V., Paulot, F., Stier, P., Wild, M., Myhre, G., and Schulz, M.: Robust evidence for reversal of the trend in aerosol effective climate forcing, *Atmos. Chem. Phys.*, 22, 12221–12239, doi:10.5194/acp-22-12221-2022, 2022.

https://doi.org/10.5194/egusphere-2026-1107
Preprint. Discussion started: 6 March 2026

Satheesh, S. K., Babu, S. S., Padmakumari, B., Pandithurai, G., and Soni, V. K.: Variability of atmospheric aerosols over India, in: Observed Climate Variability and Change over the Indian Region, Springer, Singapore, 221–248, doi:10.1007/978-981-10-2531-0_13, 2017.

Sbai, S. E., Bentayeb, F., and Yin, H.: Atmospheric pollutants response to the emission reduction and meteorology during the COVID-19 lockdown in the north of Africa (Morocco), Stoch. Environ. Res. Risk Assess., 36, 3769–3784, doi:10.1007/s00477-022-02224-z, 2022.

Sinyuk, A., Holben, B. N., Eck, T. F., Giles, D. M., Slutsker, I., Korkin, S., Schafer, J. S., Smirnov, A., Sorokin, M., and Lyapustin, A.: The AERONET Version 3 aerosol retrieval algorithm, associated uncertainties and comparisons to Version 2, Atmos. Meas. Tech., 13, 3375–3411, doi:10.5194/amt-13-3375-2020, 2020.

Stein, O., Schultz, M. G., Bouarar, I., Clark, H., Huijnen, V., Gaudel, A., George, M., and Clerbaux, C.: On the wintertime low bias of Northern Hemisphere carbon monoxide found in global model simulations, Atmos. Chem. Phys., 14, 9295–9316, doi:10.5194/acp-14-9295-2014, 2014.

Stuut, J. B., Boersen, B., Brück, H. M., Hansen, A., Koster, B., van der Does, M., and Witte, Y.: Cruise Report RV Meteor M89, TRAFFIC I: Transatlantic Fluxes of Saharan Dust, 3–25 October 2012, available at: http://melia.nioz.nl/public/dmg/rpt/crs/m89.pdf (last access: 19 September 2025), 2012.

Peterson, D. A., Campbell, J. R., Hyer, E. J., Fromm, M. D., Kablick, G. P., Cossuth, J. H., and co-authors: Wildfire-driven thunderstorms cause a volcano-like stratospheric injection of smoke, npj Clim. Atmos. Sci., 1, 30, doi:10.1038/s41612-018-0039-3, 2018.

Popp, T., de Leeuw, G., Bingen, C., Brühl, C., Capelle, V., Chedin, A., Clarisse, L., Dubovik, O., Grainger, R., Griesfeller, J., Heckel, A., Kinne, S., Klüser, L., Kosmale, M., Kolmonen, P., Lelli, L., Litvinov, P., Mei, L., North, P., Pinnock, S., Povey, A., Robert, C., Schulz, M., Sogacheva, L., Stebel, K., Zweers, D. S., Thomas, G., Tilstra, L. G., Vandenbussche, S., Veefkind, P., Vountas, M., and Xue, Y.: Development, production and evaluation of aerosol climate data records from European satellite observations (Aerosol_cci), Remote Sens., 8, 421, doi:10.3390/rs8050421, 2016.

Proestakis, E., Amiridis, V., Marinou, E., Georgoulias, A. K., Solomos, S., Kazadzis, S., Chimot, J., Che, H., Alexandri, G., Binietoglou, I., Daskalopoulou, V., Kourtidis, K. A., de Leeuw, G., and van der A, R. J.: Nine-year spatial and temporal evolution of desert dust aerosols over South and East Asia as revealed by CALIOP, Atmos. Chem. Phys., 18, 1337–1362, doi:10.5194/acp-18-1337-2018, 2018.

Prospero, J. M., Ginoux, P., Torres, O., Nicholson, S. E., and Gill, T. E.: Environmental characterization of global sources of atmospheric soil dust identified with the Nimbus 7 Total Ozone Mapping Spectrometer (TOMS) absorbing aerosol product, Rev. Geophys., 40, 2-1–2-31, doi:10.1029/2000RG000095, 2002.

Ramo, R., Roteta, E., Bistinas, I., van Wees, D., Bastarrika, A., Chuvieco, E., and van der Werf, G. R.: African burned area and fire carbon emissions are strongly impacted by small fires undetected by coarse resolution satellite data, Proc. Natl. Acad. Sci. USA, 118, e2011160118, doi:10.1073/pnas.2011160118, 2021.

https://doi.org/10.5194/egusphere-2026-1107
Preprint. Discussion started: 6 March 2026

Ridley, D. A., Heald, C. L., Ridley, K. J., and Kroll, J. H.: Causes and consequences of decreasing atmospheric organic aerosol in the United States, Proc. Natl. Acad. Sci. USA, 115, 290–295, doi:10.1073/pnas.1700387115, 2018.

Sen, P. K.: Estimates of the regression coefficient based on Kendall's tau, J. Am. Stat. Assoc., 63, 1379–1389, doi:10.1080/01621459.1968.10480934, 1968.

Sindelarova, K., Granier, C., Bouarar, I., Guenther, A., Tilmes, S., Stavrakou, T., Müller, J.-F., Kuhn, U., Stefani, P., and Knorr, W.: Global data set of biogenic VOC emissions calculated by the MEGAN model over the last 30 years, *Atmos. Chem. Phys.*, 14, 9317–9341, doi:10.5194/acp-14-9317-2014, 2014.

Smith, M. H., Park, P. M., and Consterdine, I. E.: Marine aerosol concentrations and estimated fluxes over the sea, Q. J. R. Meteorol. Soc., 119, 809–824, doi:10.1002/qj.49711951211, 1993.

Sun, T., Che, H., Qi, B., Wang, Y., Dong, Y., Xia, X., Wang, H., Gui, K., Zheng, Y., Zhao, H., Ma, Q., Du, R., and Zhang, X.: Aerosol optical characteristics and their vertical distributions under enhanced haze pollution events: effect of the regional transport of different aerosol types over eastern China, Atmos. Chem. Phys., 18, 2949–2971, doi:10.5194/acp-18-2949-2018, 2018.

Tsamalis, C., Chedin, A., Pelon, J., and Capelle, V.: The seasonal vertical distribution of the Saharan Air Layer and its modulation by the wind, Atmos. Chem. Phys., 13, 11235–11257, doi:10.5194/acp-13-11235-2013, 2013.

Tuna Tuygun, G. and Elbir, T.: Comparative analysis of CAMS aerosol optical depth data and AERONET observations in the Eastern Mediterranean over 19 years, Environ. Sci. Pollut. Res., 31, 27069–27084, doi:10.1007/s11356-024-32950-6, 2024.

Twomey, S. A., Piepgrass, M., and Wolfe, T. L.: An assessment of the impact of pollution on global cloud albedo, Tellus B, 36B, 356–366, doi:10.1111/j.1600-0889.1984.tb00254.x, 1984.

Varga, G., Újvári, G., and Kovács, J.: Spatiotemporal patterns of Saharan dust outbreaks in the Mediterranean Basin, Aeolian Res., 15, 151–160, doi:10.1016/j.aeolia.2014.06.005, 2014.

von Storch, H.: Misuses of statistical analysis in climate research, in: Analysis of Climate Variability: Applications of Statistical Techniques, edited by: von Storch, H. and Navarra, A., Springer-Verlag, New York, 11–26, 1995.

Wei, J., Li, Z., Lyapustin, A., Sun, L., Peng, Y., Xue, W., Su, T., and Cribb, M.: Reconstructing 1-km-resolution high-quality PM2.5 data records from 2000 to 2018 in China: spatio-temporal variations and policy implications, Remote Sens. Environ., 252, 112136, doi:10.1016/j.rse.2020.112136, 2021.

Wei, J., Li, Z., Guo, J., Sun, L., Huang, W., Xue, W., Fan, T., and Cribb, M.: Satellite-derived 1-km-resolution PM1 concentrations from 2014 to 2018 across China, Environ. Sci. Technol., 53, 1–14, doi:10.1021/acs.est.9b03258, 2019.

Willmott, C. J.: On the validation of models, Phys. Geogr., 2, 184–194, doi:10.1080/02723646.1981.10642213, 1981.

World Meteorological Organization (WMO): WMO Airborne Dust Bulletin No. 7 – September 2023, Overview of global airborne dust in 2022, WMO, Geneva, 2023.

Xian, P., Zhang, J., O'Neill, N. T., Toth, T. D., Sorenson, B., Colarco, P. R., Kipling, Z., Hyer, E. J., Campbell, J. R., Reid, J. S., and Ranjbar, K.: Arctic spring and summertime aerosol optical depth baseline from long-term observations and model reanalyses – Part 1: Climatology and trend, *Atmos. Chem. Phys.*, 22, 9915–9947, doi:10.5194/acp-22-9915-2022, 2022.

https://doi.org/10.5194/egusphere-2026-1107
Preprint. Discussion started: 6 March 2026

Xian, P., Reid, J. S., Hyer, E. J., Sampson, C. R., Rubin, J. I., Ades, M., Asencio, N., Basart, S., Benedetti, A., Bhattacharjee, P. S., Brooks, M. E., Colarco, P. R., da Silva, A. M., Eck, T. F., Guth, J., Jorba, O., Kouznetsov, R., Kipling, Z., Sofiev, M., Pérez García-Pando, C., Pradhan, Y., Tanaka, T., Wang, J., Westphal, D. L., Yumimoto, K., and Zhang, J.: Current state of the global operational aerosol multi-model ensemble: An update from the International Cooperative for Aerosol Prediction (ICAP), *Q. J. Roy. Meteor. Soc.*, 145 (Suppl. 1), 176–209, doi:10.1002/qj.3497, 2019.

Xue, T., Liu, J., Zhang, Q., Geng, G., Zheng, Y., Tong, D., Liu, Z., Guan, D., Bo, Y., Zhu, T., He, K., and Hao, J.: Rapid improvement of PM2.5 pollution and associated health benefits in China during 2013–2017, Sci. China Earth Sci., 62, 1847–1856, doi:10.1007/s11430-018-9348-2, 2019.

Yang, Y., Zheng, Z., Yim, S. Y. L., Roth, M., Ren, G., Gao, Z., Wang, T., Li, Q., Shi, C., Ning, G., and Li, Y.: PM2.5 pollution modulates wintertime urban heat island intensity in the Beijing–Tianjin–Hebei Megalopolis, China, Geophys. Res. Lett., 47, e2019GL084288, doi:10.1029/2019GL084288, 2020.

Yue, X., Unger, N., Harper, K., Xia, X., Liao, H., Zhu, T., Xiao, J., Feng, Z., and Li, J.: Ozone and haze pollution weakens net primary productivity in China, Atmos. Chem. Phys., 17, 6073–6089, doi:10.5194/acp-17-6073-2017, 2017.

Yue, S., Pilon, P., Phinney, B., and Cavadias, G.: The influence of autocorrelation on the ability to detect trend in hydrological series, Hydrol. Process., 16, 1807–1829, doi:10.1002/hyp.1095, 2002.

Yue, S. and Wang, C. Y.: Applicability of prewhitening to eliminate the influence of serial correlation on the Mann–Kendall test, Water Resour. Res., 38, 1068, doi:10.1029/2001WR000861, 2002.

Yu, Y., and Ginoux, P.: Enhanced dust emission following large wildfires due to vegetation disturbance, Nat. Geosci., 15, 878–884, doi:10.1038/s41561-022-01046-6, 2022.

Yumimoto, K., Tanaka, T. Y., Oshima, N., and Maki, T.: JRAero: the Japanese Reanalysis for Aerosol v1.0, Geosci. Model Dev., 10, 3225–3253, doi:10.5194/gmd-10-3225-2017, 2017.

Zhang, M., Xie, S., Liu, X., Lin, W., Zheng, X., Golaz, J. C., and Zhang, Y.: Cloud phase simulation at high latitudes in EAMv2: Evaluation using CALIPSO observations and comparison with EAMv1, J. Geophys. Res., 127, e2022JD037100, doi:10.1029/2022JD037100, 2022.

Zhang, Z., Li, J., Che, H., Dong, Y., Dubovik, O., Eck, T., Gupta, P., Holben, B., Kim, J., Lind, E., Saud, T., Tripathi, S. N., and Ying, T.: Long-term trends in aerosol properties derived from AERONET measurements, Atmos. Chem. Phys., 25, 4617–4637, doi:10.5194/acp-25-4617-2025, 2025.

Zhang, J., Reid, J. S., Westphal, D. L., Baker, N. L., and Hyer, E. J.: A system for operational aerosol optical depth data assimilation over global oceans, *J. Geophys. Res.*, 113, D10208, doi:10.1029/2007JD009065, 2008.

Zhao, H., Gui, K., Yao, W., Shang, N., Zhang, X., Liang, Y., Liu, Y., and others: Relative contributions of component-segregated aerosols to trends in aerosol optical depth over land (2007–2019): Insights from CAMS aerosol reanalysis, *Atmos. Environ.*, 333, 120676, doi:10.1016/j.atmosenv.2024.120676, 2024.

https://doi.org/10.5194/egusphere-2026-1107
Preprint. Discussion started: 6 March 2026

Zhao, C., Klein, S. A., Xie, S., Liu, X., Boyle, J. S., and Zhang, Y.: Aerosol first indirect effects on non-precipitating low-level liquid cloud properties as simulated by CAM5 at ARM sites, Geophys. Res. Lett., 39, L09707, doi:10.1029/2012GL051213, 2012.

Zheng, B., Tong, D., Li, M., Liu, F., Hong, C., Geng, G., Li, H., Li, X., Peng, L., Qi, J., Yan, L., Zhang, Y., Zhao, H., Zheng, Y., He, K., and Zhang, Q.: Trends in China's anthropogenic emissions since 2010 as the consequence of clean air actions, Atmos. Chem. Phys., 18, 14095–14111, doi:10.5194/acp-18-14095-2018, 2018.

Zheng, Y., Che, H., Xia, X., Wang, Y., Wang, H., Wu, Y., Tao, J., Zhao, H., An, L., Li, L., Gui, K., Sun, T., Li, X., Sheng, Z., Liu, C., Yang, X., Liang, Y., Zhang, L., Liu, C., Kuang, X., Luo, S., You, Y., and Zhang, X.: Five-year observation of aerosol optical properties and its radiative effects to planetary boundary layer during air pollution episodes in North China: intercomparison of a plain site and a mountainous site in Beijing, Sci. Total Environ., 674, 140–158, doi:10.1016/j.scitotenv.2019.03.418, 2019.

Zuidema, P., Redemann, J., Haywood, J., Wood, R., Piketh, S., Hipondoka, M., and Formenti, P.: Smoke and clouds above the southeast Atlantic: Upcoming field campaigns probe absorbing aerosol's impact on climate, Bull. Am. Meteorol. Soc., 97, 1131–1135, doi:10.1175/BAMS-D-15-00082.1, 2016.